UNIVERSITY OF CAPE TOWN
IYUNIVESITHI YASEKAPA • UNIVERSITEIT VAN KAAPSTAD

A Numerical Assessment of Architectural Parameters for Anisotropic Behaviour in Idealised Trabecular Structures

This work is submitted in partial fulfilment of the requirements of the degree of Master of Science in Engineering specialising in Mechanical Engineering

Author:
Keelan Moore

Supervisor:
Mr Trevor Cloete
Prof. Gerald Nurick

October 22, 2018

Blast Impact and Survivability Research Unit
Department of Mechanical Engineering
Faculty of Engineering and the Built Environment
University of Cape Town

Declaration

1. I know that plagiarism is wrong. Plagiarism is to use another's work and pretend that it is one's own.
2. I have used the IEEE convention for citation and referencing. Each contribution to, and quotation in, this report form the work(s) of other people has been attributed, and has been cited and referenced.
3. This report is my own work
4. I have not allowed, and will not allow, anyone to copy my work with the intention of passing if off as their own work or part thereof

I know the meaning of plagiarism and declare that all the work in the document, save for that which is properly acknowledged, is my own. This thesis/dissertation has been submitted to the Turnitin module (or equivalent similarity and originality checking software) and I confirm that my supervisor has seen my report and any concerns revealed by such have been resolved with my supervisor.

Signature:

Keelan Moore

Date: October 22, 2018

Abstract

Bones macroscopically consist of two major constituents; namely cortical and trabecular (also known as cancellous) bone. Cortical bone is the hard and dense outer layer of bone, which holds the majority of the load bearing capacity. Trabecular bone is the porous internal bone, which distributes loads at joints by allowing for a larger bearing surface and acts as an energy absorber.

Trabecular bone has a complex, heterogeneous, anisotropic open cell lattice structure with a large variation in mechanical properties across anatomic site, species, sex, age, normal loading direction and disease state. A common attempt to account for this variation is to correlate the structure of the trabecular bone sample to the mechanical response, which requires a means of quantifying the structure.

Microstructural indices such as bone volume vs. total volume (BV/TV), trabecular thickness (Tb.Th), trabecular separation (Tb.Sp), structural modal index (SMI) and mean intercept length (MIL) have been widely used to find correlations between structure and properties. Early studies only considered densitometric indices, which accounted for much of the variation however cross study correlations did not agree, leading to an interest in capturing non-scalar valued indices to account for features such as the anisotropy of the bone. The structural anisotropy varies from fully equiaxed to highly directional based on where the trabecular bone is located and what the function would be. The mean intercept length has been proposed as a measure of the structural anisotropy, specifically the interfacial anisotropy of the sample, which is commonly used to account for the mechanical anisotropy.

This research falls within a longer term goal of investigating and understanding the mechanical anisotropy of trabecular bone. To that end, the anisotropy of regular lattice structures was investigated, with the particular goal that the investigated lattices were simple analogues for the more complex structures seen in trabecular bone.

A framework for assessing the structure-property relations of trabecular bone is created, with focus on anisotropy. The mechanical anisotropy of idealised trabecular structures is quantified using well known microstructural indices, which are compared to the numerically determined mechanical response.

The modelling methodology initially investigated 2D lattices that have very well known responses, such that the modelled approach could be verified. Three 2D lattices were used to do this, with the aim that the 3D lattices would be their analogues. Specifically a 2D square, hexagonal and triangular lattice were investigated. The square lattice is highly anisotropic as is the cubic lattice. The hexagonal lattice is isotropic with a large constraint effect as is the Kelvin cell, and the triangular lattice is isotropic with a small constraint effect. The octet-truss was the closest analogue to the triangular lattice, having a small constraint effect and being less anisotropic than the cubic lattice.

The three 3D lattices were chosen to represent highly directional trabecular bone (using a cubic lattice) and more equiaxed trabecular bone, with the fully isotropic Kelvin cell lattice (also known as a tetrakaidecahedron) and the octet-truss lattice which has a lower degree of anisotropy than the cubic. Two confinement arrangements were also investigated as analogues for the trabecular bone at the free surface and at the cortical surface.

To assess the mean intercept length analysis as a measure of mechanical anisotropy, this research performed the analysis on three 3D periodic lattice structures and compared the results to mechanical properties which were numerically determined using finite element analysis.

The mean intercept analysis was performed by generating 3D images for the lattices, similar to the output of μCT images, using a combination of open-source software and custom code, and performing the analysis in BoneJ, an open-source software package. The mechanical response was determined using two methods, namely discrete and continuum modelling approaches.

The discrete approach characterised the lattice with each strut modelled as a Timoshenko beam element solved in LS-DYNA. To capture the anisotropy, the lattice had to be loaded at arbitrary angles, which

was achieved by a rotating the whole lattice and cropping it to a specified test region using custom code. The continuum modelling approach used a homogenisation approach by treating the lattice as a solid material with effective properties. This was solved in a custom implicit solver written in MATLAB using solid elements. The anisotropy was modelled by transforming the elasticity tensor to arbitrary coordinate systems to load the model in arbitrary directions.

The discrete modelling approach suffered from high computational costs and difficulty in removing the boundary effects, all of which would be worsened for models of real trabecular bone. However the discrete approach did accurately captured the mechanical behaviour of the lattices tested. The continuum approach accurately captured some of the responses but failed to capture all behaviour caused by confinement. The continuum model could not capture the switch in predominant deformation mode of the 2D hexagonal lattice caused by lateral confinement, and failed to accurately capture the symmetry of the highly anisotropic 3D cubic lattice.

The mean intercept length analysis failed to capture the anisotropic response of simple periodic lattices, showing no significant difference between the octet-truss and cubic lattices, despite them having a very large difference in mechanical anisotropy. It also showed that the Kelvin cell lattice had the highest degree of geometric anisotropy, which is compared to having the lowest mechanical anisotropy being the only fully isotropic 3D lattice investigated.

The mechanical investigation showed that the lateral confinement has a large effect, significantly scaling the response of isotropic lattices whilst distinctly changing the anisotropic behaviour of the cubic and octet-truss lattice. The mean intercept length analysis can not capture the mechanical confinement effect from geometry alone, and thus fails to capture the mechanical response due to confinement

Overall, the continuum modelling approach showed difficulty in capturing the confinement effect in all lattices and thus a more robust method is required. The mean intercept analysis proved unsuccessful in capturing the mechanical response of three periodic idealised trabecular structures. A new microstructural index that can capture the mechanical anisotropy is required, with the ability to consider the effects of confinement on the structure.

Acknowledgements

I would like to express my gratitude to everyone that offered support and aided in the completion of this work over the last 2 years.

Firstly I would like to thank my family for consistently supporting me in studying further. To my mother and sister for always listening to my complaints when things weren't looking up and to listening to me ramble on about my work when things were going well; your consistent care and support truly made my entire academic career possible. To my father for the financial support when it was needed most.

I would like to specifically thank Claire. I definitely would not be finishing without the work you had done prior to mine, and the help you offered during my project. The time you spent carefully reading my dissertation and finding and correcting my many mistakes was honestly invaluable, I hope I can repay this massive favour. Over and above any technical aspects, you made this environment more interesting and fun since you came, and thank you for all the coffee breaks, no matter how busy you were.

To all BISRU and EPPEI students; you all make this building the weird and fun place it is. To Sherlyn, Dustin and Rendi for the countless hours of fun outside of work, and support during work. I fondly remember all the days that ended at the pub with the three of you, and I hope there are more to come.

Lastly I would like show my gratitude for the supervision of this work. Trevor, your intuition and insight into structural mechanics was invaluable and offered a way forward when things were not working and helped find flaws that I could not see. Your tenacious questioning is something I hope that I carry forward. I would also like to thank you for being one of the few academics that really push for postgraduate study as I would definitely not be here without that. I would also like to thank Professor Nurick for your kindness and the stability that you always offer. The focus that you gave the work is undoubtedly a strong reason for its completion.

List of Figures

List of Tables

Contents

Chapter 1

Introduction

This research involves the creation of a framework for comparing the mechanical behaviour of lattices with reference to their microstructure. A framework was developed to generate lattice structures and determine the mechanical properties using finite element analysis in two approaches, and to determine the microstructural parameters conventionally used to quantify trabecular bone. This chapter outlines background and motivation for the work, as well as a breakdown of objectives followed by an overview of the structure of the report.

1.1 Background and Motivation

Accurate human musculoskeletal modelling can provide insights into how the human body reacts to different environments and how risk of injury can be mitigated without requiring expensive experimental anthropomorphic test devices. Human musculoskeletal modelling can macroscopically be separated into modelling of soft tissues (skin, muscles, tendons, etc) or muscles and hard tissues (bone). The modelling of bone is further separated into modelling the two macroscopic constituents of bone; cortical and trabecular (also known as cancellous) bone (see Figure 1.1).

Trabecular bone has a complex, irregular, anisotropic, open cell lattice structure with a variation in mechanical properties based on anatomic site, species, sex, age, loading direction and disease state [1].

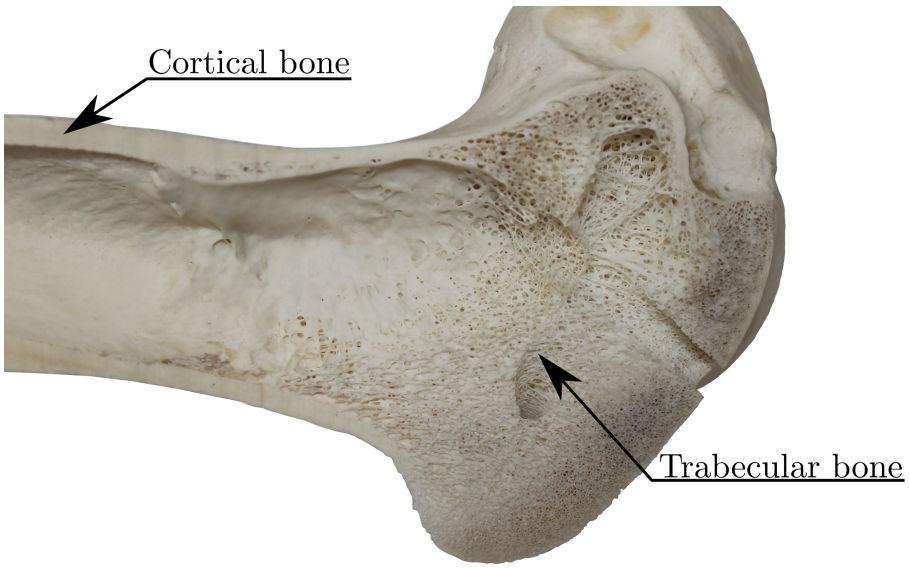

Figure 1.1: Cross section of femur showing cortical and trabecular bone.

Understanding the mechanics of trabecular bone could have substantial effects, for example osteoporosis is a condition characterised by a decrease in bone mineral density and a degradation of bone microarchitecture [2], which particularly affects trabecular bone. There were estimated 9 million osteoporotic

fractures globally in 2000 [3]. Kurtz et al. found an upwards global increase in total hip arthroplasties [4], with a large and unexplained discrepancy in the number per country. Oden et al. predict the number of individuals at risk of osteoporotic fractures to double from 2010 to 2040 [5].

A thorough understanding of mechanical properties of trabecular bone could have applications in fracture risk prediction which could mitigate the increasing number of osteoporotic fractures, aid in the development of internal and external prosthesis and/or development of protective structures to prevent injury from impact loading events. The development of internal prosthesis could be specifically aided by a thorough understanding of the properties of trabecular bone at the implantation site, as the difference in mechanical properties of the implant versus the surrounding bone tissue is thought to be a reason that the implant loosens, causing discomfort and pain in the patient [6].

A common approach to account for the variation in mechanical properties found in trabecular bone samples is to use microstructural indices [7–15]. These indices quantify geometric features or structural properties such as bone volume vs. total volume (BV/TV), trabecular thickness (Tb.th), trabecular separation (Tb.Sp), structural model index (SMI) and mean intercept length (MIL).

Microstructural indices are calculated from images taken of trabecular bone samples; these micro-tomography images (μCT) represent cross sectional slices through the sample which are used in a 3D reconstruction (see Figure 1.2). The indices can be calculated from each image in the stack (for example BV/TV is calculated by the summation of bone pixels vs. non-bone pixels), whilst other indices require the reconstruction of a 3D surface to calculate such as trabecular thickness and separation.

Many of the indices that are used to account for variation in mechanical properties are scalar valued properties, such as BV/TV. Therefore these indices are incapable of accounting for any potential anisotropy present. Mean intercept length is a commonly proposed index to capture the microstructural geometric anisotropy in the specimen [9, 15, 16].

There is no agreement in literature as to which, or which combination of indices produce the best correlation with effective stiffness. This could be in part due to the variance in microstructure seen in trabecular bone. Figure 1.3, adapted from Hildebrand et al [7], shows typical microstructure of trabecular bone at various anatomical sites. If the sample size used in the correlation study is too small, or does not capture a particular microstructural feature in the population, erroneous conclusions may be drawn.

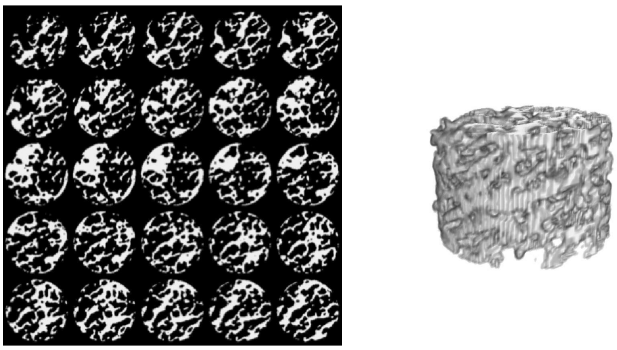

(a) (b)

Figure 1.2: Micro-CT scan of trabecular bone sample: (a) Montage of image slices (b) 3D reconstruction.

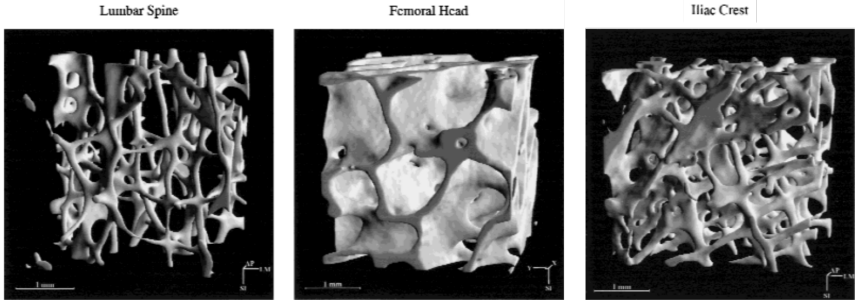

Figure 1.3: Typical trabecular bone structure of lumbar spine, femoral head, iliac crest [7].

This research attempts to mitigate the problems associated with the variation in trabecular bone by investigating correlations between the mean intercept length index and idealised trabecular structures in the form of regular periodic lattices.

The particular lattices where chosen as to capture a wide range of anisotropic behaviours, such that the mean intercept length could be assessed against purely isotropic and highly anisotropic mechanical responses.

The chosen lattices are also required to exhibit a similar range in geometric isotropy as seen in trabecular bone, for example Figure 1.4a shows a highly equiaxed microstructure and Figure 1.4b shows a more aligned microstructure.

The loading of the lattices was also performed with two types of confinement. Figure 1.4 demonstrates the trabecular bone at the free surface (Figure 1.4c) and built into the cortical surface (Figure 1.4d) . The different confinements were important to consider as lateral confinement can have a large effect on both the overall compliance of the structure and the degree of mechanical anisotropy [17].

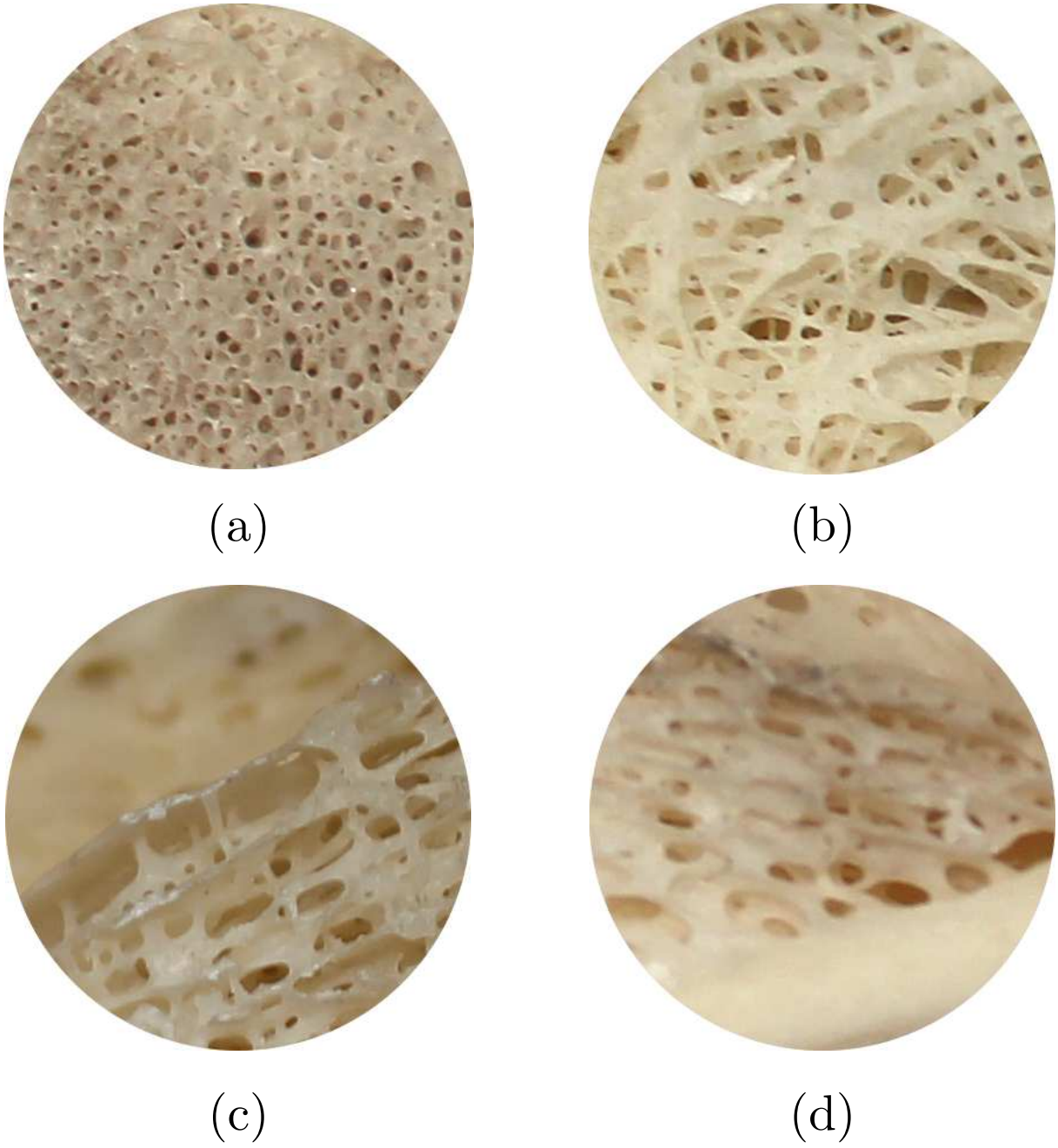

Figure 1.4: Examples of different microstructure taken from the same cross section of femur shown in Figure 1.1: (a) Equiaxed microstructure (b) Highly aligned microstructure (c) Trabecular bone at free edge (b) Trabecular bone built in at cortical surface.

A total of 6 lattices were investigated, with three 2D and three 3D. The three 2D lattices were chosen as they have a range of anisotropic behaviours; with square lattices being highly anisotropic, triangular and hexagonal lattices being isotropic.

The Poisson's ratio of the lattice provides an indication of the effect that the lateral confinement would have, however it is not the only contributing factor. For example, 2D hexagonal lattices shift predominant deformation modes from bending to axial when lateral confinement is added [17]. The 2D hexagonal lattice also has a high Poisson's ratio, and in combination with the shift in predominant deformation mode, has a large confinement effect; whereas the 2D triangular lattice has a relatively low Poisson's ratio and has a smaller confinement effect. The 2D square, and 3D cubic, have a Poisson's effect of 0 in the principal directions, which changes as the loading angle changes and therefore the confinement not only changes the compliance but the degree of anisotropy.

The 3D lattices were investigated as they have a range of behaviours similar to the 2D set, and could act as the 3D analogues to the 2D behaviour. The three 3D lattices are: a cubic lattice, 3D octet-truss lattice which is a lattice based on 8 tetrahedra and 6 octahedra around each vertex and the tetrakaidecahedron (for brevity sake referred to as a Kelvin cell lattice) lattice which is a polyhedron of 6 quadrilateral and 8 hexagonal faces. The original Kelvin cell had slightly curved faces, as it was originally proposed as the optimal shape for packing equal sized objects whilst minimising surface area [18]. The 6 lattices investigated are shown in Figure 1.5.

The 2D square and 3D cubic lattices are analogues for the highly aligned microstructure seen in Figure 1.4b, where longer trabeculae are present and aligned with the common loading direction in the bone. The 2D triangular and hexagonal lattices, and the octet-truss and Kelvin cell lattice are akin to the equiaxed trabecular bone found closer to the femoral head as shown in Figure 1.4a.

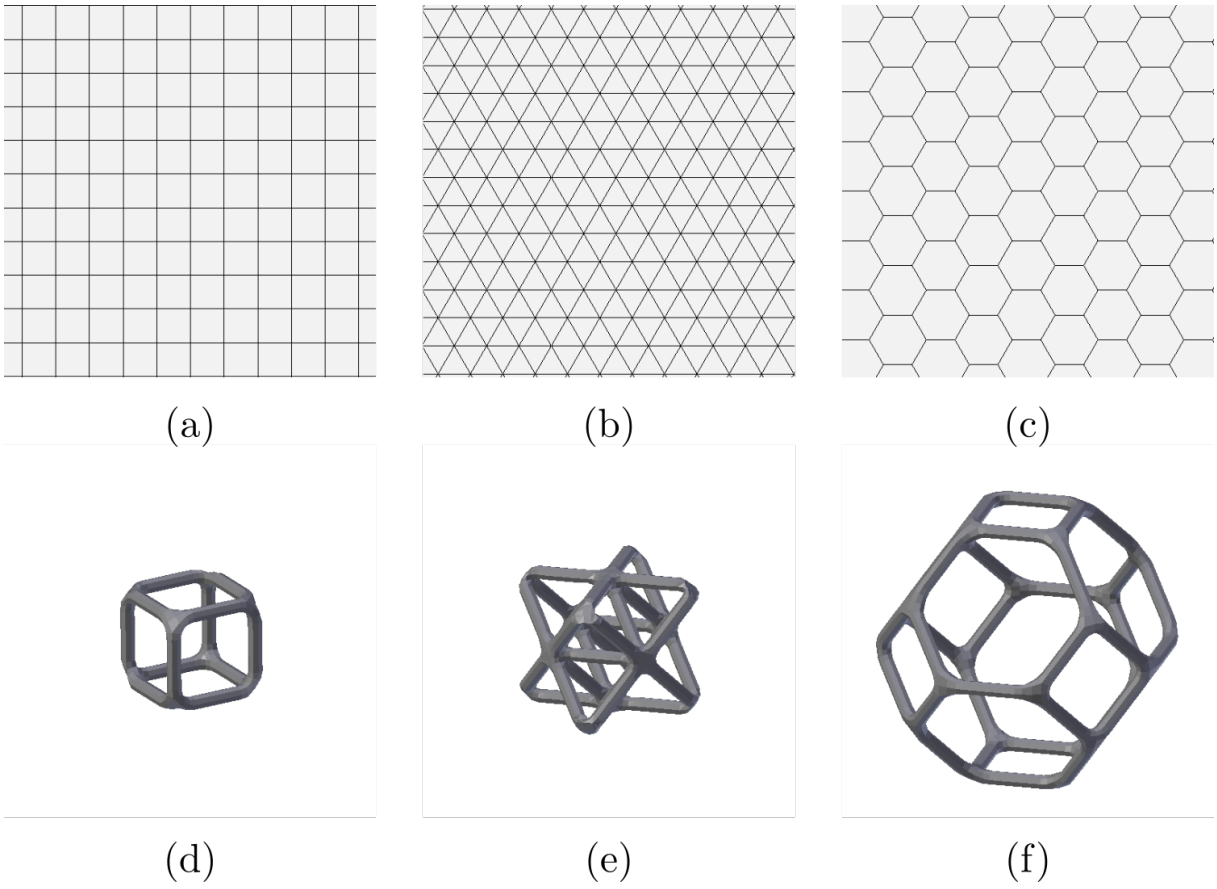

Figure 1.5: Lattices investigated: (a) 2D Square (b) 2D Triangular (c) 2D Hexagonal (d) Cubic unit cell (e) Octet truss unit cell (f) Kelvin cell unit cell.

1.2 Research Objectives

The aim of the research is the assessment of microstructural indices for anisotropic behaviour using idealised trabecular structures. To achieve this, a framework for calculating mechanical properties of periodic lattices at arbitrary angles and determining the corresponding microstructural indices was developed. The objectives of the research are listed:

1. To develop a robust method for generating periodic lattice structures for use in finite element models.
2. To develop a method for simulating the response of lattice structures under arbitrary loading directions.
3. Investigate the anisotropic mechanical behaviour of three 2D periodic lattices and three 3D periodic lattices.
4. To develop a method for determining microstructural indices associated with investigated periodic lattices.
5. Assess the correlation between the anisotropic behaviour of lattice structures and mean intercept length (MIL).

1.3 Report Outline

Following this introduction, a review of relevant literature is presented in Chapter 2. A brief overview of the bone anatomy and structure is presented, which is followed by common approaches used in the numerical modelling of trabecular bone. Microstructural indices are explained, including their methods of calculation; this is followed by an overview of correlation studies present in literature. Finally, the previous work performed analysing the mechanical properties of the particular lattices investigated in this research is presented, including numerical and analytical modelling techniques.

Chapter 3 details the methodology used in modelling the lattice structure directly. The method for generating lattices is described, followed by the approach used to load the lattice at arbitrary angles. A description of the finite element model used is presented, along with the applied boundary conditions. The method of calculating the effective mechanical properties from the output of the finite element modelling is described.

Chapter 4 details the modelling of the lattices as a continuum. This is to increase the number of loading directions used in assessing the anisotropy, as continuum models require fewer elements than the discrete modelling approach to achieve the same accuracy. A description of the method for transforming the elasticity matrix to assess anisotropy is presented along with details of the finite element model employed. The method used to compare the continuum modelling results to the discrete modelling results is presented.

Chapter 5 details the methodology used in determining the microstructural indices from the lattice geometry. The method for preparing models of the lattice geometry for software used to calculate microstructural indices is presented; this includes creating a solid model of the lattice geometry and slicing said model to create the image stacks to mimic output of micro-tomography scans.

Chapter 6 provides discrete modelling results and verifies the numerically determined results against analytical values where possible. Chapter 7 shows a mesh convergence study and investigation into the performance of the continuum model's ability to capture the anisotropic behaviour; followed by the results of the continuum modelling. Chapter 8 shows the results of the microstructural index analysis of the three 3D lattices.

Chapter 9 includes a discussion of the three previous chapters, collating the mechanical behaviour with the microstructural indices results. The main conclusions are presented in Chapter 10 and recommendations for future work are presented in Chapter 11.

Chapter 2

Literature Review

This chapter outlines the relevant literature, starting with a brief overview of the anatomy of structure of bone, with attention paid to the microstructure of trabecular bone. A review of the microstructural indices used to quantify trabecular bone microstructure, along with the methods of calculation and mechanical property correlation studies performed is presented, followed by an overview of the numerical modelling techniques used for trabecular bone. Analytical solutions for the lattices investigated are presented and finally, the method of cellular solid homogenisation.

2.1 Bone Anatomy and Structure

Bone is a complex hierarchical material with varied structure and material viewed at different scales. This hierarchical structure is used to achieve a wide range of mechanical, chemical and biological properties.

Bone is, macroscopically, comprised of two major constituents, hard outer cortical bone and the spongy internal trabecular bone. The majority of the load bearing capacity is ascribed to the cortical bone, whereas trabecular bone distributes the load to the cortical bone at the joints and acts as an energy absorber [19].

Trabecular bone is found at the heads of long bones such as the femur where the trabecular bone hosts the bone marrow whilst minimising weight for an increased surface area, providing a large bearing surface which decreases stresses at the joints (see Figure 2.1a). It is also present in flat bones such as the iliac crest (pelvis) and calvaria (skull) which have thin layers of cortical bone supported by a trabecular bone structure (see Figure 2.1b), similar to composite sandwich panels [6, 19, 20].

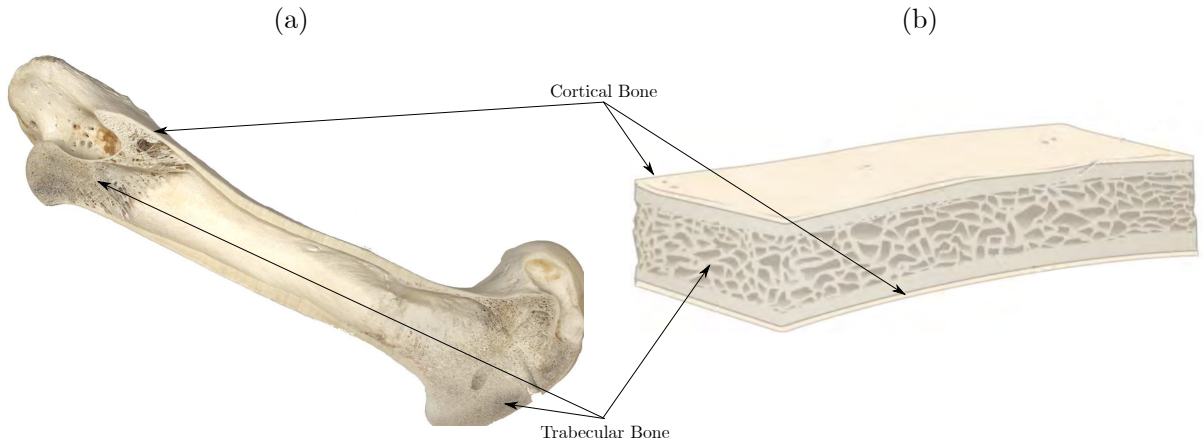

Figure 2.1: Examples of macroscopic difference between cortical and trabecular bone: (a) Cross section of bovine femur (b) Diagram of calvaria adapted from Anatomy & Physiology [21].

The differentiation between the two major bone types is most readily performed by comparing density or porosity of different specimens as trabecular bone is less dense than cortical, however the microstructure of bone makes for a clearer distinction.

At the microstructural level, bone is comprised of arrangements of mineralised collagen fibres called lamellae [19–21]. Cortical bone is composed of multiple concentrically wrapped cylinders of lamellae called osteons. The lamellae can also be unordered which is called woven bone or are tangential to the bone around the circumference which is called lamellar bone. Trabecular bone, consists of a network of trabeculae which are individual beams or plates. Trabecular bone can be categorised in terms of basic structures; rod-rod, rod-plate and plate-plate [19,20]. Figure 2.2 shows examples of these three trabecular structures.

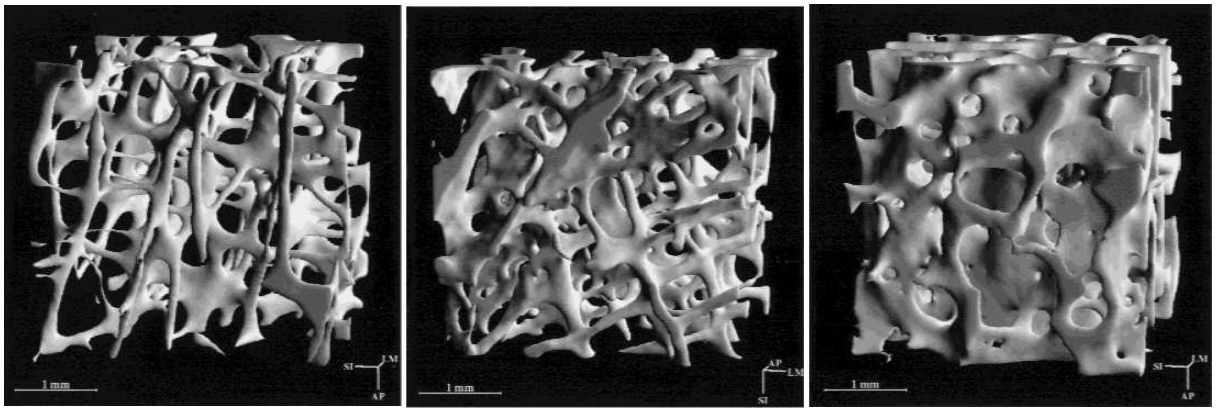

Rod-rod Rod-plate Plate-plate

Figure 2.2: Examples of different trabecular bone structures [7].

The structure of trabecular bone can vary dramatically inter-subject and even inter-bone. The structure and mechanical properties also vary with anatomic site, species, sex, age, loading direction and disease state [1].

Due to the nature of trabecular bone a distinction must be made between the structural properties of the entire bone and the material properties of the individual trabeculae which make up the structure.

The large and unpredictable variation in structure, in concert with the fact that there is little agreement in the material properties of the individual trabeculae (values for the elastic modulus ranging from 1 to 20 GPa in literature [20]), makes the accurate modelling of bone an incredibly complex task.

2.2 Microstructural Indices

The microstructure of trabecular bone is a highly heterogeneous, anisotropic open cell lattice structure which makes categorising features of the microstructure difficult. Microstructural indices attempt to quantify different structural properties such that microstructural features can be categorised which leads to the ability to do correlation studies between structural features and behaviours. A number of microstructural indices have been proposed in literature; this section gives an overview of the indices proposed, method of calculation and correlation studies performed.

2.2.1 Overview

Microstructural indices are calculated for bone specimens that have been imaged with a micro-computed tomographic or X-ray microtomographic systems. These 3D images are in the form of a stack of 2D images, each representing slices through the specimen; the calculation of the microstructural indices are either based directly on the image stack or are calculated once the image stack has been reconstructed as a 3D model.

The microstructural indices are calculated using a free and open source plugin for ImageJ called BoneJ [16]. Table 2.1 shows the list of indices calculable using BoneJ, along with the name of the option in the software used.

Table 2.1: Microstructural indices, showing common abbreviations when applicable and the option in BoneJ used.

Microstructural Index	Abbreviation	BoneJ Option
Branch Length		Analyse Skeleton
Number of Branches	Tb.N	
Number of Junctions		
Mean intercept length ellipsiod	MIL	Anisotropy
Degree of anisotropy	DA	
Connectivity Density	Conn.D	Connectivity
Bone Surface	BS	Isosurface
Plateness		Ellipsoid Factor
Structural Model Index	SMI	Structural Model Index
Trabecular Thickness	Tb.T	Thickness
Trabecular Separation	Tb.S	
Bone Volume	BV	Volume Fraction
Total Volume	TV	

The following subsections go into detail on the method of calculation for the microstructural indices shown in Table 2.1.

2.2.1.1 Analyse skeleton

The analyse skeleton tool calculates information regarding branches and junctions by taking in a skeletonised representation of the bone image and classifying each voxel as an end-point, junction or slab based on whether the neighbouring 26 voxels are part of the skeleton.

The skeletonised representation of the bone image is created using a 3D thinning algorithm implemented in ImageJ [22]. The 3D thinning algorithm finds the centerlines of the object by iteratively eroding the surface of the object until only the skeletal information remains [22].

Further, the analysis uses the classified voxels to count the length of each branch (a number of connected slab voxels) and gives the average branch length with the number of branches. The number of junctions is similarly calculated by counting the number of separate clusters of junction voxels [16].

2.2.1.2 Anisotropy

The anisotropy analysis calculates the mean intercept length ellipsoid, which is proposed as a fabric tensor representing the anisotropy of trabecular bone, and a scalar measure of anisotropy called the degree of anisotropy (DA), which is calculated from the mean intercept length ellipsoid [16].

The mean intercept length method is implemented in BoneJ as follows. A random point within the sample is chosen and a large number of vectors with the same length are drawn from that point, through the sample. An intercept is defined as when a vector crosses between the bone and marrow (foreground and background). The number of intercepts are counted for each vector, and the mean intercept length is defined as the length divided by the number of intercepts counted. This process is repeated for different random points until a tolerance of the coefficient of variation or a maximum number of points is met [16].

This is a variant on the method described by Hildebrand et al. [7] where parallel vectors are superimposed on the sample and the intercepts are counted. The mean intercept length in that direction is defined as the total length of the test vectors divided by the total number of intercepts.

The mean intercept length for all directions is fitted with an ellipsoid using a least squares fit. This is defined as the mean intercept length ellipsoid, which is also the basis for the material anisotropy, or fabric, tensor. Eigendecomposition is used to find the lengths of the ellipsoids axis, which is used to define the degree of anisotropy as a scalar from 0 to 1; where 0 represents fully isotropic structure and 1 represents fully anisotropic structure. The degree of anisotropy is calculated as:

$$DA = 1 - \frac{\lambda_{long}}{\lambda_{short}}, \tag{2.1}$$

where λ_{long} is the eigenvalue of the long axis and λ_{short} is the eigenvalue of the short axis.

2.2.1.3 Connectivity

The connectivity analysis estimates the number of connections in the trabecular bone sample by calculating the Euler characteristic. The Euler characteristic or number is a topological invariant that describes an object's structure [6, 23]. The method of calculating the Euler characteristic uses volume neighbourhoods and connectivity between voxels, which makes no assumptions about the structure of the trabecular bone [23].

The method calculates the Euler characteristic for each voxel, which is summed for all voxels to find the Euler characteristic of the whole sample. The contribution of the structure that the sample was removed from is calculated and corrected for, by considering the voxels at the edges of the 3D image. The connectivity estimate is calculated from the corrected Euler characteristic. The connectivity density is calculated as:

$$Conn.D = \frac{C_{est}}{V_t}, \tag{2.2}$$

where C_{est} is the estimated connectivity and V_t is the volume of the whole 3D image.

2.2.1.4 Isosurface

The surface area of the sample is calculated by creating a 3D reconstruction of the sample as a triangulated surface mesh, using the marching cubes algorithm. The total surface area is calculated by the summation of the area of all surface triangles [16].

The marching cubes algorithm creates a surface triangle representation of a binarised 3D image by placing triangles based on the surrounding voxels. The algorithm places a cubic with 8 voxels at each of the corners and determines how the surface intercepts the cube by a lookup table. This is repeated for every voxel in the image. Without utilising symmetries, the lookup table would contain 2^8 entries, however this is reduced to only 14 possible intersections by using the rotational and reflective symmetry of the problem [24]. Figure 2.3 shows these fourteen possible intersections.

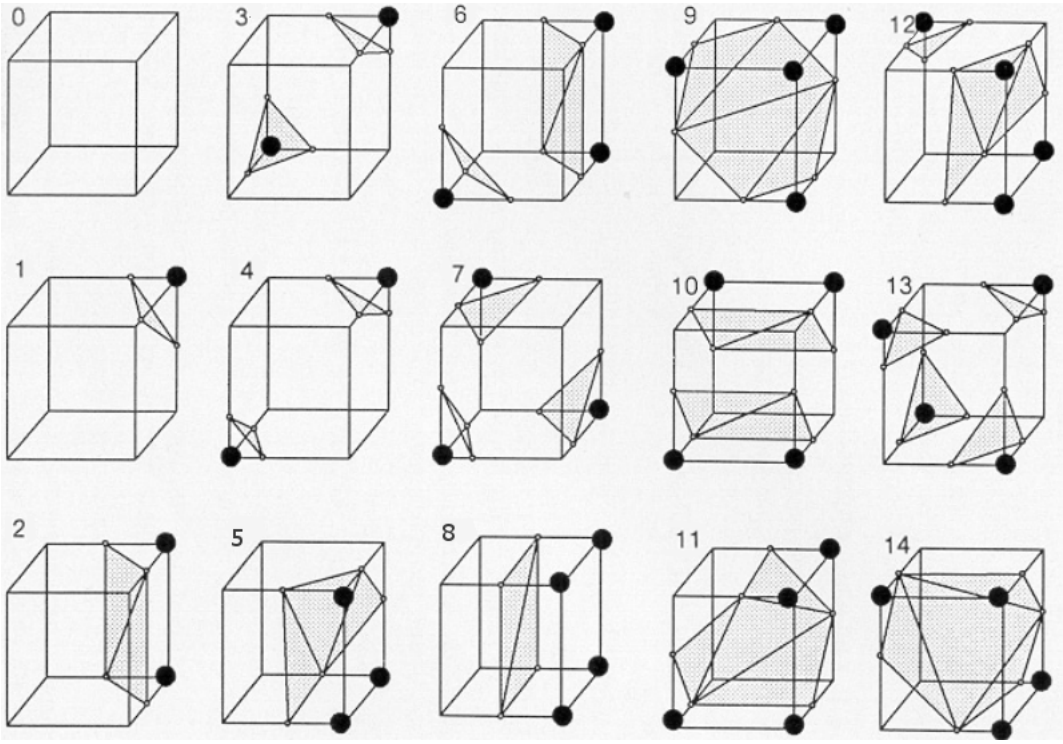

Figure 2.3: Fourteen possible intersections used in the 3D marching cubes algorithm [24].

2.2.1.5 Ellipsoid factor

The ellipsoid factor is a method for determining how plate-like or rod-like the trabecular bone sample is locally. The method works by first skeletonising the 3D image to find the medial axes for the object (see Section 2.2.1.1). Ellipsoids are seeded along the medial axes of the object and iteratively dilates, rotates and translates the ellipsoids to find the maximum volume whilst being fully encapsulated by the bone. The ratio of the axes lengths is calculated to determine if the ellipsoid is more oblate (disc-like) or prolate (spear-like) [25].

The ellipsoid factor is calculated from the three semi-axis lengths (a, b, c) of the maximal ellipsiod as follows:

$$a \leq b \leq c \quad , \quad EF = \frac{a}{b} - \frac{b}{c}, \tag{2.3}$$

where a, b, c are the lengths of the semi-axis of the ellipsoids in order of size and EF is the ellipsoid factor.

2.2.1.6 Structural model index

The structural model index (SMI) is a commonly used quantification to determine whether the trabecular bone sample resembles a more rod- or plate-like structure [26]. Despite the wide usage, there is reasonable doubt as to whether the index does indeed capture the structure of the bone, see Section 2.2.2 for more detail.

The methodology is based on a differential analysis of the bone surface, which requires a triangulated surface mesh (see Section 2.2.1.4). The SMI is calculated as:

$$SMI = 12\frac{\epsilon + \epsilon^2}{1 + 4(\epsilon + \epsilon^2)}, \tag{2.4}$$

where ϵ is defined as the rod-plate volume ratio. This ratio is calculated as:

$$\epsilon = \frac{V - rS}{rS + 2V}, \tag{2.5}$$

where V is the structure volume, S is the derivative of the volume with respect to the surface normal and r is half the thickness of the structural element. r is assumed constant over the whole structure [27].

The volume derivative with respect to the surface normal is calculated numerically by calculating the volume of the structure $V(r)$, displacing all the vertices along the surface normal by a small amount δr and recalculating the volume $V(r + \delta r)$; the approximate derivative is defined as $S = \frac{V(r+\delta r)-V(r)}{\delta r}$. The value of δr can be chosen between 1/10 and 1/1000 [27].

For an ideal plate structure the SMI is 0, and an ideal rod structure the SMI is 3; for bone samples with varied volume fraction of plates and rods the SMI will range between the two ideal limits [27].

2.2.1.7 Thickness

The thickness calculation is based on a local thickness algorithm developed by Dougherty and Kunzelmann [28]. The local thickness at a point is defined as the diameter of the largest sphere that is fully encapsulated by the structure and that contains the point. The point does not need to be at the centre of the sphere. The local spacing information is calculated using an inverted image.

The trabecular thickness (Tb.Th) and spacing (Tb.Sp) are calculated as the mean of all the local thickness and spacing information. This is presented with the standard deviation [16].

2.2.1.8 Volume fraction

The volume fraction is calculated using two methods in BoneJ [16]. The simplest method is the number of foreground pixels divided by the number of background pixels. The more complex method calculates the volume enclosed by a closed triangulated surface mesh, created using the marching cubes algorithm (see Section 2.2.1.4), and dividing by the total volume.

2.2.2 Correlation studies

The variation in properties of trabecular bone, along with the variation in microstructure has lead to multiple attempts to correlate various microstructural indices to physical properties. There is no widely agreed upon index or set of indices that provide the strongest correlations with mechanical properties.

Early attempts to account for the variation in mechancial properties considered purely densitometric measures. Galante et al. [14] considered two measures of density, the apparent density as the weight divided by the sample volume and the actual or real density as the weight divided by the volume of the bone (determined by displacement of water). A strong linear relationship was found between the apparent density and elastic modulus of the samples tested.

Lotz et al. [29] considered the apparent density and the mineral density measured using CT imaging. They found a strong power correlation between the elastic modulus and densitometric measures. The apparent density, raised to the power 1.4 showed a correlation of 91% and the mineral density, raised to the power 1.2 showed a correlation of 90%. Keller [13] considered the apparent ash density, or dry density, and found that both linear and power models produced high correlations. However the highest correlations where found with power models. Correlation of 96.5% with $E = 10.5\rho_{\alpha}^{2.57\pm0.04}$ was found. Hodgkinson and Currey [30] found a correlation of 91% using a close to quadratic power relation between Young's modulus and the apparent density. Despite high correlations being found using densitometric measures in individual studies, there is a large variation in the nature of the correlations [12]. Helgason et al. [12] performed a literature review of correlations using only densitometric measures and found little agreement between studies, demonstrating that densitometric measures are insufficient. Figure /reffig:densitometricCorrelationStudies visually demonstrates the lack of agreement.

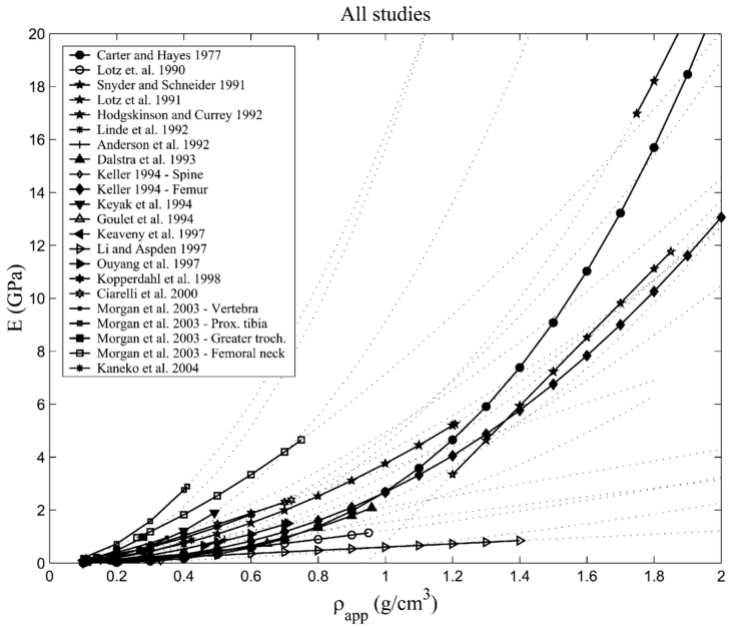

Figure 2.4: Young's modulus vs. apparent density from multiple sources [12].

Goldstein et al. [9] suggested that scalar densitometric measures were not sufficient due to the heterogeneity of the structure leading to anisotropic behaviour. A wide range of microstructural indices were considered, including measures of anisotropy using the mean intercept length method. They performed multiple regression analysis and found the correlation could be improved by combining the bone volume fraction with anisotropy, quoting 90% of variance accounted for; however the manner in which they used the mean intercept length ellipsoid was not specified. Strong correlations between independent indices were also found, with a highly significant relationship between the trabecular plate number and connectivity with bone volume fraction quoted [9].

Ulrich et al. [11] similarly suggested that more than merely densitometric measures must be used to account for the still unexplained variance. It was found that the correlation improved from 53% to 82% when relative density (BV/TV) and mean intercept length ratio were used as opposed to only using relative density. A further increase to 92% correlation was quoted when relative density, mean intercept length ratio and trabecular spacing was considered. The set of indices that lead to the best correlations

varied based on anatomical site. Moesen et al. [15] quotes between 75-90% correlation with Young's modulus using a fabric tensor based on mean intercept length method.

Ding et al. [8] correlated how plate-like or rod-like the structure is using structural model index (SMI) with the mechanical properties, finding a correlation of 42% using a linear regression analysis. They found an increase in correlation by separating the data into three age groups, using a different index or set of indices for each. It was demonstrated that a correlation of 57% was present using connectivity density alone for the young cohort, 52% was present using trabecular thickness for the middle-aged cohort and 58% was present using apparent density and degree of anisotropy for the old-aged cohort. This suggests that different mechanisms are present in the structure-property relation during ageing. The correlations found in the study by Ding et al. [8] were substantially lower than found by other studies.

Cui et al. [10] similarly found the structural model index to be important, showing the second highest correlation with Young's modulus (51%) with the highest being relative density (76%). The degree of anisotropy and trabecular thickness alone showed no significant correlation with mechanical properties, in contrast to previous investigations [9, 11, 15]. It was shown that a combination of indices produced higher correlations, similar to Ulrich et al [11]. Combining structural model index, trabecular number and trabecular thickness resulted in a correlation of 80%. The mechanical properties were not experimentally determined, but determined using finite element analysis assuming a constant material property throughout which could have lead to erroneous results.

2.2.3 Critique of Microstructural Indices

There have been, in recent years, an analysis of certain microstructural indices that have noted theoretical flaws in the definition of the index. This section outlines flaws in the structural model index (noted by Salmon et al. [26]) and the mean intercept length (Kalttx et al. [31]).

Salmon et al. [26] bring to light a problem with the definition of the structural model index and assert that it does not measure the plate- or rod-likeness of the structure. The methodology makes assumptions regarding the convexity of the structure, assuming constant positive curvature of the surface. This is in contrast to actual trabecular structures which are highly concave. The structural model index is negative when evaluated on concave surfaces, which imparts error into the presumed positive SMI. Salmon et al. [26] demonstrated that the SMI failed to capture the plate to rod transition when simulating the erosion of trabecular bone, noting that SMI is strongly correlated to relative density. They propose the ellipsoid factor as a more accurate measure of structure and demonstrate that the ellipsoid factor accurately detects the rod-like trabecular bone in avian samples and is not confounded by the relationship with relative density and percentage convexity like the structural model index.

The strong relationship between the structural model index and relative density is likely the reason it provides false positive correlations with elastic modulus, as the relative or apparent density has well known correlations with the elastic modulus.

Klattx et al. [31] investigated the assumption that the polar plot of the directional mean intercept length is, in general, an ellipse. To do this, they developed an analytical solution for the mean intercept length for overlapping grain models of porous media, supplemented by numerical simulations. The findings demonstrate that the polar plot of the mean intercept length is not an ellipse in general for simple boolean models of porous media. This has implications in how the mean intercept length is used to create a fabric tensor to define the structure-property relation, as the fabric tensor is created by a least squares fitted ellipsoid and can not in general be represented by a second rank tensor.

2.2.4 Summary of Correlation Studies and Discussion of General Trends

Table 2.2 shows a summary of the correlation studies reviewed. The summary of indices used demonstrates that no conclusions has been met regarding which combination of indices produce the highest correlations. However, it does show that the BV/TV, which is a measure of apparent density, is common throughout. In more recent studies the SMI seems to overtake BV/TV. This is due to the strong correlation between the SMI and BV/TV. The apparent density alone does not account for all of the variation, noted in the literature review by Helgason et al. [12], and other indices that capture the determining features of the structure that define the structure-property relation are required. The mean intercept length is an attempt to capture the inherent anisotropy present in trabecular bone, as pure scalar values are not sufficient.

Table 2.2: Overview of the results from a series of correlation studies.

Authors	**Microstructural Index**	**Correlation**	**Year**
Galante el al. [14]	Apparent Density	High Correlation	1970
Lotz et al. [29]	Apprent Density	91%	1990
Keller et al. [13]	Ash density	96.5%	1991
Hodgkinson & Currey [30]	Apprent Density	91%	1992
Goldstein et al. [9]	BV/TV and MIL	90%	1993
Ulrich et al. [11]	BV/TV, MIL, Tb.Sp	92%	1999
Ding et al. [32]	SMI	42%	2002
Cui et al. [10]	SMI, Tb.N, Tb.Th	80%	2006
Moesen et al. [15]	MIL	75-90%	2012

2.3 Numerical Modelling of Trabecular Bone

This section gives an overview of the common methods for finite element modelling of trabecular bone. Finite element analysis of trabecular bone has been used widely in research, for example the approach has been used to determine material properties by correlation with experimental results [33], determine structural response [10,34–36], predict and understand fracture mechanics [37] and attempt to accurately predict behaviour from in-situ trabecular bone scans [38].

Finite element analysis is well posed to model trabecular bone due to the complex structure of the bone; and with the very high resolution μCT available, the finite element meshes can accurately model the geometry. There are two conventionally used methods using continuum elements to build FE meshes from μCT scans; one using axis aligned hexahedral elements and other using tetrahedral elements [35].

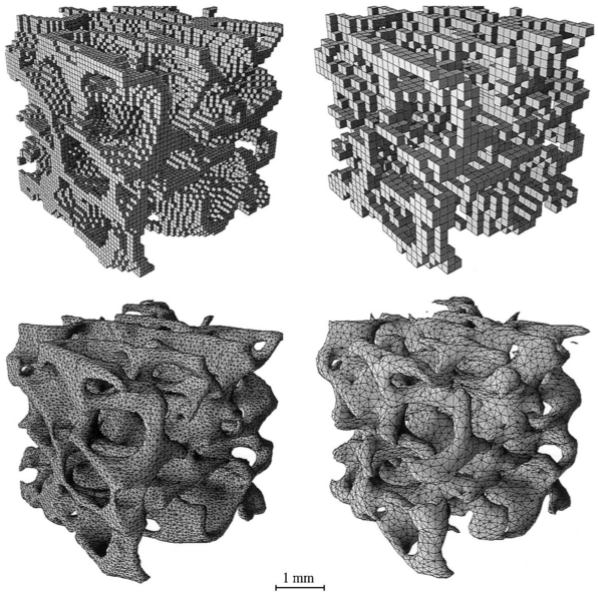

Figure 2.5: Finite element meshes of trabecular bone using two different resolutions (84 μm and 168 μm) with two element types: axis aligned hexahedral elements (top) and tetrahedral elements (bottom) [35].

Both methods require a thresholded μCT image, where each voxel is classified as either bone or background. The output from a μCT scan is a greyscale image, where the grey value of each voxel represents the density.

The hexahedral meshing method loops over each voxel of the thresholded μCT image and places an axis aligned hexahedral element when a bone voxel is found. The tetrahedral meshing method relies on the marching cubes algorithm outlined in Section 2.2.1.4, which creates a triangulated surface mesh. Each surface triangle is used as a face of a tetrahedral element, and the internal volume is filled with uniformly sized tetrahedral elements. This results in a much smoother representation of the surface than when hexahedral elements are used, which is demonstrated in Figure 2.5.

Recently another method for meshing the μCT images have been used, where shell and beam elements are used instead of continuum elements based on volumetric decomposition of the μCT images into the plates and rods that make up the trabecular bone structure [39–42]. The individual trabecular rods are modelled using 2 node-beam elements and the trabecular plates are modelled using multiple shell elements. The thickness of the elements are determined using a local thickness approximation as described in Section 2.2.1.7. Figure 2.6 shows an example of the plate and rod decomposition as performed by Van Lenthe et al. [39].

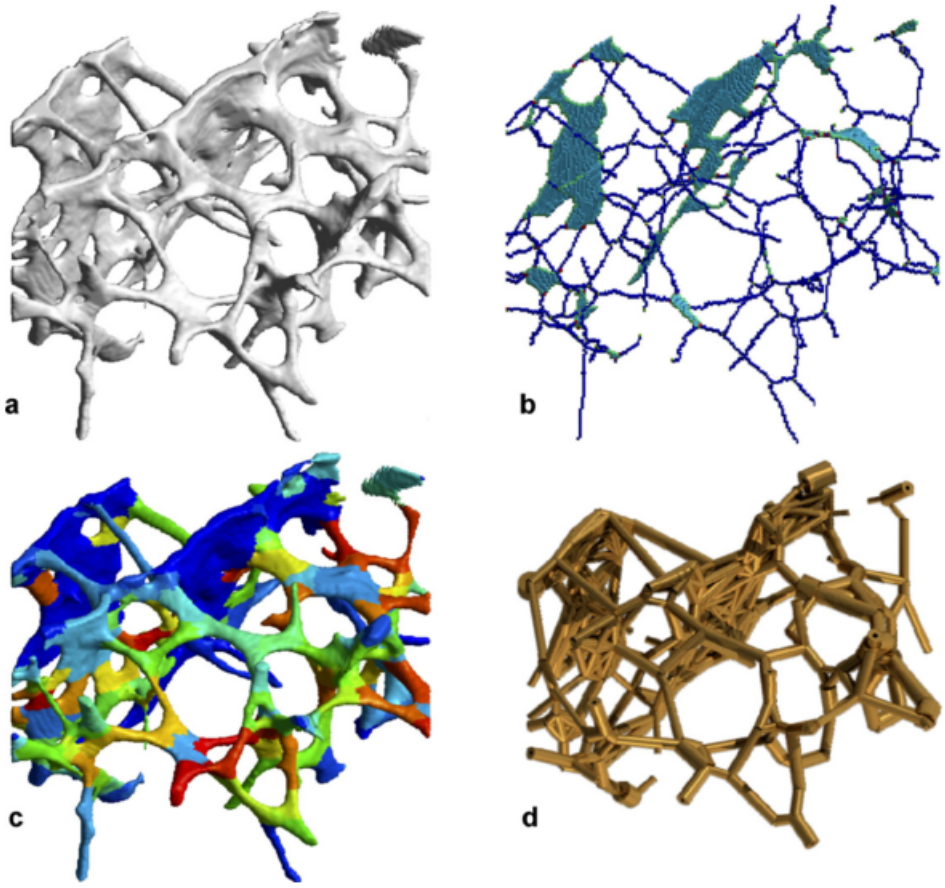

Figure 2.6: Example showing decomposition of μCT image into plate and rod model. (a) μCT image topological reconstruction, (b) skeletonisation and point-classification, (c) multi-colour dilation (d) plate and rod model of μCT with correctly specified element thicknesses [39].

The method has the clear advantage of lower computational costs as fewer elements are required, however there are more important clinical advantages. The lowered computational cost means the method is more applicable to clinical environments that may not have large computational resources. The other clinical advantage has to do with analysis of the micromechanics, as the stress and strain states of individual trabeculae are trivially accessible whereas in approaches using continuum elements the response of individual trabeculae could only be assessed by navigating through several (up to millions) of elements [42].

Importantly the structural response and overall behaviour plate and rod method shows high correlation with continuum element modelling methods. Wang et al. [42] investigated the accuracy of the plate and rod method by comparing the response of idealised microstructural models (see Figure 2.7) with a wide range of trabecular thicknesses. They quote a 762 times reduction in computational time for the largest model and high correlation ($R^2 \geq 0.99$) between conventional continuum element models and the plate and rod model.

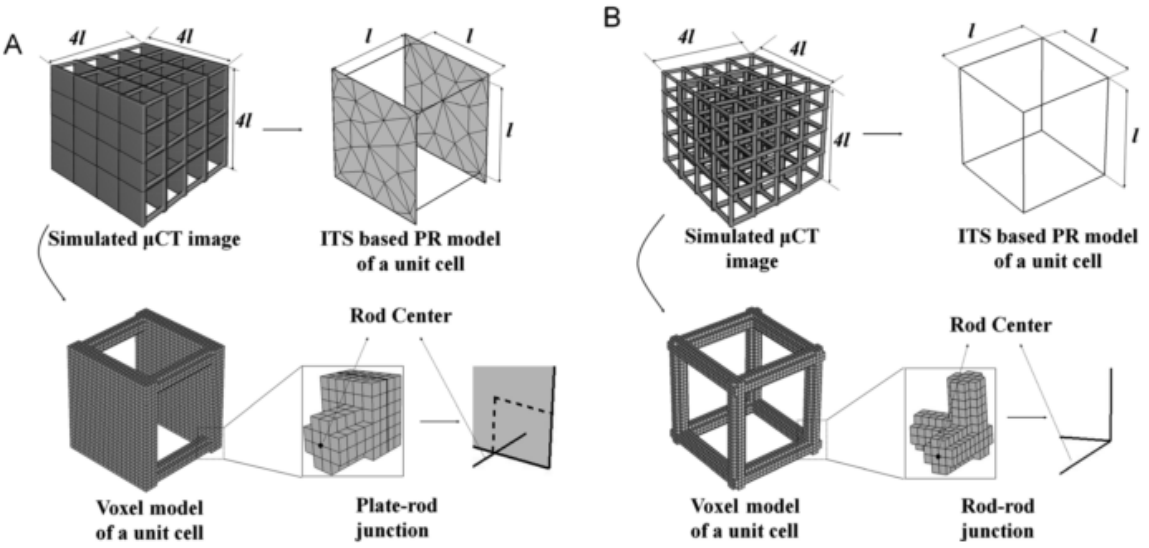

Figure 2.7: Idealised trabecular structures showing both voxel based mesh and plate and rod mesh [42].

It was demonstrated that the plate and rod model of the idealised plate-plate and plate-rod structures showed high correlation with structural response (effective Young' modulus) and yield strength; $R^2 \geq 0.99$ for any voxel size investigated [42]. However, the plate and rod model did under-predict the effective Young's modulus for the idealised rod-rod structure for trabecular thicknesses of 240 μm and 320 μm; this deviation is ascribed to a limitation of beam theory with shear deflection of thick beams [42] and thus the deviation could be overcome by using a different beam formulation. However, the deviation is acceptable as the average trabecular thickness is 100 μm in rod-predominant structures [42]. This demonstrates that beam and shell modelling is a sound research avenue for trabecular bone and trabecular-like structures.

Regardless of meshing methodology, without an accurate measure of the mechanical properties of the trabecular material the model will not accurately capture the structural response. It is important to clearly distinguish between the properties of the structure and the properties of the material (individual trabeculae). It was assumed that the elastic modulus of individual trabeculae would be the same as for thin cortical bone samples, however several investigations show considerably lower elastic moduli than whole bone [20].

There is a very large discrepancy in literature for the material properties of trabecular bone; ranging from 1 to 20 GPa [20]. Rho et al. [43] performed nano-indentation experiments to determine properties of trabecular bone; and quoted a statistically significant variance in elastic modulus for the tested samples. The possible causes for the variance that were considered were the influences of microstructural defects such as cement lines and voids, uncertainty in the geometry of the specimens due to their small size and the difficulty in correctly aligning small specimens in fixtures for testing [43]. Choi et al. [44] states that, even though individual trabeculae are at the microstructural scale, the response of trabecular bone specimens should potentially still be considered a structural response rather than a material property [44].

Table 2.3 shows experimentally determined elastic moduli for trabecular bone, using a wide range of testing procedures. This demonstrates the lack of agreement on the exact material properties of trabecular bone.

Table 2.3: Overview of values of elastic modulus for trabecular bone and how there were determined. Adapted form [20].

Author	Year	Method	Estimate of elastic modulus (GPa)
Runkle and Pugh [45]	1975	Buckling	8.96 ± 3.17
Townsend et al. [46]	1975	Inelastic buckling	11.38
Williams and Lewis [33]	1982	Back-calculating from FEM	1.3
Ashman and Rho [33]	1988	Ultrasound test method	12.7 ± 2.0
Ryan and Williams [47]	1989	Tensile testing	0.76 ± 0.39
Hodgskinson et al. [48]	1989	Microhardness	15
Kugn et al. [49]	1989	Three-point bending	3.81
Mente and Lewis [50]	1989	Cantilever bending with FE analysis	7.8 ± 5.4
Choi et al. [44]	1990	Four-point bending	5.35 ± 1.36
Rho et al. [51]	1993	Tensile testing	10.4 ± 3.5
		Ultrasound test method	14.8 ± 1.4
Rho et al. [43]	1997	Nanoindentation (longitudinal)	19.6 ± 3.5
		Nanoindentation (transverse)	15.0 ± 3

Table 2.4 shows an overview of the elastic moduli used in various finite element analyses of trabecular bone [10, 34–36, 39, 40, 52–56]. There is a clear discrepancy noted when comparing the elastic moduli used as material properties commonly in finite element analysis of trabecular bone to the attempts to experimentally determine the mechanical properties. Commonly a value of 10 GPa is used as the element properties, and very commonly simple isotropic material models are used for the trabecular bone. Further investigation into the material properties of trabecular bone is required as incorrect values used in modelling could lead to erroneous descriptions of the mechanical behaviour and misunderstanding of the functions that different microstructures offer.

Table 2.4: Summary of elastic moduli used for the trabecular material properties in various finite element analyses of trabecular bone.

Author	Year	Element Type	Tissue Elastic modulus (GPa)
Muller [52]	1995	Hexahedral	12.72 (average)
Lengsfeld et al. [34]	1998	Hexahedral and Tetrahedral	11
Ulrich et al. [35]	1998	Hexahedral and Tetrahedral	10
Niebur et al. [53]	2000	Hexahedral	Iteratively calculated using ratio of effective modulus to element modulus with experimental results (value not stated)
Cui et al. [10]	2006	Hexahedral	10
Van Lenthe et al. [39]	2006	Plate and Rod method	10
Liu et al. [40]	2008	Hexahedral	15
Bevill et al. [36]	2009	Hexahedral	10
Bevill and Keaveny [54]	2009	Hexahedral	10
Guillen et al. [55]	2011	Hexahedral	18
Wang et al. [42]	2013	Hexahedral and Plate and Rod method	15

2.4 Cellular Solids

This section gives an overview of the analytical solutions to macroscopic properties of the lattices investigated in this research, as well as the work on cellular solids and the applicability to trabecular bone modelling. Gibson and Ashby note the similarity of trabecular bone to open-cell lattice structures in appearance and behaviour [6], which in part motivated this research to investigate methods used to account for variation in trabecular bone using idealised open-cell lattice structures with differing properties.

2.4.1 Properties of Cellular Solids

This section gives an overview of the work done on the mechanical properties of cellular solids; paying particular attention to the analytical solutions for the lattices investigated as part of this research that will be used to validate the numerically determined responses in certain directions. Care must be taken in the interpretation of analytical results as they often make assumptions and ignore certain modes of deformation.

The mechanical properties of lattices are influenced by three predominant factors; namely the mechanical properties of the base material (properties of trabecular tissue, properties of aluminium in aluminium foams, etc.), the topology of the lattice and the relative density (ρ^*/ρ_s) where ρ^* is the density of the lattice and ρ_s is the density of the solid [57].

The topology of the lattice importantly determines the dominant deformation mode, which can be either *bending-dominant* or *stretch-dominant*. Most lattices are bending dominant, which causes their stiffness to be well below that of stretch-dominant lattices [57]. Ashby gives an example of a bending-dominant, low-connectivity lattice with a relative density of 0.1 being 10 times less stiff than a stretch-dominant triangular lattice [57].

When mechanically loaded, lattices initially deform elastically until plastically yielding, buckling or brittle fracture of the cell plates or rods occurs. The structure will continue to deform at near constant stress (called the plateau stress) until the cell plates or rods start to impinge against each other. Once the cell walls impinge, the lattice starts to densify and the stress rises sharply [6,57]. Figure 2.8 shows an example stress versus strain curve for cellular solids. This research only deals with the initial elastic region, where the effective Young's modulus is present.

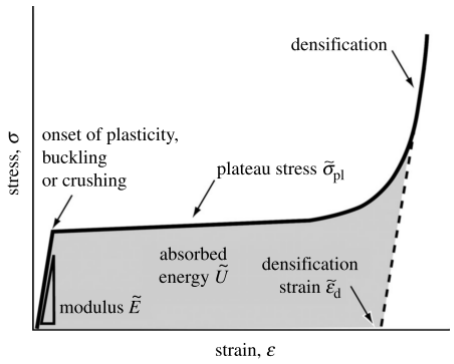

Figure 2.8: Example stress-strain curve for cellular solid [57].

Gibson and Ashby describe properties used to characterise the topology and structure of lattices, similar to how microstructural indices are used to characterise structure in trabecular bone research. Table 2.5 shows an overview of the parameters described.

Table 2.5: Parameters for characterisation of the topology of lattices [6].

Parameter	**Symbol**
Relative Density	ρ^*/ρ_s
Edge Connectivity	Z_e
Mean edges/cell	$\bar{n}$
Largest principal cell dimension	L_1
Smallest principal cell dimension	L_2
Shape anisotropy ratio	$R = L_1/L_2$
Cell wall thickness	t

2.4.1.1 2D Lattices

The elastic properties of many 2D lattices are well understood, in particular the lattices investigated in this research [6, 57, 58]. Gibson and Ashby present analytical solutions for the square, triangular and hexagonal lattices using a unit cell modelling technique, and assuming deformation only by the predominant deformation mode. However, they present the results only for square cross sections [6] and leave out portions of the derivation such that solutions can not be modified for different cross sections. Lawrence [17] derived the relative elastic moduli generally, and provided solutions with circular cross sections. The elastic moduli of these lattices were also derived with lateral confinement [17].

Square lattice along the principal directions, assuming stretch-dominant behaviour:

$$\frac{E^*}{E_s} = \frac{\pi}{4}\left(\frac{d}{l}\right). \tag{2.6}$$

The response of the square lattice is unchanged with lateral confinement.

Triangular lattice along the principal directions (and any other, see Figure 2.9), assuming stretch-dominant behaviour:

$$\frac{E^*}{E_s} = \frac{\pi}{2\sqrt{3}}\left(\frac{d}{l}\right). \tag{2.7}$$

Triangular lattice with lateral confinement:

$$\frac{E^*}{E_s} = \frac{3\sqrt{3}\pi}{16}\left(\frac{d}{l}\right). \tag{2.8}$$

Hexagonal lattice along the principal directions (and any other, see Figure 2.9), assuming bending-dominant behaviour:

$$\frac{E^*}{E_s} = \frac{\sqrt{3}\pi}{4}\left(\frac{d}{l}\right)^3. \tag{2.9}$$

With lateral confinement, the hexagonal lattice becomes stretch dominant:

$$\frac{E^*}{E_s} = \frac{\pi}{8\sqrt{3}}\left(\frac{d}{l}\right), \tag{2.10}$$

where, E^* and E_s are the elastic modulus of the structure and base material respectively, and d and l are the diameter and lengths of the circular beam making up the lattice [17].

It is interesting to note that stretch or axially dominant deformation modes have a linear dependence on the beam aspect ratio (which is proportional to relative density) while the bending-dominant structure, such as the hexagonal lattice, have a cubic dependence on beam aspect ratio.

The triangular and hexagonal lattices are fully isotropic, whereas the square lattice is highly anisotropic having the same properties in the principal directions but a massive reduction in stiffness at off angles [6, 17, 58]. Gibson and Ashby present a polar diagram showing the response of the three lattices loaded at various angles, with the same beam aspect ratio (see Figure 2.9).

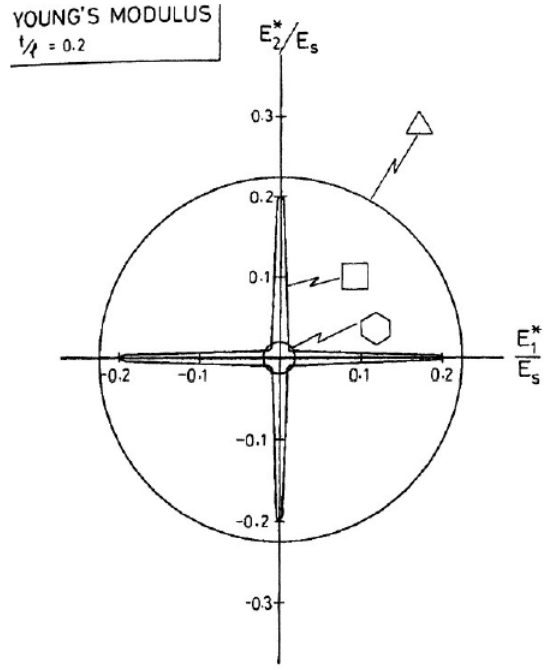

Figure 2.9: Polar plot showing the macroscopic Young's modulus for square, triangular and hexagonal lattices comprised of beams with the same aspect ratio [6].

Lawrence [17] showed the effect of lateral confinement on elastic moduli, which depending on structure can have a simple scaling effect whilst maintaining similar isotropy (see Figure 2.10b) or have a dramatic effect changing the degree of anisotropy (see Figure 2.10a).

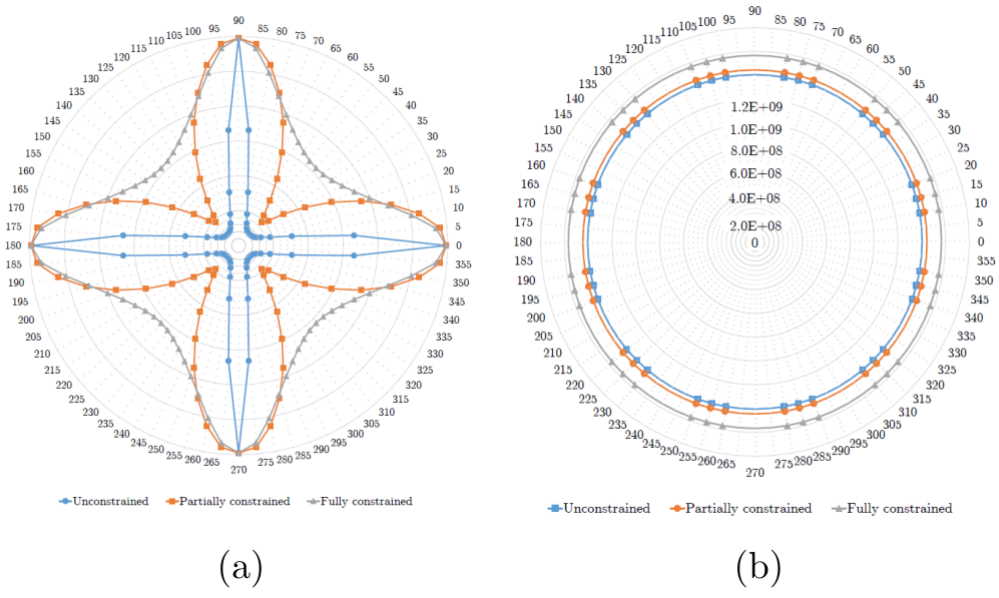

(a) (b)

Figure 2.10: Effect of lateral confinement on elastic moduli for; (a) square and (b) triangular lattices. [17]

2.4.1.2 3D Lattices

Deshpande et al. [59] investigated the effective mechanical properties of the octet-truss lattice. They provide analytical solutions for the octet-truss lattice relative density and elastic moduli, assuming only axial deformation as the contribution from the bending of struts is negligible.

The relative density of the octet-truss lattice (see unit cell in Figure 2.11) is:

$$\bar{\rho} = 6\sqrt{2}\pi\left(\frac{a}{l}\right)^2, \tag{2.11}$$

where a and l are the radius and lengths of the beams respectively. The elastic moduli of the principal directions (p_{1-3} in Figure 2.11) is:

$$\frac{E^*}{E_s} = \frac{\bar{\rho}}{9} = \frac{2\sqrt{2}\pi}{3}\left(\frac{a}{l}\right)^2. \tag{2.12}$$

The structure is anisotropic, with the octet-truss structure having the highest elastic modulus in the p_4 direction, which was similarly derived.

$$\frac{E^*}{E_s} = \frac{\bar{\rho}}{5} = \frac{6\sqrt{2}\pi}{5}\left(\frac{a}{l}\right)^2 \tag{2.13}$$

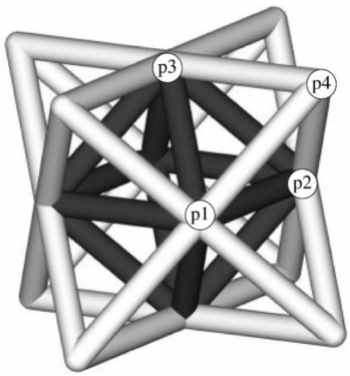

Figure 2.11: Octet-truss unit cell [59].

Zhu et al. [60] analytically derived the effective mechanical properties of the Kelvin cell (tetrakaidecahedron), without considering non-dominant deformation modes negligible. The effective Young's modulus for circular cross sections, with radius r, is;

$$E_{eff} = \frac{3\sqrt{(2)}r^4}{2(1+3r^2)}. \tag{2.14}$$

They also found that the Poisson's ratio approaches 0.5 for low relative densities and that the lattice model is isotropic, unlike the majority of 3D lattices [60].

See Appendix C for the derivation of the cubic lattice in the principal directions.

2.4.2 Cellular Solid Idealisation

Gibson and Ashby attempt to account for the variation that relative density alone cannot account for, using idealised unit cells for two distinct classes of trabecular bone. The classes of bone they considered were highly equiaxed, separated into low and high densities (see Figure 2.12a,b) and stress-orientated, separated into prismatic and parallel plate models (see Figure 2.12c,d).

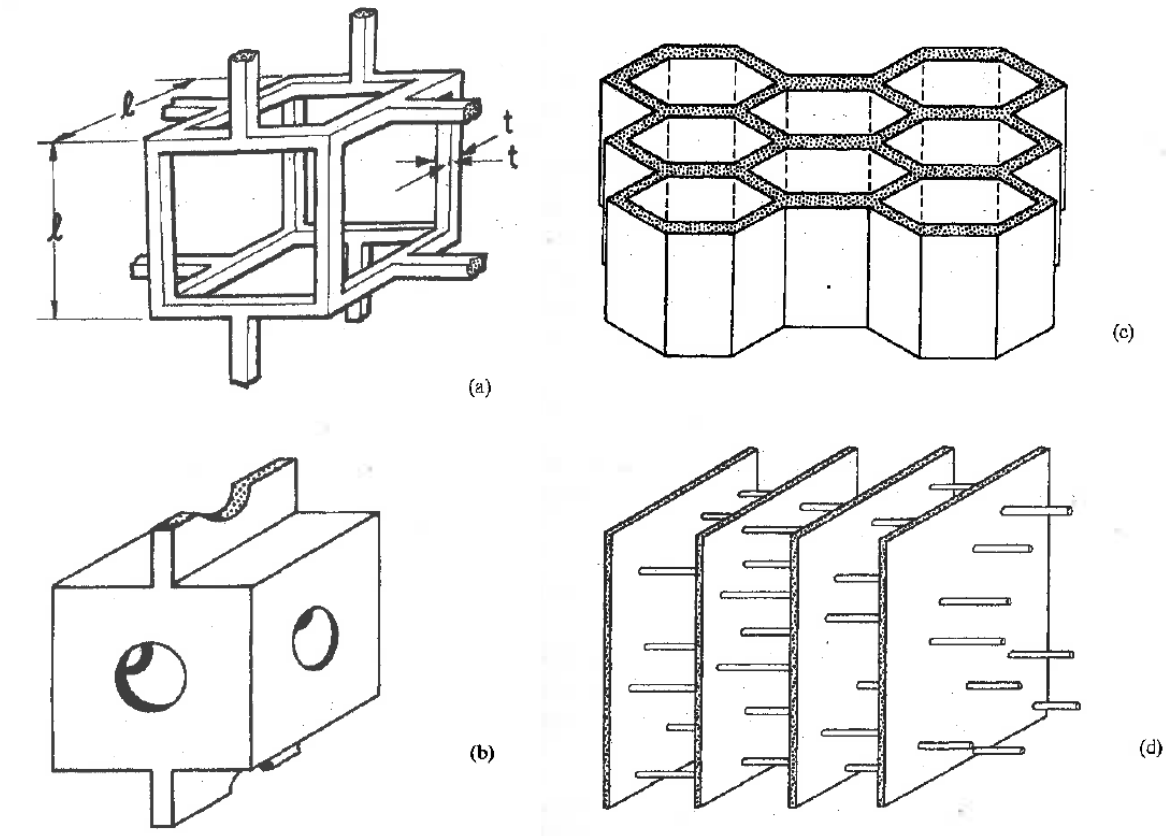

Figure 2.12: Idealised trabecular model for trabecular bone: (a) low density equiaxed structure, (b) high density equiaxed structure, (c) stress orientated prismatic structure, and (d) stress oriented parallel plate structure [6].

The low density equiaxed model was used such that the linear-elastic behaviour is dominated by the bending of the cell walls, which is supported by experimental data [6]. The Young's modulus of this structure is:

$$\frac{E^*}{E_s} = C_1 \left(\frac{\rho^*}{\rho_s} \right)^2, \tag{2.15}$$

where E^* and E_s are the Young's moduli of the structure and material respectively, C_1 is a constant near unity related to the exact cell geometry, ρ^* and ρ_s are the density of the structure and the material respectively [6].

The perforated plate model used to represent the high density equiaxed model which similarly responded in bending. As the perforation is variable, the model can represent everything between a closed cell to a low density equiaxed cell [6]. The Young's modulus of this structure is:

$$\frac{E^*}{E_s} = C_2 \left(\frac{\rho^*}{\rho_s} \right)^a, \tag{2.16}$$

where a varies between 1 and 2 based on the relative diameter of the perforation.

The stress oriented models for trabecular bone differ in that they have distinct Young's moduli based on direction of loading. The Young's modulus for both the prismatic and parallel plate models vary linearly

or cubically depending on loading direction. The Young's moduli for the prismatic model loaded across the prism axis and the parallel plate model loaded normal to the plates is:

$$\frac{E^*}{E_s} = C_3\left(\frac{\rho^*}{\rho_s}\right)^3. \tag{2.17}$$

The Young's moduli for the prismatic and parallel plate models loaded across the cell walls is:

$$\frac{E^*}{E_s} = C_4\left(\frac{\rho^*}{\rho_s}\right). \tag{2.18}$$

This model predicts that the Young's moduli of trabecular bone samples should lie between a line with gradient 1 and 3 passing through the point corresponding to the density of whole bone, corresponding to linear and cubic dependence respectively (see Figure 2.13a) when plotted against density. Figure 2.13 demonstrates that the model captures much of the data, however a significant portion lie outside of this region [61]. Gibson and Ashby [6] account for the deviation in Figure 2.13a by considering the effects of strain-rate. The stress-oriented model, which predicts the Young's moduli plotted against data should vary linearly for longitudinal moduli and cubically for transverse moduli [6].

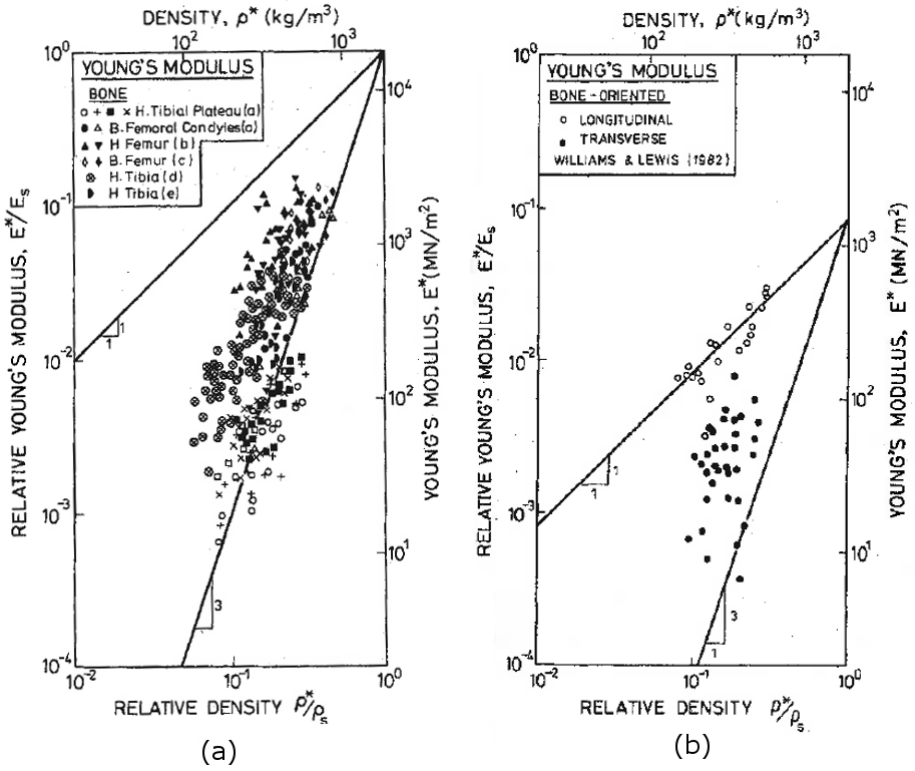

Figure 2.13: Young's moduli of trabecular bone plotted against density; (a) of unspecified orientation, (b) transverse and longitudinal directions [6].

Gibson and Ashby assume that the material properties of trabecular bone (not the structural property) is the same as cortical bone and thus their models can be extrapolated to the behaviour of cortical bone. This is shown in the line of best fit drawn through the point corresponding to whole bone. This is a common assumption however it does not fit with more recent experimental data in attempts to capture the mechancial properties of individual trabeculae [20, 44, 51, 62]. This is more likely the reason that a significant portion of the data falls outside the predicted region. It is also interesting to note that the constants C_{1-4} which are used to describe the geometry of the models could be thought of as microstructural indices used in particular combinations.

2.5 Homogenisation and Elasticity Transformation

The lattice response is linear elastic until plastic yielding, buckling or brittle fracture of the cell walls (see Figure 2.8) if the base material is linear elastic [6], which is the region of interest for this research. As the response is linear elastic, effective properties for Young's modulus, shear modulus and Poisson's ratio could be used in an the elasticity tensor for a model using solid elements [63].

Ptochos et al. [63] used a homogenised model on a body centered cubic lattice, based of effective material properties which were analytically calculated, finding very high correlation with their discrete model with dramatic decrease in computational cost. Their discrete model had 40,960 element while their homogenised model only used 512 elements.

Their investigation did not consider the anisotropy of the effective properties and therefore the approach needs to be extended for use in this research. The anisotropy can be determined by taking advantage of inherent symmetries in the elasticty tensor, and transforming the elasticity tensor to different coordinate systems such that it would respond correctly to loading in the new coordinate system [64].

Stress and strain are both symmetric second rank tensors, as they are defined by two distinct properties; stress is defined by a traction vector and the normal of the surface on which the traction acts and strain is defined by a change in length in a given direction and the original reference direction [65]. Stress and strain are field tensors, distinct from property tensors, as arbitrary stresses (and resulting strains) can be applied that do not have to conform to crystal symmetries [64].

The elasticity tensor is defined as the relationship between the stress and strain, and for linear elastic materials the elasticity tensor is defined by Hooke's Law [65]. As stress and strain are both second rank tensors, the elasticity tensor is therefore a fourth rank tensor. The transformation of the elasticity tensor is done by transforming the stress and strain to different coordinate systems.

The transformation of stress and strain is complicated by the conventional use of Voigt notation, which is a condensed notation of stress and strain that take advantage of symmetries due to equilibrium. The stress tensor can be equated to a stress vector as follows:

$$\begin{bmatrix} \sigma_{11} & \sigma_{12} & \sigma_{13} \\ \sigma_{21} & \sigma_{22} & \sigma_{23} \\ \sigma_{31} & \sigma_{32} & \sigma_{33} \end{bmatrix} = \begin{bmatrix} \sigma_1 = \sigma_{11} \\ \sigma_2 = \sigma_{22} \\ \sigma_3 = \sigma_{33} \\ \sigma_4 = \sigma_{23} \\ \sigma_5 = \sigma_{13} \\ \sigma_6 = \sigma_{12} \end{bmatrix} \tag{2.19}$$

The transformation matrix for the 6x1 stress vector is derived by comparing the coefficients of stress tensor transformed by α_{ij} to the stress vector multiplied by a 6x6 transformation matrix a.

The transformation of the stress tensor is:

$$\sigma'_{ij} = \alpha_{il}\alpha_{jk}\sigma_{kl}, \tag{2.20}$$

where σ'_{ij} is the stress in the new coordinate system, α is the transformation matrix and σ_{ij} is the stress in the original coordinate system. The stress vector would have to be transformed by a 6x6 matrix (a)) such that:

$$\begin{bmatrix} \sigma'_1 \\ \sigma'_2 \\ \sigma'_3 \\ \sigma'_4 \\ \sigma'_5 \\ \sigma'_6 \end{bmatrix}' = \begin{bmatrix} a_{11} & a_{12} & a_{13} & a_{14} & a_{15} & a_{16} \\ a_{21} & a_{22} & a_{23} & a_{24} & a_{25} & a_{26} \\ a_{31} & a_{32} & a_{33} & a_{34} & a_{35} & a_{36} \\ a_{41} & a_{42} & a_{43} & a_{44} & a_{45} & a_{46} \\ a_{51} & a_{52} & a_{53} & a_{54} & a_{55} & a_{56} \\ a_{61} & a_{62} & a_{63} & a_{64} & a_{65} & a_{66} \end{bmatrix} \begin{bmatrix} \sigma_1 \\ \sigma_2 \\ \sigma_3 \\ \sigma_4 \\ \sigma_5 \\ \sigma_6 \end{bmatrix} \tag{2.21}$$

The coefficients a_{ij} can be determined by comparing expanded out transformed coefficients of the stress vector and tensor, equating the terms using Equation 2.19. For the first stress component, $\sigma'_{11} = \sigma'_1$, it follows that:

$$\begin{aligned} \sigma'_1 &= a_{11}\sigma_1 + a_{12}\sigma_1 + \cdots + a_{16}\sigma_6 \\ \sigma'_{11} &= \alpha_{11}^2\sigma_{11} + \alpha_{11}\alpha_{12}\sigma_{12} + \alpha_{12}\alpha_{11}\sigma_{21} + \cdots + \alpha_{12}^2\sigma_{22} + \ldots \end{aligned}, \tag{2.22}$$

By grouping terms it shows that $a_{11} = \alpha_{11}^2, a_{12} = \alpha_{12}^2, a_{16} = 2\alpha_{11}\alpha_{12}$. Following the same procedure the rest of the coefficients of the transformation of the stress vector can be determined.

The strain vector in Voigt notation is:

$$\begin{bmatrix} \epsilon_{11} & \epsilon_{12} & \epsilon_{13} \\ \epsilon_{21} & \epsilon_{22} & \epsilon_{23} \\ \epsilon_{31} & \epsilon_{32} & \epsilon_{33} \end{bmatrix} = \begin{bmatrix} \epsilon_1 = \epsilon_{11} \\ \epsilon_2 = \epsilon_{22} \\ \epsilon_3 = \epsilon_{33} \\ \epsilon_4 = 2\epsilon_{23} \\ \epsilon_5 = 2\epsilon_{13} \\ \epsilon_6 = 2\epsilon_{12} \end{bmatrix} \tag{2.23}$$

The transformation of the strain vector could be achieved in the same fashion as the stress vector, however by utilising the fact that strain energy density, W is a scalar quantity it is invariant to changes in basis $W' = W$.

$$\begin{aligned} W &= W' \\ W = \epsilon^T\sigma = \epsilon^T(a^{-1}a)\sigma &= \epsilon^T a^{-1}(a\sigma) \\ W &= \epsilon^T a^{-1}\sigma' \\ W' &= \epsilon'\sigma' \end{aligned} \tag{2.24}$$

Therefore $\epsilon' = \epsilon^T a^{-1} = (a^{-1})^T\epsilon$. The transformation of the elasticity tensor can be achieved using the transformations of the stress and strain vectors (see Chapter 4).

Chapter 3

Discrete Modelling Methodology

3.1 Overview

The macroscopic stiffnesses of arbitrary lattices with arbitrary loading and boundary conditions were determined using finite element analysis, solved in LS-DYNA using beam elements. The approach used was to generate an oversized lattice, which is rotated and cropped to a specified test region. The lattice was rotated, in lieu of the loading angle, such that the lattice could be loaded in varying directions whilst maintaining an easily definable boundary. The lattices are subjected to a prescribed displacement, ensuring constant macroscopic strain, and the summation of forces result in a volume averaged stress which is then used to calculate the effective stiffness, defined as:

$$E_{eff} = \frac{\sigma_{avg}}{\epsilon_{prescribed}}, \tag{3.1}$$

where $\epsilon_{prescribed}$ is the prescribed macroscopic strain, σ_{avg} is the volume averaged stress and E_{eff} is the effective stiffness of the lattice.

3.2 Mesh Generation

A unit cell approach was used to generate the periodic lattices. The smallest repeating structure (unit cell) is manually defined, along with the required number of unit cells to make up the full lattice in X,Y,Z. The unit cell is copied into the prescribed positions and neighbouring cells have elements and nodes stitched together, removing duplicate elements and nodes. An example unit cell is shown in Figure 3.1.

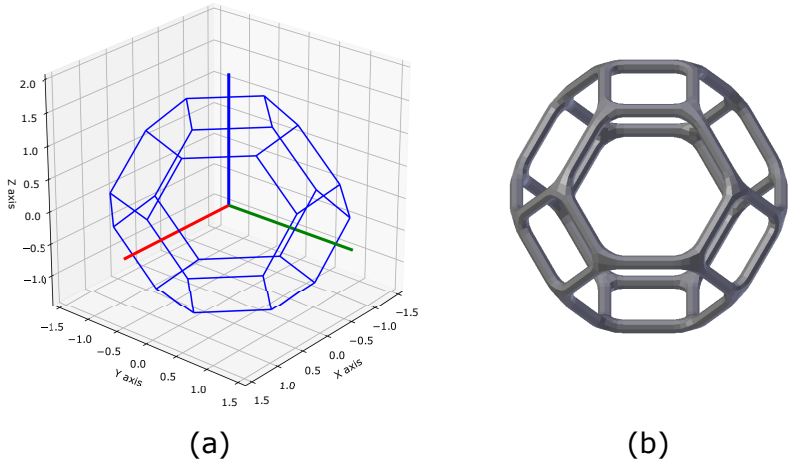

Figure 3.1: Tetrakaidecahedron Unit Cell: (a) beam representation (b) solidified representation.

To ensure that the time taken to add a new cell to the lattice did not increase as the size of the lattice increased, any data reading of the whole lattice was limited. This was achieved by storing node and element data in cell objects. Whenever a new cell is added to the lattice only the neighbouring cell object data is required.

The cells are all stored in a dictionary, or associative array, where the list of cells is indexed by the position of the cell rather than a range of numbers as in a conventional array. This makes the time to find a cell at a given position plateau, regardless of number of cells in the list. Algorithm 1 shows the process of adding a new cell to the lattice.

Algorithm 1 Mesh Generation - Add New Cell

```
procedure NewCell(newPosition)
    [nodesToAdd, elementsToAdd] ← UnitCell.Transform(newPosition)
    for position in adjacentPositions do                ▷ Finding all neighbouring cells
        if position in allCells.positions then
            neigbour ← allCells(position)
            nodesToCheck ← neigbour.nodes
            elementToCheck ← neigbour.elements
    for node in nodesToAdd do                           ▷ Adding new nodes
        if node in nodesToCheck then                    ▷ Node exists, don't add
            nodeID ← nodesToCheck.ID where nodeToCheck == node
            elementToAdd.nodeID ← nodeID where elementToAdd.nodeID == nodeID
        else
            addNode(node)
    for element in elementsToAdd do                     ▷ Adding new Cell
        if element not in elementsToCheck then
            addElement(element)
    addCell()                                           ▷ Adding this cell to dictionary
```

The geometry of each unit cell dictates which neighbouring cells can be attached. For example the unit cell shown in Figure 3.1 can only attach to the 6 cells sharing faces, as there are no corner or edge nodes. Figure 3.2 shows the average time to add a cell to a lattice as a function of total number of cells for two unit cells.

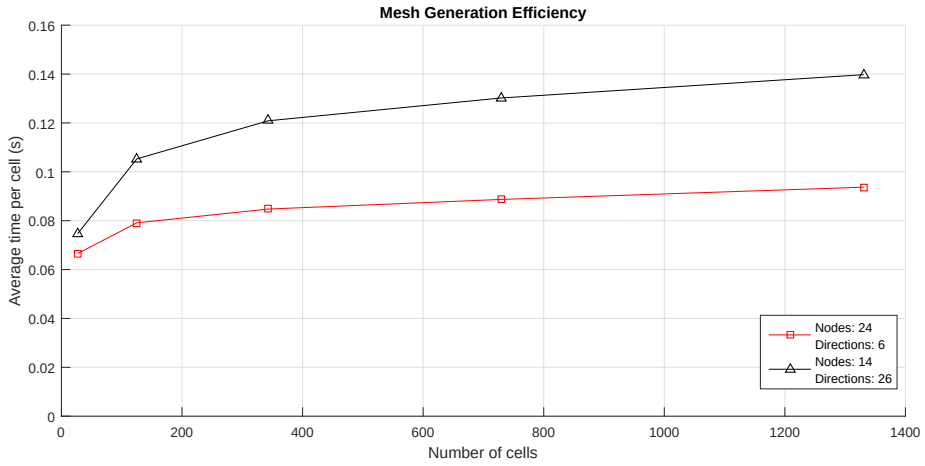

Figure 3.2: Average time to add a new cell to a lattice, for two different unit cells

Figure 3.2 demonstrates that the average time to add a new cell is consistently higher for the unit cell that has only 14 nodes and 26 potential neighbouring cells than the more complex unit cell (14 nodes) with fewer potential neighbouring cells. This indicates that speed of mesh generation has a greater dependency on the number of potential neighbours than the complexity of the unit cell. Given that certain macroscopic topologies can be described by more than one unit cell. Care must be taken in defining a unit cell such that the number of potential neighbouring cells is minimised. It can also be seen that for both the unit cells shown, the average time taken to add a new cell plateaus.

3.2.1 Previous Mesh Generation Approach

The first mesh generation approach was to use recursive generation rule-sets. The approach required all the nodes of the lattice to be placed first, then a set of recursive rules would connect all the nodes to form the required lattice. This worked well for 2D lattices, however as the process was inherently abstracted from the actual geometry it became increasingly difficult for 3D lattices.

The current method was found to be more intuitive and could be used for any periodic lattice structures more readily than the generation rule-set approach.

3.3 Mesh Cropping

The oversized lattices need to be cropped to a specified test region. Efficiency of the cropping procedure was a concern as the number of nodes and elements become very large in the larger lattices, which is compounded by the large number of rotations required. For example a $35 \times 35 \times 35$ cell Kelvin cell lattice has 529616 nodes and 1044116 elements, and 331 rotations where required to achieve a reasonable resolution in 3D. It was important to find a method to structure the nodal coordinate data such that it could be efficiently searched.

3.3.1 Spatial Hashing

There are many options for ordering spatial data however as the structure would need to be created for each rotation, the efficiency of building the structure was the limiting factor. A spatial hash was decided on as rebuilding the hash is only O(N)[1], with N data points, where a conventional tree-like structure like a binary space partition is at best O(Nlog(N)) to rebuild the tree [66].

Spatial Hashing is a method to project 2D or 3D data into a 1D dictionary (also known as an associative array or hash table). The domain of the positional data is subdivided into a uniform grid, and the positional data is labelled with a unique key corresponding to the grid space it falls in [66].

The hash table is an indexed list of data points that fall within a grid space for each grid space in the domain, which is indexed by the unique key. This effectively sorts the data into 'buckets' of neighbouring data, which are efficiently recalled by the key. Figure 3.3 is an example of 14 points (illustrated as encircled letters) being hashed over a 5x5 grid (left) into a hash table (right), illustrating how positional data is stored by a spatial hash.

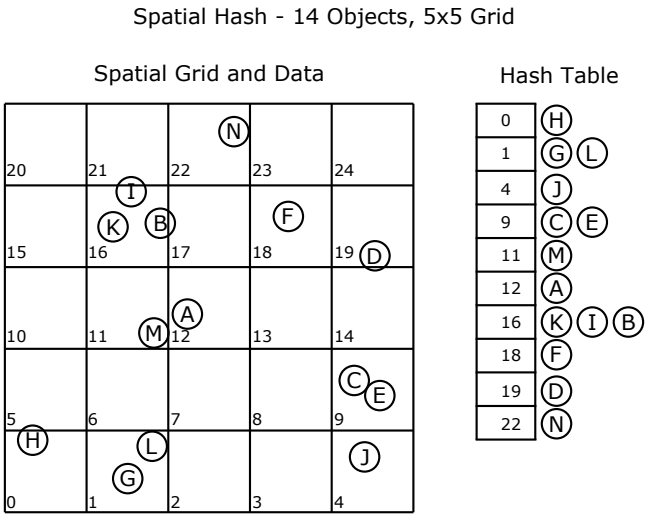

Figure 3.3: Example of Spatial Hash.

[1] Big O notation is a measure of computational efficiency, representing the worst case scenario

The benefit is, that once you have created the spatial hash, queries to find positional data become very fast. For example, Table 3.1 shows the difference in computational time between using a spatial hash to decrease search space (including time to generate the spatial hash) and a brute force search to find all points a specified distance away from a line.

Table 3.1: Spatial Hash Efficiency Example.

Number of points	Brute Force (s)	Spatial Hash (s)
1000	0.091	0.011
10000	0.890	0.040
100000	8.700	0.410

Table 3.1 demonstrates that the spatial hash creation is O(N), or increases linearly in time with increased number of points and shows that for simple tasks the efficiency increase using a spatial hash is considerable, within the expected range of nodes.

3.3.2 Rotations and Angle Series Definition

Rotation matrices are easily definable in 2D:

$$R(\theta) = \begin{bmatrix} \cos(\theta) & -\sin(\theta) \\ \sin(\theta) & \cos(\theta) \end{bmatrix}, \tag{3.2}$$

where $R(\theta)$ is the rotation matrix and θ is the angle of rotation; however a convention must be chosen and adhered to in defining 3D rotations.

Euler angles rotations define any arbitrary rotation in 3D space as a series of rotations around each axis. Any orientation is then a function of 3 Euler angles $R(\psi, \theta, \phi)$. Further, the order in which the axis rotation matrices are multiplied must be chosen and adhered to as $R_x R_y R_z \neq R_z R_x R_y$. The generalised 3D rotation convention used is:

$$\begin{aligned} R(\psi,\theta,\phi) &= R_z(\phi) R_{y'}(\theta) R_{x'}(\psi) \\ R(\psi,\theta,\phi) &= \begin{bmatrix} \cos(\phi) & -\sin(\phi) & 0 \\ \sin(\phi) & \cos(\phi) & 0 \\ 0 & 0 & 1 \end{bmatrix} \begin{bmatrix} \cos(\theta) & 0 & -\sin(\theta) \\ 0 & 1 & 0 \\ \sin(\theta) & 0 & \cos(\theta) \end{bmatrix} \begin{bmatrix} 1 & 0 & 0 \\ 0 & \cos(\psi) & -\sin(\psi) \\ 0 & \sin(\psi) & \cos(\psi) \end{bmatrix}, \end{aligned} \tag{3.3}$$

where $R(\psi, \theta, \phi)$ and (ψ, θ, ϕ) are the angles of rotation about (z, y', x') respectively; (y', x') are the rotated y and x . Figure 3.4 shows subsequent steps of an axis being rotated via Equation 3.3.

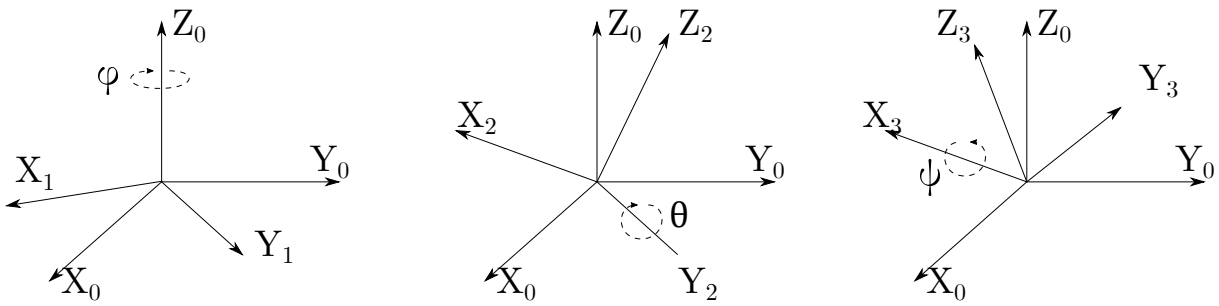

Figure 3.4: 3D rotation by Euler angle rotations. Showing effect of each subsequent rotation matrix.

The following is the method in which the series of angles to fully describe the anisotropy over a region are defined. The definition of the angle series in 2D is trivial with only one angle to increment. The series is incremented with between a defined start and end angle with a constant step size. As with the rotation matrix, the definition of series of angles becomes more complex in 3D.

To capture the mechanical response in 3D, the angle series needed to fully cover the positive octant; the lattices investigated have reflective symmetry and therefore the positive octant alone is sufficient. As generalised Euler angles are used, a simple incrementing scheme would not easily work to fully cover the positive octant with near equispaced points.

To achieve this, the set of Euler angles that rotate the loading direction onto a set of vectors corresponding to points linearly spaced across the surface of a cube (see Figure 3.5a) are calculated. The Euler angles required are calculated from the matrix that rotates the loading direction onto each point.

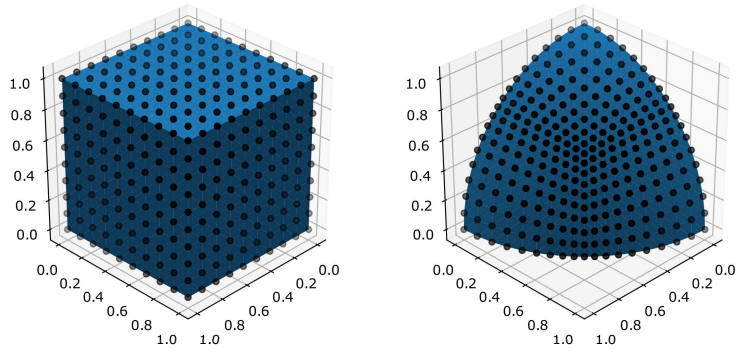

(a) (b)

Figure 3.5: Scheme for generating 3D angle series: (a) cube with linearly spaced vertices (b) points generated via rotating direction.

The following procedure is used to calculate the rotation matrix that rotates a vector $\mathbf{A}$, to another vector $\mathbf{B}$. Given two arbitrary unit vectors $\mathbf{A}$ and $\mathbf{B}$, the rotation from $\mathbf{A}$ to $\mathbf{B}$ can trivially be defined on the plane with the normal $\mathbf{A} \times \mathbf{B}$ as:

$$U = \begin{bmatrix} \cos(\beta) & -\sin(\beta) & 0 \\ \sin(\beta) & \cos(\beta) & 0 \\ 0 & 0 & 1 \end{bmatrix} = \begin{bmatrix} \mathbf{A} \cdot \mathbf{B} & -||\mathbf{A} \times \mathbf{B}|| & 0 \\ ||\mathbf{A} \times \mathbf{B}|| & \mathbf{A} \cdot \mathbf{B} & 0 \\ 0 & 0 & 1 \end{bmatrix}, \tag{3.4}$$

where β is the planar angle between vectors $\mathbf{B}$ and $\mathbf{B}$. The method of calculating U relies on linear algebra rather than evaluating trigonometric functions as linear algebra is more computationally efficient.

U is the rotation on the plane with the normal $\mathbf{B} \times \mathbf{B}$, and not in respect to the normal basis x, y, z, thus U has to be transformed into the normal basis.

U is in the basis defined by $\mathbf{A}$, the orthographic projection of $\mathbf{B}$ onto $\mathbf{A}$ and $\mathbf{A} \times \mathbf{B}$. Thus the change of basis matrix from this basis to the normal basis is:

$$D = \begin{bmatrix} \mathbf{A} & \frac{\mathbf{B}-(\mathbf{A}\cdot\mathbf{B})\mathbf{A}}{||\mathbf{B}-(\mathbf{A}\cdot\mathbf{B})\mathbf{A}||} & \mathbf{B} \times \mathbf{A} \end{bmatrix} \tag{3.5}$$

Therefore, the rotation from $\mathbf{A}$ to $\mathbf{B}$ in the normal basis is:

$$R(\psi, \theta, \phi) = DUD^{-1} \tag{3.6}$$

The rotation matrix calculated in Equation 3.6 is equated to normal rotation matrix (Equation 3.3). The Euler angles are calculated from components of the expanded rotation matrix in 3D (Equation 3.7).

$$R(\psi,\theta,\phi) = \begin{bmatrix} \cos(\phi)\cos(\theta) & -\sin(\phi)\cos(\psi)+\cos(\phi)\sin(\theta)\sin(\psi) & \sin(\phi)\sin(\psi)+\cos(\phi)\sin(\theta)\cos(\psi) \\ \sin(\phi)\cos(\theta) & \cos(\phi)\cos(\psi)+\cos(\phi)\sin(\theta)\sin(\psi) & -\cos(\phi)\sin(\psi)+\sin(\phi)\sin(\theta)\cos(\psi) \\ -\sin(\theta) & \cos(\theta)\sin(\psi) & \cos(\theta)\cos(\psi) \end{bmatrix} \tag{3.7}$$

$$\begin{aligned} \psi &= \arctan\left(\frac{R_{32}}{R_{33}}\right) \\ \theta &= \arctan\left(\frac{-R_{31}}{\sqrt{R_{32}^2+R_{33}^2}}\right) \\ \phi &= \arctan\left(\frac{R_{21}}{R_{11}}\right) \end{aligned} \tag{3.8}$$

3.3.3 Boundary Element Deletion Cropping Procedure

The cropping procedure requires an oversized lattice, and an axis aligned bounding box that will become the test region (see Figure 3.6a). It is important that the size of the bounding box is defined such that at the extremes of rotation the bounding box stays fully within the lattice. This is achieved by enforcing the constraints:

$$l_b^{2D} < \frac{l_l}{\sqrt{2}} \quad ; \quad l_b^{3D} < \frac{l_l}{\sqrt{3}}; \tag{3.9}$$

where l_b^{2D} and l_b^{3D} are the side lengths of the bounding box for 2D and 3D respectively, and l_l is the shortest dimension of the lattice. This ensures that the length of the diagonal of the bounding box must be smaller than the shortest edge of the lattice.

The lattice is rotated by multiplying each nodal position vector with a rotation matrix (see Figure 3.6b). The lattice is rotated as the mechanical anisotropy is of particular interest, however any transformation can be applied. The same method can be used to investigate other effects, such as imparting stretch to investigate the effects of geometric anisotropy on mechanical response.

Once the mesh has been rotated, the spatial hash is created and used to quickly cull nodes (see Figure 3.6c). The bounding box is used with the spatial hash to classify all the external nodes as nodes that are one grid space away from the edges of the bounding box. The grid size of the spatial hash is set to 1 element length, such that it is ensured that no classified external nodes are connected to a node inside the bounding box. These external nodes are deleted (see Figure 3.6d).

The identification numbers associated with each node that is referenced by the list of elements and used in the construction of the stiffness matrix, are kept static during the cropping process. By using static node ID numbers, as opposed to numbering the nodes based on their position in the nodal list; the element list does not need to be edited whenever nodes are deleted, which dramatically improves computational efficiency.

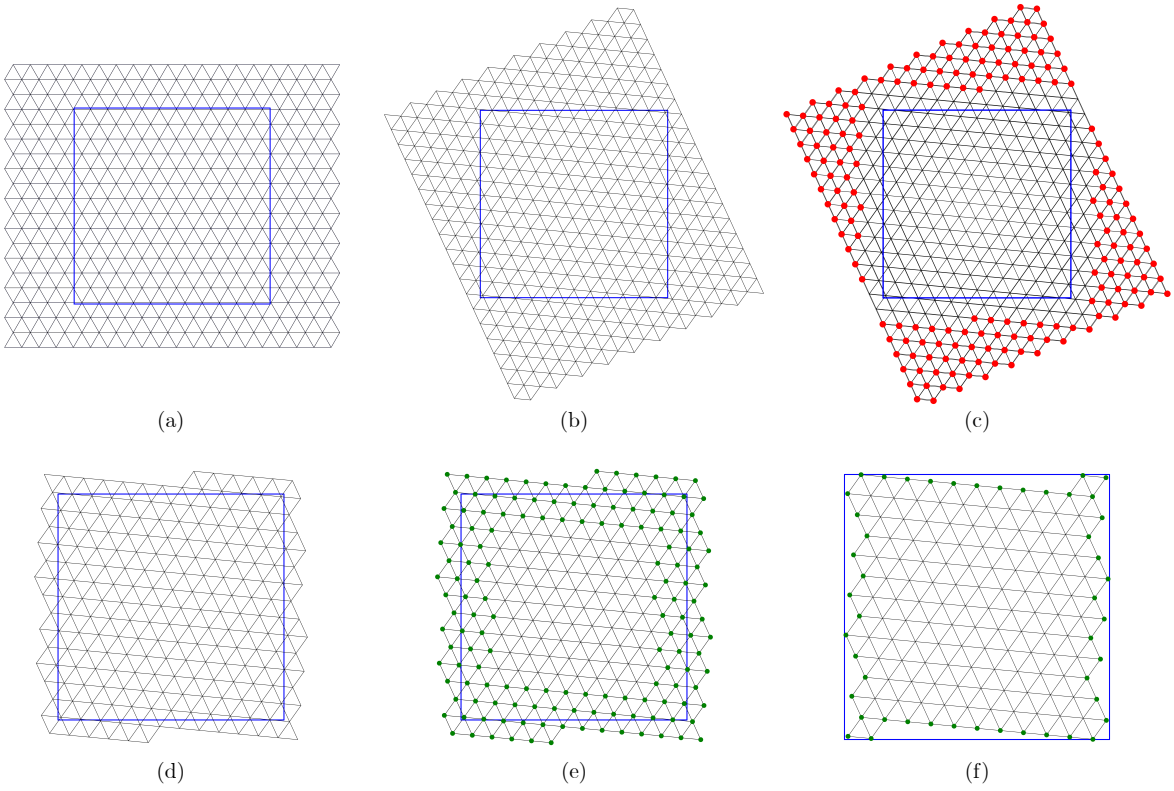

Figure 3.6: Cropping Procedure: (a) Original lattice and bounding box (b) Rotated lattice (c) External nodes classified (d) External nodes deleted (e) Potential boundary nodes identified (f) External nodes deleleted and boundary correctly classified

Once the external nodes are deleted, potential boundary nodes are identified to minimise the number of nodes that need further processing (see Figure 3.6e). The potential boundary nodes are found by finding the difference between the set of all nodes and the sets of external nodes and internal nodes (see equation 3.10). The internal node set is found in a similar method to the external nodes.

$$N_{\text{boundary}} = N_{\text{all}} - (N_{\text{ext}} \bigcup N_{\text{int}}) \tag{3.10}$$

The set of potential boundaries are processed to remove all nodes outside of the bounding box, whilst characterising the nodes into sets corresponding to the closest edge/surface of the boundary box. The boundaries are characterised by finding the closest boundary to an external node in the potential boundary set, then tagging all nodes connected and finally deleting the external node (see Algorithm 2). This effectively tracks the boundary inwards as the external nodes are deleted.

After Algorithm 2, the mesh has a fully classified boundary and is fully within the bounding box (see Figure 3.6f). The last processing step ensures that all boundary nodes are part of a closed unit cell. This is to ensure that the predominant deformation mode for the given lattice is maintained at the boundary. To do this, all boundary nodes connected to too few nodes are removed.

Algorithm 2 Mesh Generation - Boundary Classification

```
procedure ClassifyBoundary(potentialBoundarySet, bounds)
    nodesToRemove ← []
    dim ← potentialBoundarySet.dimension
    boundaryNodes ← [[[],[]] for x in range(dim)]          ▷ Creates sized array 2D/3D
    for i in potentialBoundarySet do
        if not bounds.IsPointWithin(nodes[i]) then
            for d in dim do
                if bounds.extents[1][d] <nodes[i][d] then
                    boundaryNodes[d][1].append(i)
                    break
                else if bounds.extents[0][d] >nodes[i][d] then
                    boundaryNodes[d][0].append(i)
                    break
            nodesToRemove.append(i)
    removeNodes(nodesToRemove)
    return boundaryNodes
```

3.3.4 Boundary Element Intersection Cropping

Another approach to cropping is to cut the elements that cross the defined bounding box, placing a new node on the boundary. This has the benefit of having nodes placed directly along the boundary, which are easier to search for and result in an easily definable bounding size. Figure 3.7 shows the result of a 2D triangular mesh cropped using exact cropping.

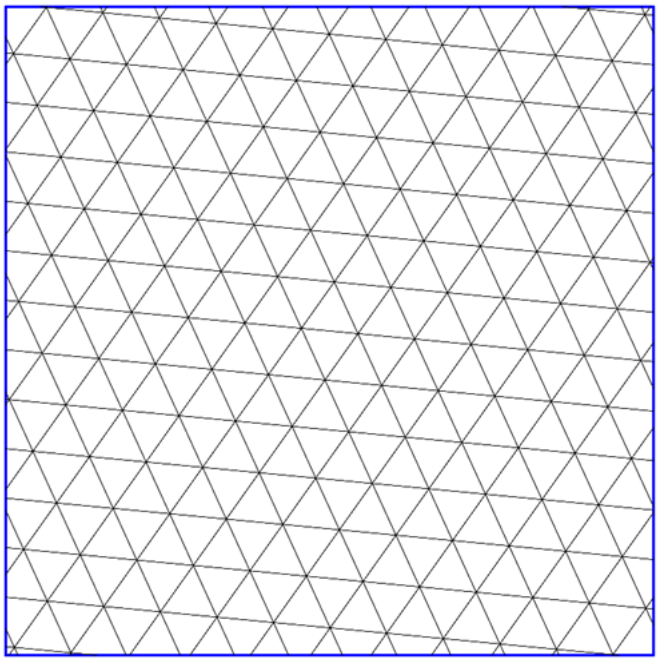

Figure 3.7: Rotated 2D triangular lattice cropped using exact cropping.

This method follows the same procedure as described previously until the set of potential boundary nodes are identified (Figure 3.6). The set of potential boundary nodes are searched to find elements with one internal and one external node to find elements which cross the boundary. All elements crossing the boundary are cropped using the Liang-Barsky algorithm [67].

This method potentially results in extremely small elements that could cause numerical instabilities. To overcome this a tolerance was specified and all boundary elements were searched and collapsed into a single node if their length was under the tolerance. This does result in slightly irregular geometry at the boundary, but the effect of the irregularities was smaller than the numerical instabilities.

A comparison of the two boundary cropping techniques are shown in Section 6.2. It was decided that the comparison of boundary cropping methods would not include stitching the edge elements to 'repair' the boundary of the element intersection cropping method. The concern was that the repair would stiffen the boundary and the structure would not take all of the load, causing an overall stiffer response.

3.4 Finite Element Model Definition

This section outlines the particulars of the finite element model used in LS-DYNA. The mesh data was formatted into the required .k files for LS-DYNA using code written in Python. As each calculation of effective properties required potentially hundreds of FE simulations, manually setting up and running each was not feasible. To this end, code was written to set up all the FE simulations, saving them in a hierarchical file structure. Finally a batch file is created that automatically steps through the file tree and runs every simulation.

As the effects of the lattice geometry on global properties were of interest, the model was kept as simple as possible. To this end, an orthotropic elastic material model was used and as time dependant effects were not of interest it was solved as a static problem using the implicit solver in LS-DYNA. A linear Timoshenko beam with exact stiffness was used as the element type (ELFORM 13 in LS-DYNA). Figure 3.8 shows an overview of the cards used in the model and which cards are used in the definition of others. See Appendix B for exact LS-DYNA implementation.

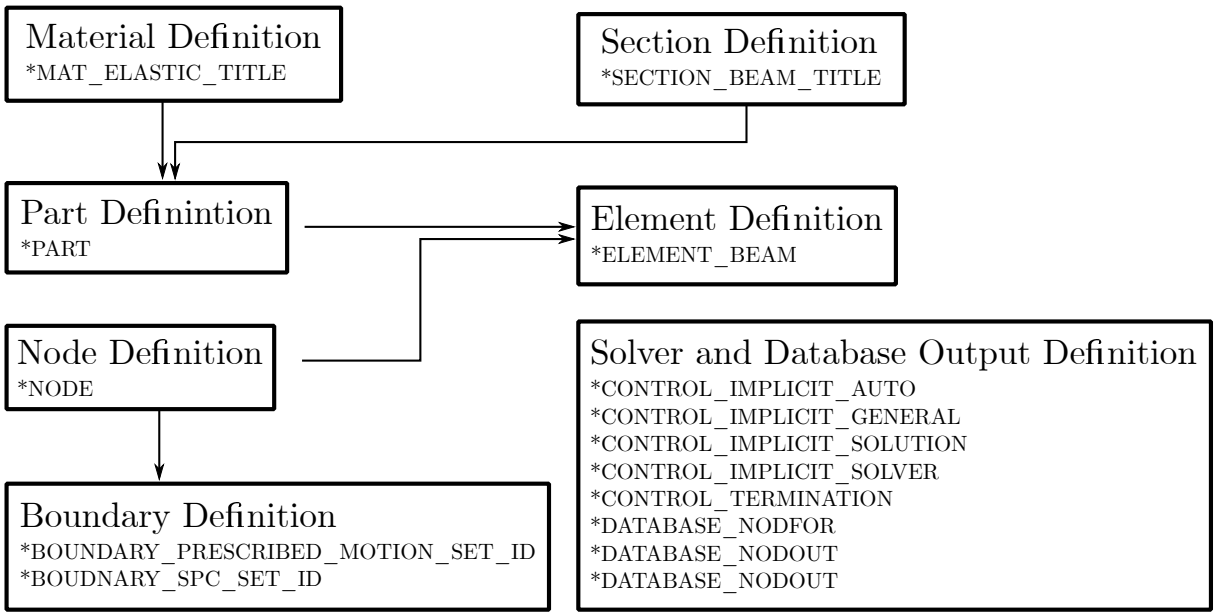

Figure 3.8: LS-DYNA implementation overview.

The beam properties were similarly defined as simply as possible with a unit length, a circular cross section and a 1:10 aspect ratio. Analytical derivations of macroscopic properties show the aspect ratio of the lattice beams are an important determining factor [6]. Thus it is kept constant at $\frac{d}{l} = 0.1$ for all lattices and simulations.

The beam element definition in LS-DYNA requires a 3rd node that defines the local coordinates (orientation of cross section). The 3rd nodes position is defined globally. As perpendicular circular cross sections are to be used, the 3rd node is calculated by finding a vector perpendicular to the element which is then added to the first node.

The material properties use the Young's Modulus, Poisson's ratio and density of steel, chosen to ensure that no numerical instabilities where caused by over or understiff material. Table 3.2 shows the values used in the model.

Table 3.2: FE model properties.

Material Properties	
Young's Modulus	2×10^{10} Pa
Poisson's Ratio	0.3
Density	2500 kg/m^3
Beam Geometry	
Length	1 m
Diameter	0.1 m
Area	0.0078540 m^2
Second Moment of Area	4.909×10^{-6}m^4

The area and second moment of area were calculated using the beam diameter with a circular cross section. The model was set up in LS-DYNA with the material properties and solver preferences defined and stored in a separate file to the geometry definitions. This was such that unnecessary data is not copied and more importantly, that the simulations could be rerun with different properties with only one file having to be changed (opposed to the hundreds of geometry files needing to be recreated).

The beams did not have internal rotational constraints (pin-jointed), however the boundary did have rotational constrains. This was due to the symmetry of the structure cancelling out moments, causing zero rotation internally. The boundary was constrained such that it acted as if it was within a larger structure.

3.4.1 Compression Constraint

The model is subjected to two compression constraint types, namely unconstrained and fully constrained (see Figures 3.9 and 3.10 respectively). The two constraint types were used to investigate the range of lattice behaviour in trabecular bone, with unconstrained and fully constrained responses approximating the trabecular bone at the marrows 'free' surface and at the cortical bone surface respectively. The two constraint types were considered also as the behaviour of open cell lattice structures more sensitive to lateral confinement than simple elastic solids. For example, adding a lateral confinement can change the predominant deformation mode of the lattice and by investigating these two constraint types that behaviour is captured.

Unconstrained behaviour allows free lateral motion by only having two prescribed boundaries, and one fully constrained node to prevent rigid body motion. This constraint is used in determining effective Young's modulus, being used in closed form analytical definitions [6, 63] as no additional stiffness is added via a lateral constraint. Therefore the stiffness calculated in using this constraint type is used in homogenisation (see Section 2.5). Poisson's ratio is determined using this constraint type.

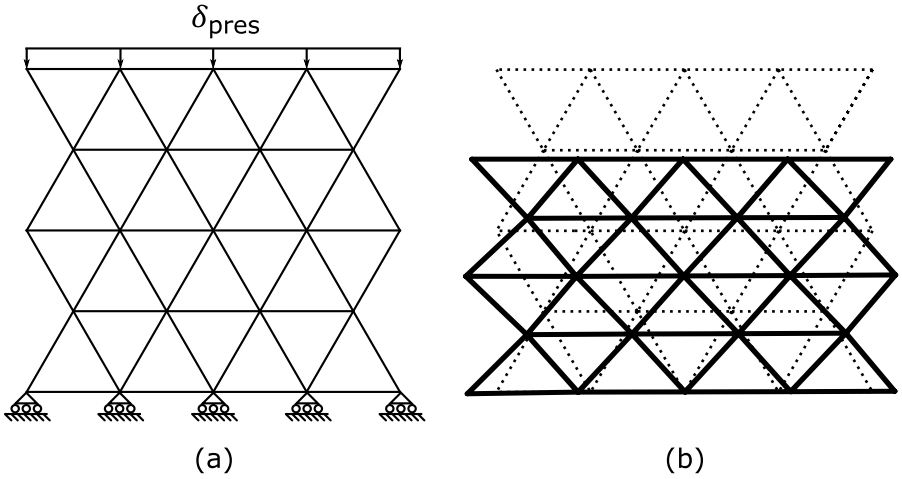

Figure 3.9: (a) Unconstrained compression type (b) example deformation solved in LS-DYNA.

The second compression constraint is referred to as fully constrained (see Figure 3.10). This constraint type disallows any macroscopic lateral deformation, caused by the Poisson's effect, by forcing a zero displacement perpendicular to the loading direction on side boundaries. This is not the same as uniaxial strain where all displacement is in one direction, as the fully constrained boundary type only constrains the surfaces of the lattice. This means that, depending on the lattice geometry, irregular internal strain states could potentially be induced. See Section 7.1 for discussion on internal strain states.

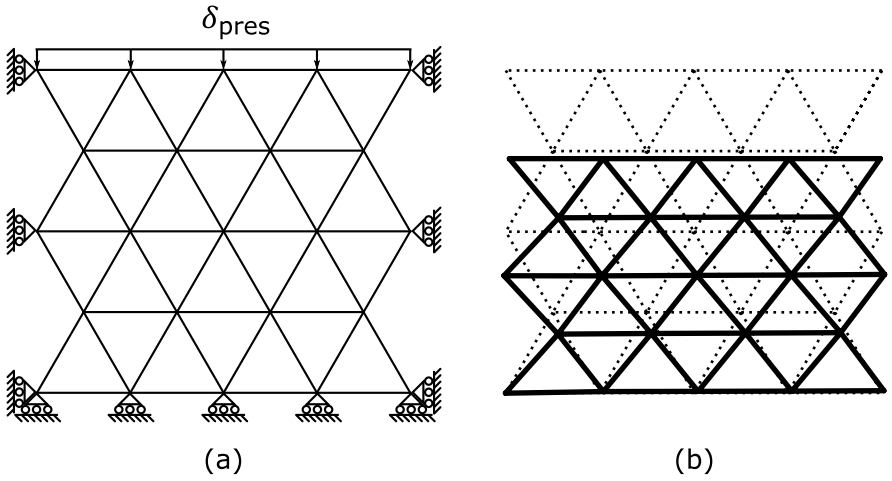

Figure 3.10: (a) Fully constrained compression type (b) with example deformation solved in LS-DYNA.

3.4.2 Shear Constraint

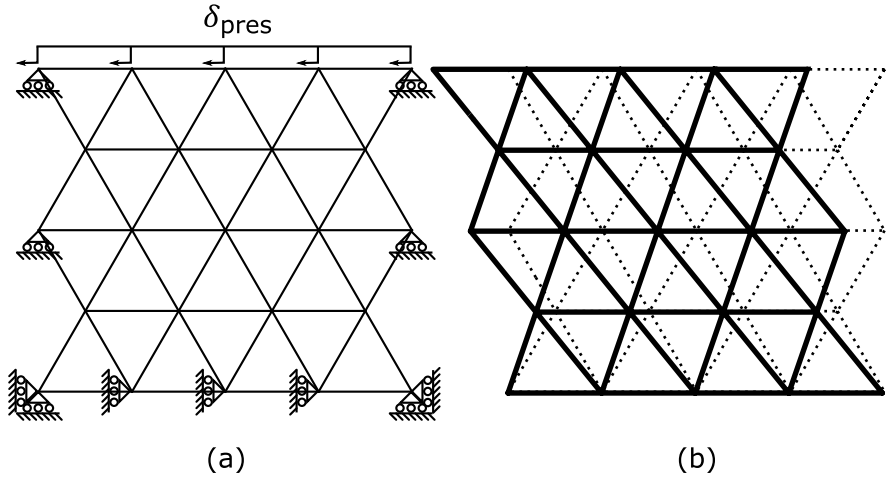

Figure 3.11: (a) Shear constraint type (b) with example deformation solved in LS-DYNA.

The lattice was loaded in shear with the boundary conditions shown in Figure 3.11. By only allowing deformation on the faces along the normals (i.e in 2D, bottom face has zero prescribed displacement in the e_1 direction), the lattice is put into macroscopic simple shear. This ensures that the calculation of the effective shear modulus is only capturing shear deformation.

By defining the boundaries as such the reaction forces act as surface tractions. In Figure 3.11, the bottom and top surfaces have only a horizontal reaction force (in opposite directions), the left and right surfaces have only vertical reaction forces which are opposing the moment caused by the top and bottom surfaces.

3.5 Effective Property Calculations

This section outlines the manner in which the macroscopic or effective mechanical properties of the lattice structures are determined. The lattices were loaded using a prescribed displacement, which enforces a constant strain. The force on each boundary is the summation of all the resulting nodal forces on each boundary. Using the total boundary force and prescribed deflection, the effective properties are calculated treating the lattice as a solid material with a linear elastic material.

For each rotation the structural response is calculated with the prescribed displacement in the local e_2' direction. The structural response of the lattice at any orientation can be inferred from the result corresponding to the orientation which aligns the direction of interest with the e_2' direction. For example, Figure 3.12(c) shows the E_x can be inferred from the 90 degree rotation, as e_1 aligns with e_2'.

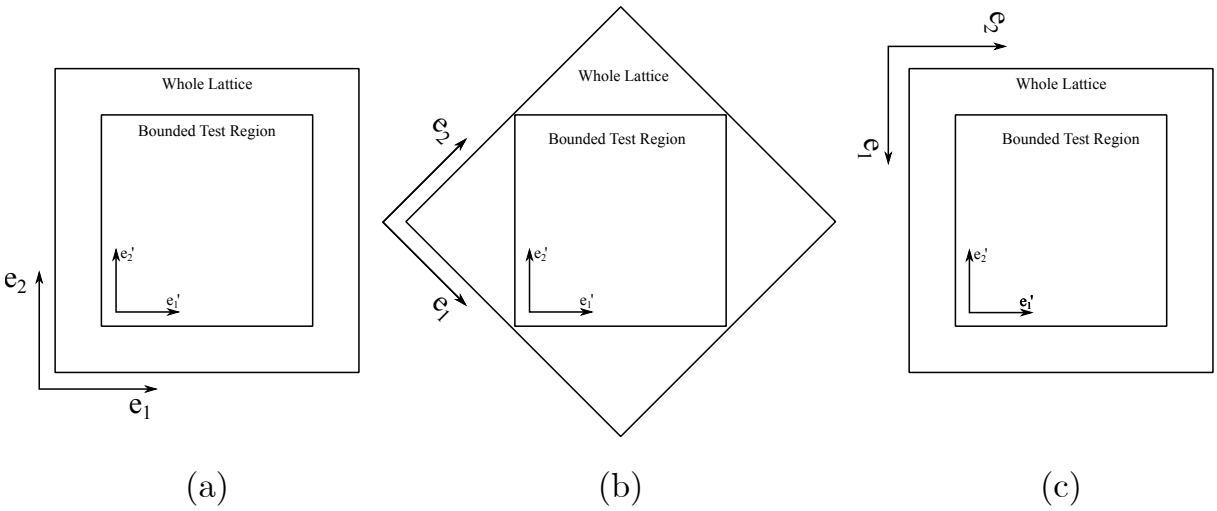

Figure 3.12: Example showing a lattice tested at varying orientations: (a) 0 degrees (b) 45 degrees (c) 90 degrees.

A distinction must be made between effective properties, used in homogenisation and continuum modelling (see Chapter 4), and structural response. The strain states need to be correct such that reasonable effective properties are inferred. That is not to say the results are not valid for orientations and constraints that do not capture the effective properties; the structural response is still found as the modelling method directly simulates the structure.

For anisotropic lattice structures, such as cubic lattices, orientation effects the validity of the effective properties for usage in continuum modelling. This is due to complex strain states being induced by the geometry (see Section 7.1). Constraints can also artificially stiffen the structural response, as is the case with fully constrained compression tests.

3.5.1 Boundary Definition

Macroscopic stress and strain states are required for calculation of effective properties. To correctly define the stress and strain states of the lattice, the projected area is required. Thus the dimensions of the boundary have to be clearly defined.

Figure 3.13 shows two possible boundary definitions for an example lattice. The first attempt was to use the smallest boundary which can fully encapsulate the lattice (fitted boundary), however it produced spurious results being sensitive to orientation. Using the average position of the boundary nodes to define the lattice boundary was found to produce more consistent results. The variance of numerically calculated effective stiffness for a 2D triangular mesh (isotropic) are 1.25×10^{-5} and 1.68×10^{-6} for fitted and average boundary definitions respectively.

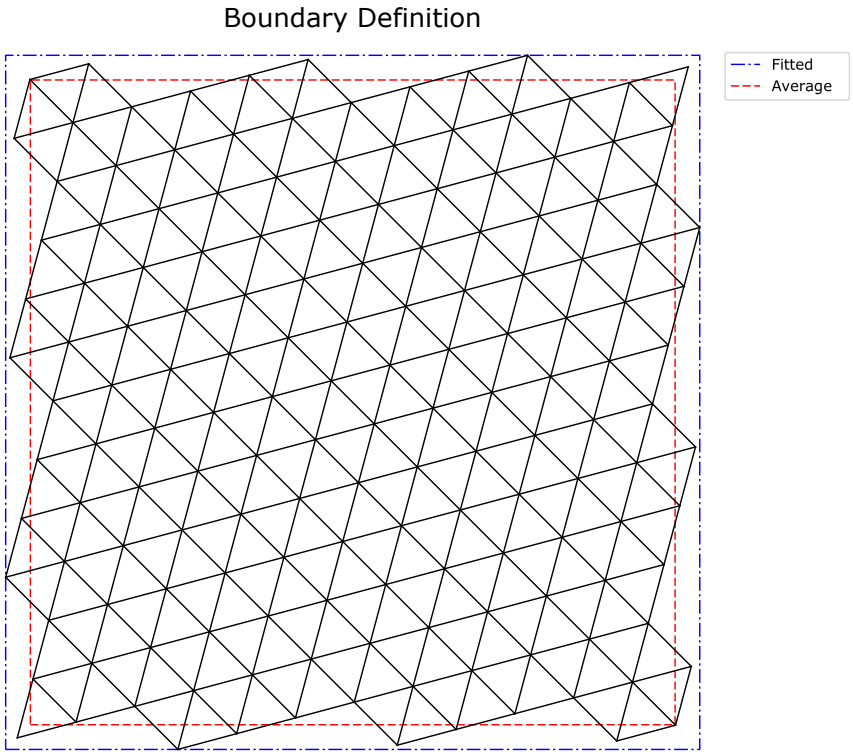

Figure 3.13: Example lattice showing two potential boundary definitions.

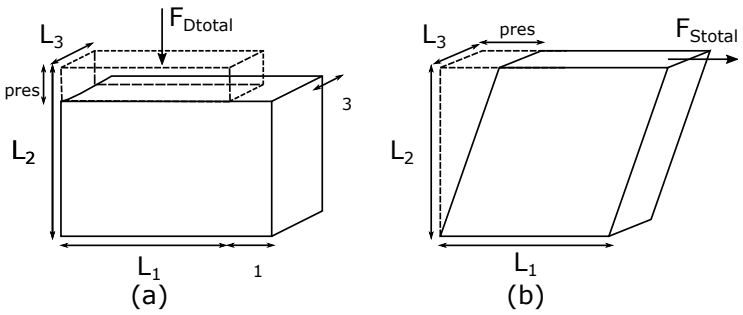

Figure 3.14: Loading conditions for the calculation of the effective properties. (a) Uniaxial compression (b) Simple shear.

3.5.2 Effective Young's Modulus

Effective Young's Modulus is calculated using compressive loading conditions (see Figure 3.14a) as follows. The effective strain is defined as:

$$\epsilon = \frac{\delta_{pres}}{L_2}, \tag{3.11}$$

where ϵ is the effective strain, δ_{pres} is the prescribed displacement and L_2 is the original length in the direction of the prescribed displacement. The effective stress is defined as:

$$\sigma_{avg} = \frac{F_{Dtotal}}{A_{proj}}, \tag{3.12}$$

where σ_{avg} is the volume averaged stress, F_{total} is the summation of all the nodal forces on the surface with the prescribed displacement and A_{proj} is the projected area of the lattice.

The projected area has to be defined for 2D and 3D respectively:

For 2D, in accordance with theory as the 2D models do not have an L_3 dimension, the beam diameter is used [6]:

$$A_{proj} = L_1 d_{beam} \tag{3.13}$$

For 3D:

$$A_{proj} = L_1 L_3 \tag{3.14}$$

The effective elastic modulus is defined from the definitions of effective stress and strain (Equations 3.11,3.12) and Hookes law as:

$$E_{eff} = \frac{\sigma_{avg}}{\epsilon} = \frac{F_{Dtotal} L_2}{A_{proj} \delta_{pres}}, \tag{3.15}$$

where E_{eff} is the effective elastic modulus of the lattice.

3.5.3 Effective Shear Modulus

Effective shear modulus is calculated using a transverse shear loading condition. The top surface is prescribed a displacement (see Figure 3.14b), as follows. The shear strain is defined as:

$$\gamma = \frac{\delta_{pres}}{L_2}, \tag{3.16}$$

where γ is the effective shear strain, δ_{pres} is the prescribed displacement and L_2 is the original length in the direction perpendicular to the shearing displacement.

The effective shear stress is defined as:

$$\tau_{avg} = \frac{F_{Stotal}}{A_{proj}}, \tag{3.17}$$

where τ_{avg} is the volume averaged shear stress, F_{total} is the summation of all the nodal forces in the direction of loading on the loaded surface, A_{proj} is the projected area as calculated using Equation 3.13,3.14.

The effective shear modulus is defined as using the effective shear stress and strain:

$$G_{eff} = \frac{\tau_{avg}}{\gamma} = \frac{F_{Stotal} L_2}{A_{proj} \delta_{pres}}, \tag{3.18}$$

where G_{eff} is the effective shear modulus.

3.5.4 Effective Poisson's Ratio

The effective Poisson's ratio is calculated using unconstrained boundary conditions under compressive loading conditions with a prescribed displacement. The transverse strains are calculated using the average deflection of the respective boundary. Where, if the e_2 direction is, the loaded direction the strains are defined as:

$$\epsilon_2 = \frac{\delta_{pres}}{L_2}, \epsilon_1 = \frac{\delta_1}{L_1}, \epsilon_3 = \frac{\delta_3}{L_3}, \tag{3.19}$$

where $\epsilon_{1,2,3}$ are the strains in the e_1, e_2, e_3 directions, δ_{press} is the prescribed displacement, δ_1 and δ_3 are the average displacement of the surfaces with e_1 and e_3 normals and $L_{1,2,3}$ are the original lengths of the lattice.

Poisson's ratio is then defined as:

$$\nu_{12} = -\frac{\epsilon_1}{\epsilon_2}, \nu_{23} = -\frac{\epsilon_2}{\epsilon_3}. \tag{3.20}$$

This loading direction was demonstrative and the calculation can be done with loading in any direction to find the Poisson's ratio in all directions.

Chapter 4

Continuum Modelling Methodology

4.1 Overview

Continuum modelling requires substantially fewer elements than discrete modelling, and can be used to generate much higher resolution views of mechanical anisotropy as the computational load is lower.

The elastic macroscopic behaviour of lattices was modelled as a continuum by representing the lattice as a regular linear elastic solid. The macroscopic properties (Young's modulus, shear modulus and Poisson's ratio) are determined by modelling the structure directly (see Chapter 3) and used in an elasticity tensor. The properties are determined using the discrete modelling approach shown in Chapter 3 using a single orientation.

The anisotropy is modelled by transforming the elasticity tensor to arbitrary orientations. This is in contrast to the discrete modelling method where the actual structure of the lattice is rotated. The transformed elasticity tensors are used with isoparametric bilinear quadrilateral elements and isoparametric trilinear hexahedron elements in 2D and 3D respectively.

The continuum modelling approach is inherently an abstraction from the physical deformation of the lattice and as such is compared to the discrete model where the structure is directly modelled to ensure that the full range of mechanical behaviours are accurately reproduced with a lower computational load.

4.2 Determining Elasticity Tensor

The lattices are treated as an orthotropic material to account for the possibility of differing properties in the principal directions. This simplifies the 36 coefficients in the compliance tensor to 9 (see Equation 4.1). The compliance tensor is defined as the inverse of the elasticity tensor.

$$S = \begin{bmatrix} \frac{1}{E_1} & -\frac{\nu_{21}}{E_2} & -\frac{\nu_{31}}{E_3} & 0 & 0 & 0 \\ -\frac{\nu_{12}}{E_1} & \frac{1}{E_2} & -\frac{\nu_{32}}{E_3} & 0 & 0 & 0 \\ -\frac{\nu_{13}}{E_1} & -\frac{\nu_{23}}{E_2} & \frac{1}{E_3} & 0 & 0 & 0 \\ 0 & 0 & 0 & \frac{1}{G_{23}} & 0 & 0 \\ 0 & 0 & 0 & 0 & \frac{1}{G_{13}} & 0 \\ 0 & 0 & 0 & 0 & 0 & \frac{1}{G_{12}} \end{bmatrix} \tag{4.1}$$

The 12 coefficients are calculated using 6 loading conditions; compression along each of the axes and 3 shear loading conditions. The coefficients are calculated as described in Section 3.5 without rotating the geometry.

As an orthotropic compliance tensor is assumed; it is important to ensure the orientation of the lattices do not induce irregular strain states. This is achievable with the lattices investigated given the geometric symmetries. If irregular lattices are investigated, a method of estimating the entire strain state would be required such that the whole elasticity tensor can be estimated. See Figure 4.1 for an example of irregular strain induced by orientation of lattice.

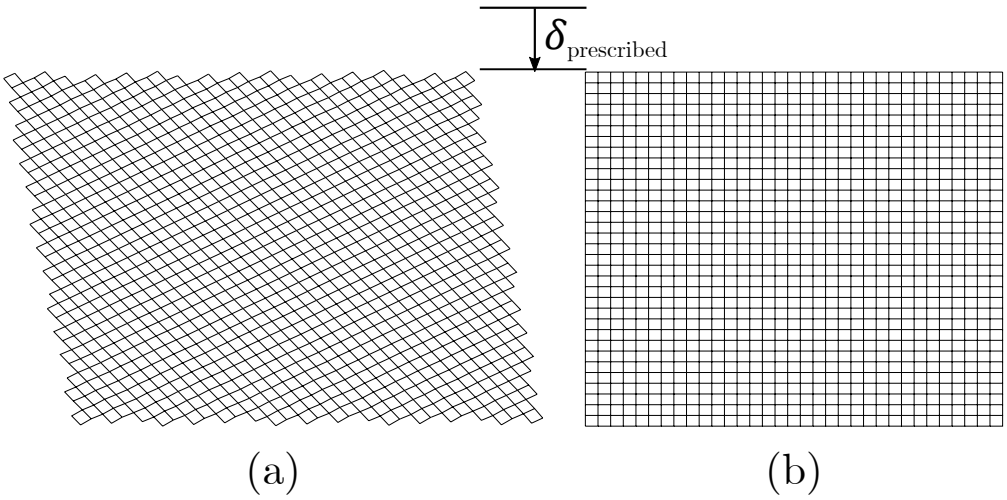

Figure 4.1: Square lattice under uniaxial compression (×50 displacement factor) showing two orientations: (a) 30° with induced shear strain (b) 0° degrees with no shear strains.

4.3 Transforming the Elasticity Tensor

The stress and strain tensors are 2nd order field tensors as they both require two directions to be specified. Stress is defined by the force direction and normal of the face the force acts upon and the strain is defined by a change of length in a given direction and the original reference direction. This implies that the elasticity tensor is 4th order. Due to symmetries inherent in the tensors, Voigt notation is a commonly used reduced order representation such that standard matrix-vector multiplication can be used. Using Voigt notation the stress and strain are 6×1 vectors and the elasticity tensor is 6×6, see Equation 4.2.

$$\sigma = \begin{bmatrix} \sigma_{xx} \\ \sigma_{yy} \\ \sigma_{zz} \\ \tau_{yz} \\ \tau_{xz} \\ \tau_{xy} \end{bmatrix}, \epsilon = \begin{bmatrix} \epsilon_{xx} \\ \epsilon_{yy} \\ \epsilon_{zz} \\ \gamma_{yz} \\ \gamma_{xz} \\ \gamma_{xy} \end{bmatrix}, E = \begin{bmatrix} E_{11} & E_{12} & E_{13} & E_{14} & E_{15} & E_{16} \\ E_{21} & E_{22} & E_{23} & E_{24} & E_{25} & E_{26} \\ E_{31} & E_{32} & E_{33} & E_{34} & E_{35} & E_{36} \\ E_{41} & E_{42} & E_{43} & E_{44} & E_{45} & E_{46} \\ E_{51} & E_{52} & E_{53} & E_{54} & E_{55} & E_{56} \\ E_{61} & E_{62} & E_{63} & E_{64} & E_{65} & E_{66} \end{bmatrix} \tag{4.2}$$

The elasticity tensor rotated by transforming both the stress and strain states to another orthogonal set of axis. The transformation matrices are assembled from the same Euler angle rotation matrices used in Chapter 3; given a 3 3 rotation matrix R, the transformation matrix A is defined as follows [64]:

$$A = \begin{bmatrix} (R_{11})^2 & (R_{12})^2 & (R_{13})^2 & 2R_{12}R_{13} & 2R_{13}R_{11} & 2R_{11}R_{12} \\ (R_{21})^2 & (R_{22})^2 & (R_{23})^2 & 2R_{22}R_{23} & 2R_{23}R_{21} & 2R_{21}R_{22} \\ (R_{31})^2 & (R_{32})^2 & (R_{33})^2 & 2R_{32}R_{33} & 2R_{33}R_{31} & 2R_{31}R_{32} \\ R_{21}R_{31} & R_{22}R_{32} & R_{23}R_{33} & R_{22}R_{33} + R_{23}R_{32} & R_{21}R_{33} + R_{23}R_{31} & R_{22}R_{31} + R_{21}R_{32} \\ R_{31}R_{11} & R_{32}R_{12} & R_{33}R_{13} & R_{12}R_{33} + R_{13}R_{32} & R_{13}R_{31} + R_{11}R_{33} & R_{11}R_{32} + R_{12}R_{31} \\ R_{11}R_{21} & R_{12}R_{22} & R_{13}R_{23} & R_{12}R_{23} + R_{13}R_{22} & R_{13}R_{21} + R_{11}R_{23} & R_{11}R_{22} + R_{12}R_{21} \end{bmatrix} \tag{4.3}$$

This transforms from old to new (primed) coordinate systems as follows [64]:

$$\begin{aligned} \sigma &= A^{-1}\sigma' \\ \epsilon &= A^{T}\epsilon' \end{aligned} \tag{4.4}$$

The transformation of elasticity can be obtained using the transformation in Equation 4.4 and Hooke's Law. Writing the stress-strain relation in the new (primed) coordinate system, and substituting Equation 4.4:

$$\begin{aligned} \sigma &= E\epsilon \\ A^{-1}\sigma' &= E(A^{T}\epsilon') \\ \sigma' &= (AEA^{T})\epsilon' \end{aligned} \tag{4.5}$$

Equation 4.5 shows that the elasticity matrix in a rotated coordinate system is $E' = (AEA^T)$.

The transformation matrix is defined by Newnham [64] for 3D elasticity, and needs to be modified to model 2D lattices. An assumption regarding the out of plane behaviour is required to simplify the elasticity tensor from 3D to 2D. Either plane stress or plane strain must be chosen; intuitively the 2D lattices are in a plane stress state as the lattice beams are free to deform out of plane.

The ability to choose plane strain or plain stress was included in the 2D continuum. Plane stress elasticity matrix is assembled from the transformed compliance tensor (inverse of E') and the plane strain elasticity matrix is assembled from the transformed elasticity tensor E', shown in Equation 4.6.

$$E_{planestress} = \begin{bmatrix} S'_{11} & S'_{12} & S'_{16} \\ S'_{21} & S'_{22} & S'_{26} \\ S'_{61} & S'_{62} & S'_{66} \end{bmatrix}^{-1}, E_{planestrain} = \begin{bmatrix} E'_{11} & E'_{12} & E'_{16} \\ E'_{21} & E'_{22} & E'_{26} \\ E'_{61} & E'_{62} & E'_{66} \end{bmatrix} \tag{4.6}$$

4.4 Finite Element Modelling

The anisotropy is investigated by using the rotated elasticity matrix in a linear elastic finite element model with the same loading conditions as used in Chapter 3. The finite element model is solved using a static implicit solver written in MATLAB. Continuum element meshes are generated in 2D and 3D to investigate effects of mesh resolution on global response.

The overview of the continuum modelling algorithm can be seen in Algorithm 3. The stiffness matrix is calculated once per angle in the series using the transformed elasticity tensor. Multiple boundary conditions are applied such that multiple loading conditions can be investigated without having to unnecessarily recalculate the stiffness matrix.

Algorithm 3 Continuum Modelling

```
procedure ContinuumModelling(Elasticity, meshResolution, angleResolution, boundaryConditions)
    mesh = generateMesh(meshResolution)
    angleSeries = generateAngleSeries(angleResolution)
    for angle in angleSeries do
        transformedElasticity = transformE(Elasticity,angle)
        K = generateStiffness(mesh, transformedElasticity)
        [Dlist, Flist] = applyBCandSolve(K,boundaryConditions)
        results = processOutput(Dlist,Flist)
    plotOutput(results)
```

The continuum results are compared to the discrete modelling method using two approaches; the macroscopic behaviour is calculated for the continuum modelling and directly compared and the displacement fields are visually compared (see Figure 4.2) to ensure continuum model is capturing the internal response (see Chapter 4).

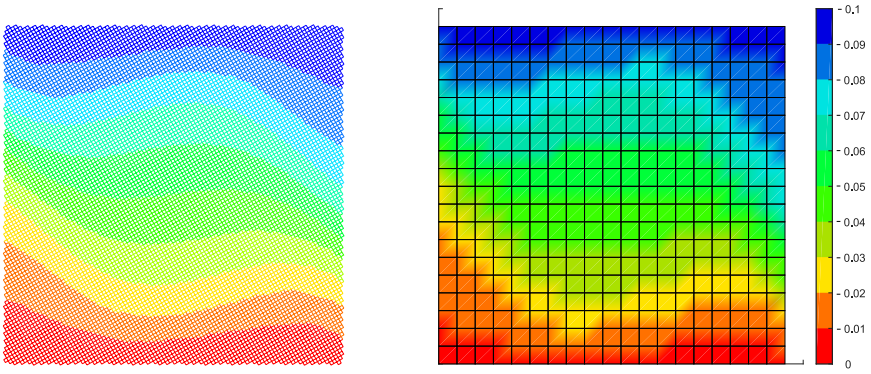

(a) (b)

Figure 4.2: Comparison between y-displacement field of discrete stiffness modelling and continuum modelling of square lattices at 30°: (a) Discrete modelling (b) Continuum model (19×19 bilinear quadrilateral elements).

Chapter 5

Microstructural Indices Methodology

5.1 Overview

The mean intercept length (MIL), and its associated fitted ellipsiod is calculated using BoneJ [16]. BoneJ is an open source plug-in for ImageJ, developed to analyse computed tomography (CT) and X-ray microtomographic (μCT) images of bone samples [16].

Using pre-existing software to generate the MIL and fitted ellipsoid, in lieu of writing code to calculate the microstructural indices, means the MIL does not require validation. A secondary benefit of using BoneJ is it creates the potential for using the current mesh generation and mechanical modelling framework to investigate other microstructural indices. For example branch length and junction count, connectivity density, structural model index (SMI), trabecular thickness (Tb.Th) and spacing (Tb.Sp) and volume fraction (BV/TV) are all indices available in BoneJ [16].

The software was developed for the analysis of CT and μCT images, which are conventionally represented as a sequence of images representing slices through the sample (commonly referred to as an image stack). Thus the lattices need to be represented as an image stack; whereas for modelling the lattice geometry defined as a list of nodal coordinates and element connectivity (see Figure 5.1a).

The process to generate an image stack representation of the lattice has two steps; firstly a skinned 3D model representation (see Figure 5.1b) of the lattice was created, using a python library from a free and open-source 3D modelling software called Blender. The 3D skinned model is saved as a .STL and sliced to create the image stack for BoneJ. See Appendix A for list of software versions used, as open-source software is subject to change.

5.2 Solidify Lattice

The lattice is solidified using a mesh modifier in Blender called 'Skin'. Modifiers are non-destructive real-time operations that are applied to a mesh. The nodal coordinate and element connectivity definitions for the FE model are saved in a text file which are processed by a python script running in Blender's internal python module (see Algorithm 4). The nodal coordinate and element connectivity definitions are stored as Blender mesh object. The skin modifier is applied to the mesh, and the radii of the lattice trabeculae are set. A final surface subdivision modifier is applied to create the circular cross section.

The solified mesh is exported as a .STL file for further processing.

5.3 Slice Lattice

The solidified representation of the lattice is saved in an .STL as a collection of surface triangles represented as a unit normal and three vertices. The STL coordinates are unitless, contain no scale information and are all in the positive octant.

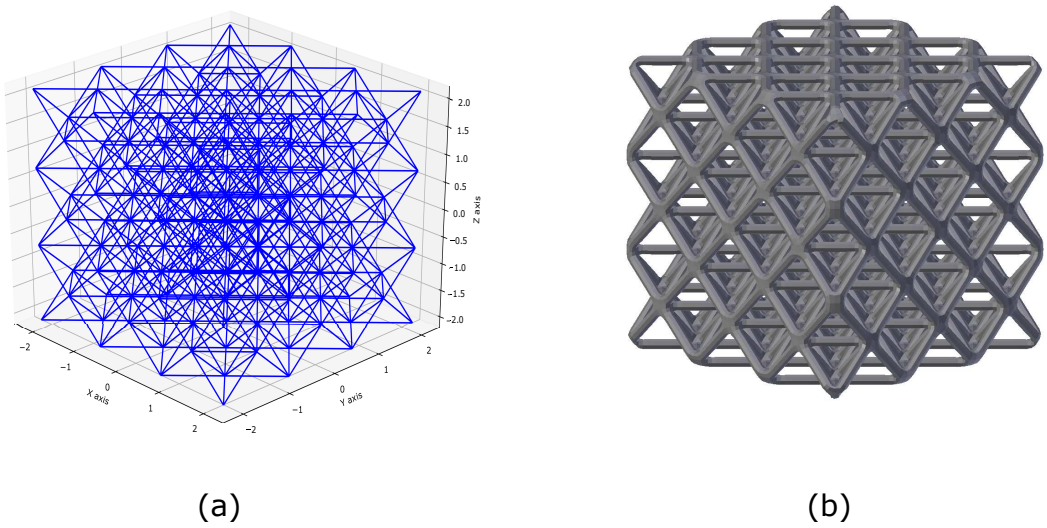

Figure 5.1: Representations of the octet-truss lattice: (a) FE model (b) skinned 3D model generated using this methodology.

Algorithm 4 Solidify Lattice

```
procedure SolidfyLattice(filename, radius)
    [nodes,elements] = processFile(filename)
    mesh = createMesh(nodes,elements)
    mesh.addModifier(type = 'SKIN')
    for vertex in mesh.skinVertices do
        vertex.radius = radius
    mesh.addModifier(type = 'SUBSURF')
```

The STL vertices need to be shifted such that the mesh is centred around the $(0, 0, 0)$ position. The STL coordinates are scaled based on the resolution, such that each pixel represents a unit cube. The slicing procedure (see Figure 5)iterates over the layers to find the lines of intersection with the layer height and surface triangles. The lines of intersection are used to create the individual images (see Figure 5.2).

Algorithm 5 Slice STL

```
procedure SliceSTL(filename, resolution)
    mesh = readSTLVertices(filename)
    [scale, shift] = calculateShiftAndScale(mesh, resolution)
    mesh.shift(shift)
    mesh.scale(scale)
    voxels = createEmptyArray(mesh,resolution)
    for layer in voxels.Layers do
        lines = findTriangleIntersections(mesh,layer)
        pixels = linesToPixels(lines, resolution)
        voxels[layer] = pixels
    outputImageStack(voxels)
```

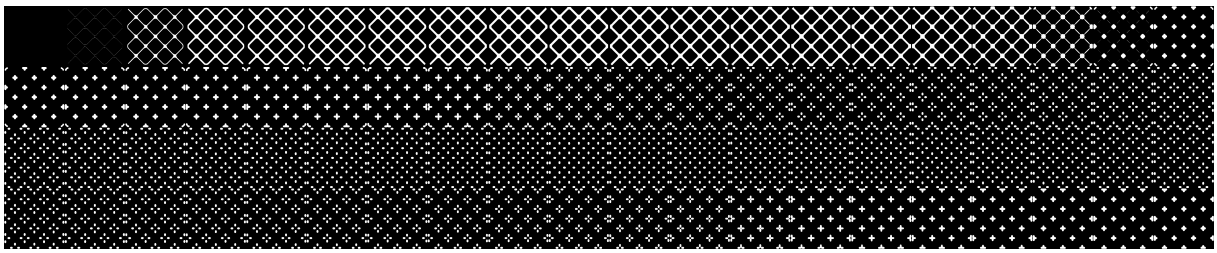

Figure 5.2: Portion of image stack generated from the octet-truss lattice.

The image stack is then imported to BoneJ for analysis. However it does need further cropping to remove the effect of the external radii (see Figure 5.3) such that the stack represents a repeatable unit. This cropping is done in two steps, firstly create a sub-stack to crop the layer axis and then use the ImageJ cropping tool to crop each image in the stack.

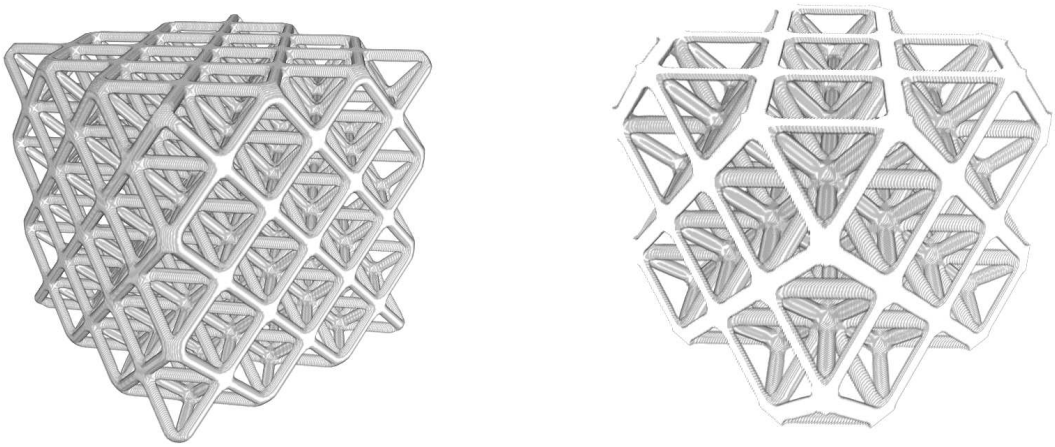

Figure 5.3: Octet-truss lattice as: (a) Loaded directly from slicing and (b) after cropping.

Once the image stack has been cropped the MIL analysis is performed. BoneJ outputs the MIL vector cloud, degree of anistropy (DA) and an anisotropy (or fabric) tensor. The MIL vector cloud (see Figure 5.4) is a visualisation of the raw data, where each point represents the mean intercept length multiplied by its associated direction vector. An ellipsoid is fitted to the MIL vector cloud to create the fabric tensor, which is the second rank tensor of eigenvectors associated with the ellipsoids axes. The degree of anisotropy (DA) is a scalar measure calculated from the maximum and minimum eigenvalues, being the length of the ellipsoids axes (see Equation 5.1). Degree of anisotropy ranges from 0 to 1, relating to isotropic and anisotropic microstructure respectively.

$$DA = 1 - \frac{\lambda_{short}}{\lambda_{long}} \tag{5.1}$$

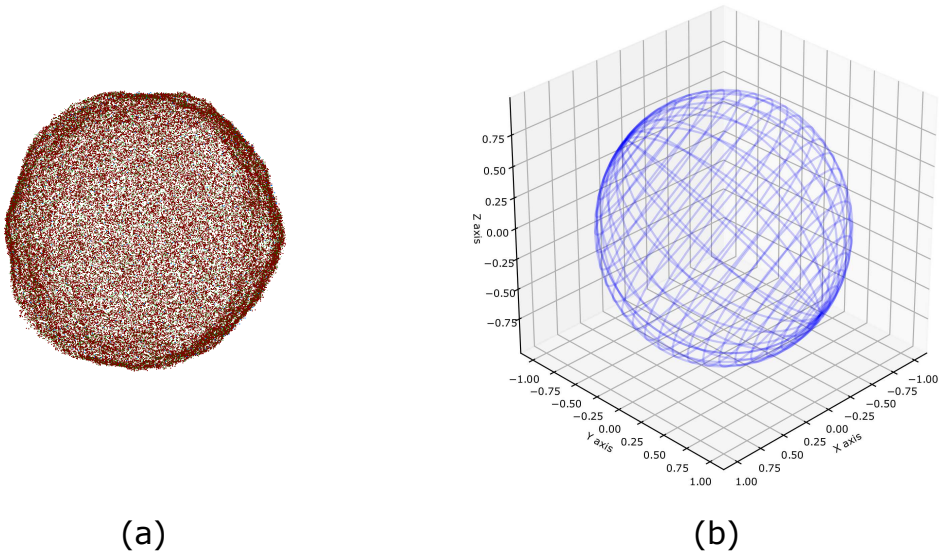

Figure 5.4: MIL Analyses: (a) vector cloud (b) fitted ellipsoid.

Chapter 6

Discrete Modelling Results

6.1 Effective Elastic Properties of 2D lattices

The following section outlines the results of the 2D discrete lattice models. The effective properties are quoted as relative to the parent material ($\frac{E_{lattice}}{E_{matl}}$); the properties are presented on polar plots to show how the properties change with angle.

6.1.1 2D Square Lattice

The relative stiffness of the square lattice along the x and y axis (0° and 90°) are analytically calculated with the number of columns in the lattice [17]:

$$E_{rel} = \frac{A_{cs}(n)}{A_T} = \frac{A_{cs}(n)}{(n-1)t}, \tag{6.1}$$

where A_{cs} is the cross sectional area of the beam, A_T is the total projected area and n is the number of columns. Table 6.1 shows the analytical solution for effective stiffness compared to the numerical value taken from Figure 6.1 for a 2D square lattice with 137 columns. The percentage difference is calculated as $e = \frac{abs(val_{analytical} - val_{numerical})}{val_{analytical}}$.

Table 6.1: Comparison of the numerical and analytical solution for the relative effective stiffness of a 2D square lattice at 0° and 90° for 18496 cells.

	Analytical	**Numerical**	**Difference (%)**
Effective Elastic Modulus	7.910×10^{-2}	7.909×10^{-2}	0.025

The analytical solution for the 2D square lattice is a function of the total lattice geometry (function of number of columns), unlike the other analytical solutions that use a unit cell approach. The bulk behaviour, or behaviour assuming infinite lattice size, is calculated by finding the asymptote of Equation 6.1. Equation 6.2 shows the result for 2D square lattice with circular cross sections.

$$E_{rel} = \frac{r\pi}{2} \tag{6.2}$$

Using Equation 6.2, the bulk 2D square relative stiffness is 7.850×10^{-2}, which equates to a percentage difference of 0.7% in the numerically determined results.

Figure 6.1 shows the effective properties of a 2D square lattice. Effective unconstrained stiffness, fully constrained stiffness and shear modulus are shown.

The fully constrained and unconstrained behaviour is exactly the same at 0° and 90°; as Poisson's ratio is zero at those angles the lateral confinement has no effect (see Figure 6.2). The largest difference is between the fully constrained and unconstrained at 45°, which is coincident with the angle where Poisson's ratio is highest ($\nu_{45} = 0.989$).

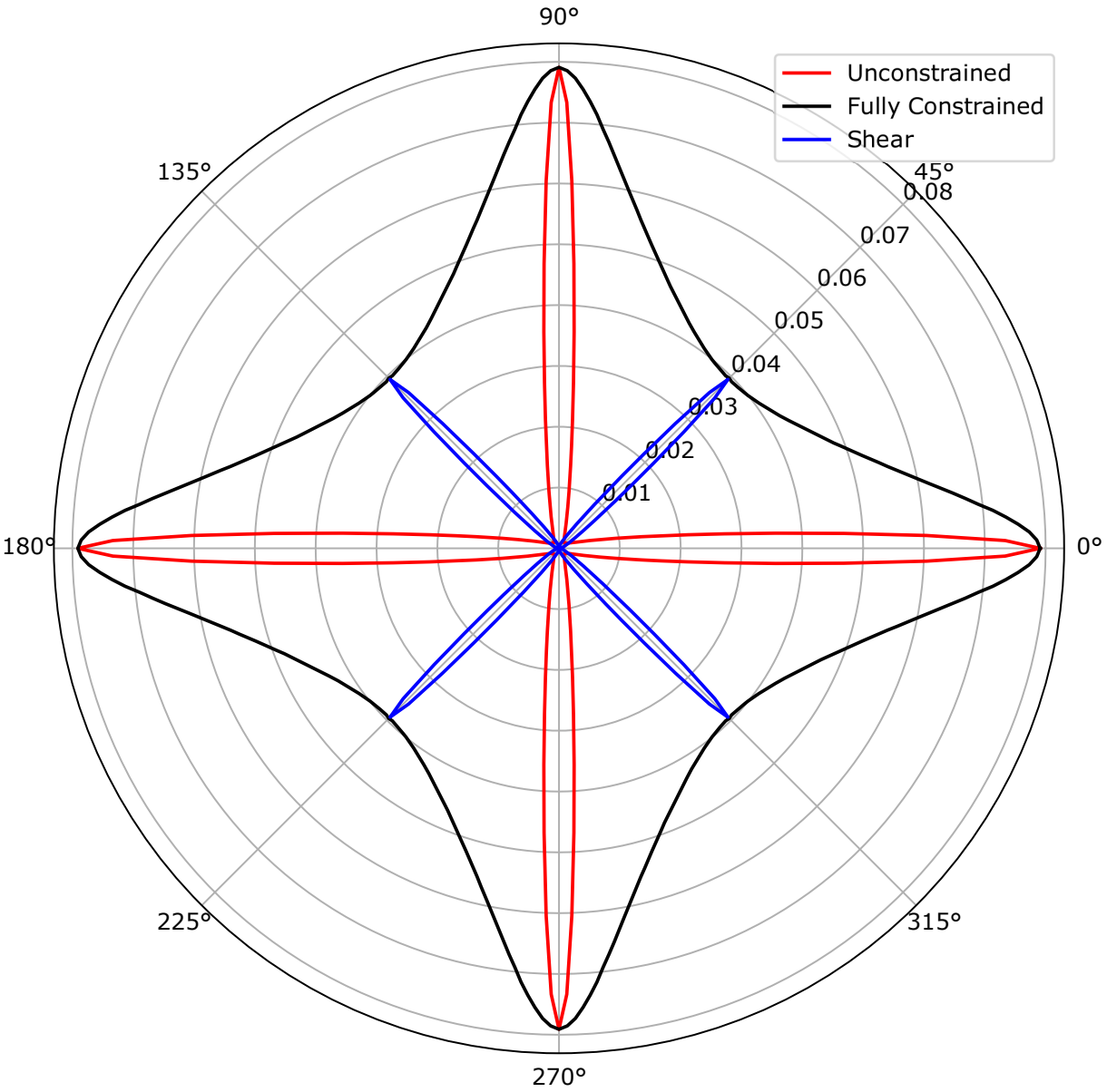

Figure 6.1: Polar plot of effective properties for 2D square lattice. Showing macroscopic stiffness with and without lateral constraint (unconstrained and fully constrained respectively) and shear modulus.

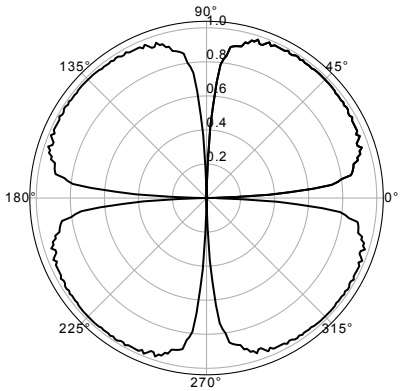

Figure 6.2: Polar plot of effective Poisson's Ratio for 2D Square lattice.

6.1.2 2D Triangular Lattice

Figure 6.3 shows the effective properties of the 2D triangular lattice. Effective unconstrained stiffness, fully constrained stiffness and shear modulus are shown.

The response is fully isotropic in both compression and shear loading. The effective properties are compared to closed form analytical solutions in Table 6.2. The table is left blank for analytical solutions that do not exist readily in literature.

Table 6.2: Effective properties of 2D triangular lattice, with comparison between numerical and analytical results.

	Numerical	**Analytical**	**Difference (%)**
Unconstrained	9.150×10^{-2}	9.096×10^{-2}	0.891
Fully Constrained	1.027×10^{-1}	1.020×10^{-1}	0.670
Shear	3.443×10^{-2}		
Poisson's Ratio	3.286×10^{-1}		

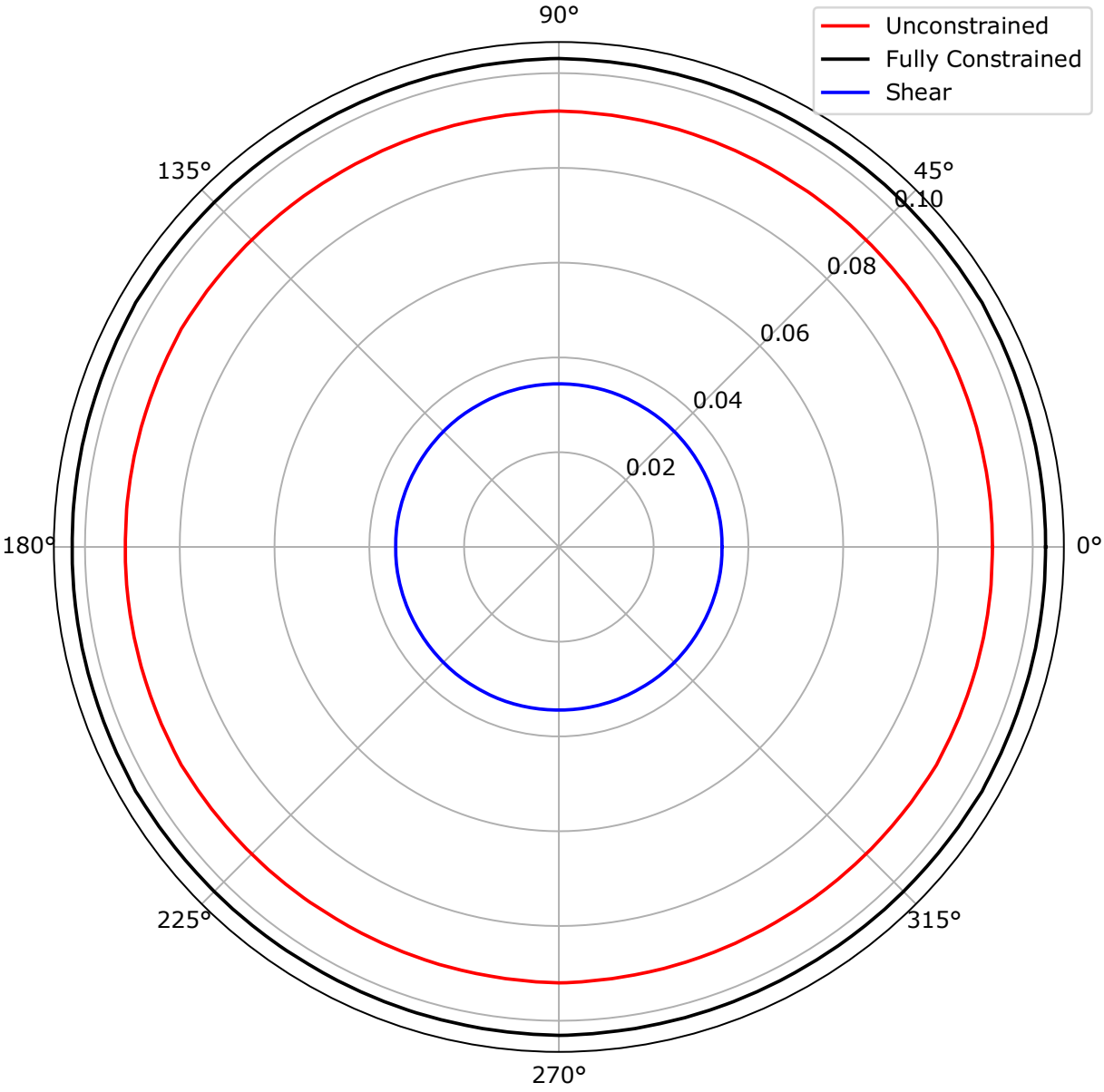

Figure 6.3: Polar plot of effective properties for 2D triangular lattice. Showing macroscopic stiffness with and without lateral constraint (unconstrained and fully constrained respectively) and shear modulus.

6.1.3 2D Hexagonal Lattice

Figure 6.4 shows the effective properties of the 2D hexagonal lattice. Effective unconstrained stiffness, fully constrained stiffness and shear modulus are shown.

Local maxima occur near 0° and 30° in the fully constrained behaviour. See annotations on Figure 6.4 to see orientation of lattice at spikes. Figure 6.5 shows the unconstrained and fully constrained effective elastic modulus with the analytical solutions on individual plots to aid readability.

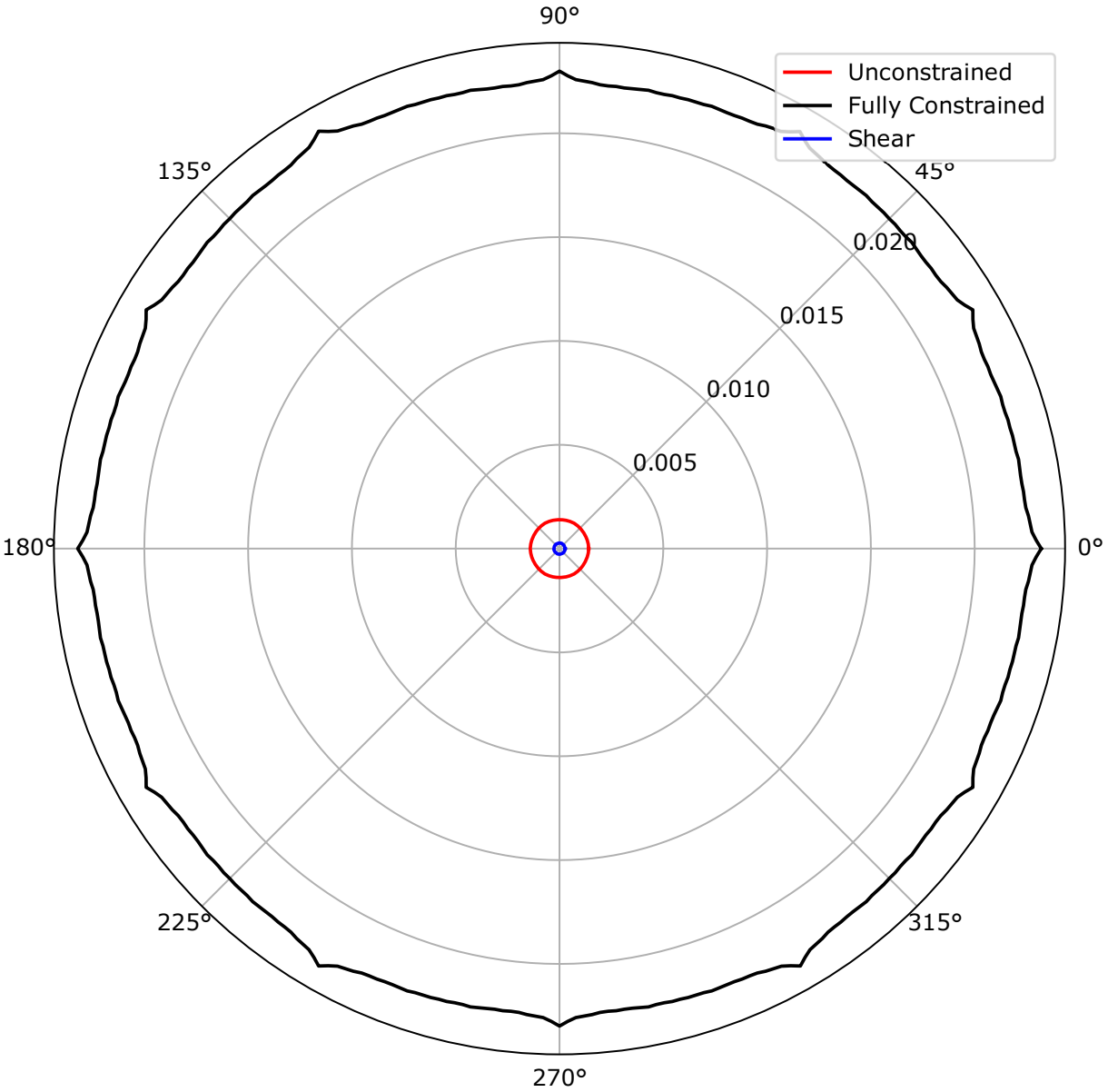

Figure 6.4: Polar plot of effective properties for 2D hexagonal lattice. Showing macroscopic stiffness with and without lateral constraint (Unconstrained and fully constrained respectively) and shear modulus.

Figure 6.5 demonstrates that the numerical response oscillates between two values from 0° to 30°. The difference between the maximum and minimum is 1.4% and 3.5% for unconstrained and fully constrained respectively. The fully constrained response oscillates between overestimating and underestimating (when compared to the analytical solution), whilst the unconstrained response constantly overestimates the analytical solution. This deviation from theoretical isotropy is likely due to boundary effects. Figure 6.6 shows the polar plot of effective mechanical properties with various element densities; this demonstrates the local behaviour diminishes as element density increases. The effect is most prominent when considering the fully constrained case.

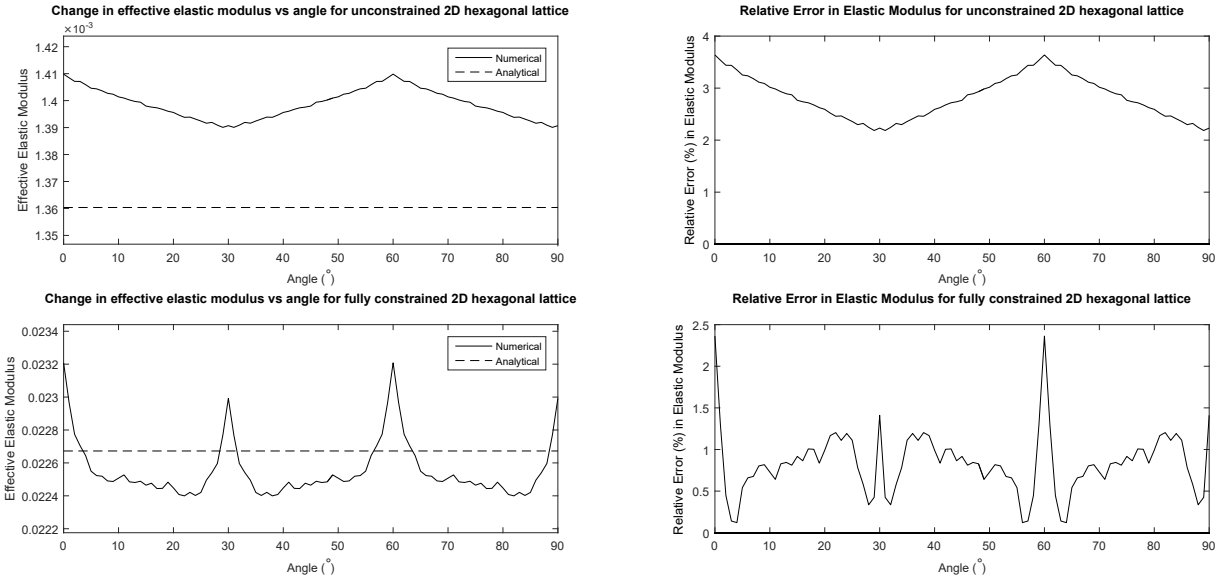

Figure 6.5: Comparison between analytical and numerical effective elastic modulus, with relative error showing how differences change with angle.

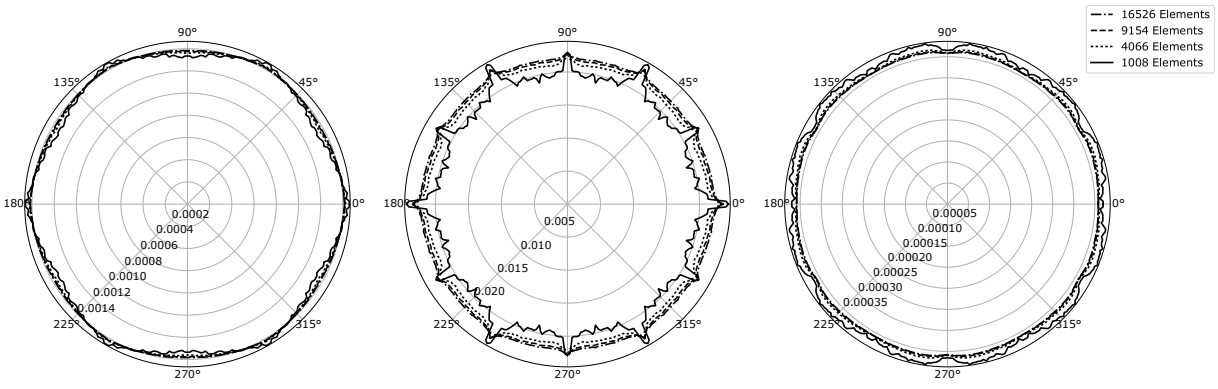

(a) (b) (c)

Figure 6.6: Polar plot of effective properties for 2D hexagonal lattice with increasing element densities. (a) Unconstrained elastic modulus (b) Fully constrained elastic modulus (c) Shear modulus.

Table 6.3 shows the numerically determined effective properties compared to the analytically calculated effective properties at 0°. The hexagonal lattice has overall larger differences when compared to square and triangular lattices. The largest discrepancy is in Poisson's ratio, with a difference of 2.64%. The analytical solutions used are derived by assuming a predominant deformation mode (bending for hexagonal lattices) and calculating the response by that alone. The discrepancy could be explained by the fact that Timoshenko beams were used in the numerical model, which accounts for axial, bending and shear deformation.

Table 6.3: Effective properties of 2D Hexagonal lattice, with comparison between numerical and analytical results at 0°.

	Numerical	**Analytical**	**Difference (%)**
Unconstrained	1.390×10^{-3}	1.360×10^{-3}	2.185
Fully Constrained	2.277×10^{-2}	2.267×10^{-2}	0.425
Shear	3.570×10^{-4}		
Poisson's Ratio	9.736×10^{-1}	1	2.639

6.1.4 Isotropic Validation via Lamé Parameter Relations

As the triangular and hexagonal lattices are isotropic, their mechanical properties calculated numerically can be validated using the Lamé parameter relations as any Lamé parameter can be calculated given 2 others. Table 6.4 shows the Lamé parameter relations of interest.

Table 6.4: Lamé parameter relations.

	$E =$	$\nu =$	$G =$
(E, G)	E	$\frac{E}{2G} - 1$	G
(E, ν)	E	ν	$\frac{E}{2(1+\nu)}$
(G, ν)	$\frac{2G(1+\nu)}{3(1-2\nu)}$	ν	G

Table 6.5 shows each mechanical property calculated via Lamé parameter relations, using the other two properties. The percentage difference is calculated between the calculated value and the numerically determined value. The percentage difference for all parameters, for both the triangular and hexagonal lattice, is under 0.1%, demonstrating that the parameters determined numerically for the triangular and hexagonal lattices do represent isotropic behaviour.

Table 6.5: Validation of effective properties using Lamé parameter relations for isotropic lattices.

	Triangular			**Hexagonal**		
	Lamé	Numerical	Difference (%)	Lamé	Numerical	Difference(%)
E	9.148×10^{-2}	9.150×10^{-2}	0.0139	1.410×10^{-3}	1.390×10^{-3}	0.0142
G	3.443×10^{-2}	3.443×10^{-2}	0.0139	3.572×10^{-4}	3.57×10^{-4}	0.0432
ν	3.287×10^{-1}	3.286×10^{-1}	0.0562	9.736×10^{-1}	9.736×10^{-1}	0.0875

6.2 2D Boundary Cropping Comparison

Figure 6.7 shows the difference in mechanical response for the two cropping methods. The element intersection cropping leads to spurious results that underpredict the effective elastic moduli and shear modulus and are not isotropic. This cropping technique causes a shift in predominant deformation mode, as demonstrated in Figure 6.8 which shows a close up of the boundary behaviour.

The different responses shown in Figure 6.8 are due to different constraints, explained in Section 3.4.

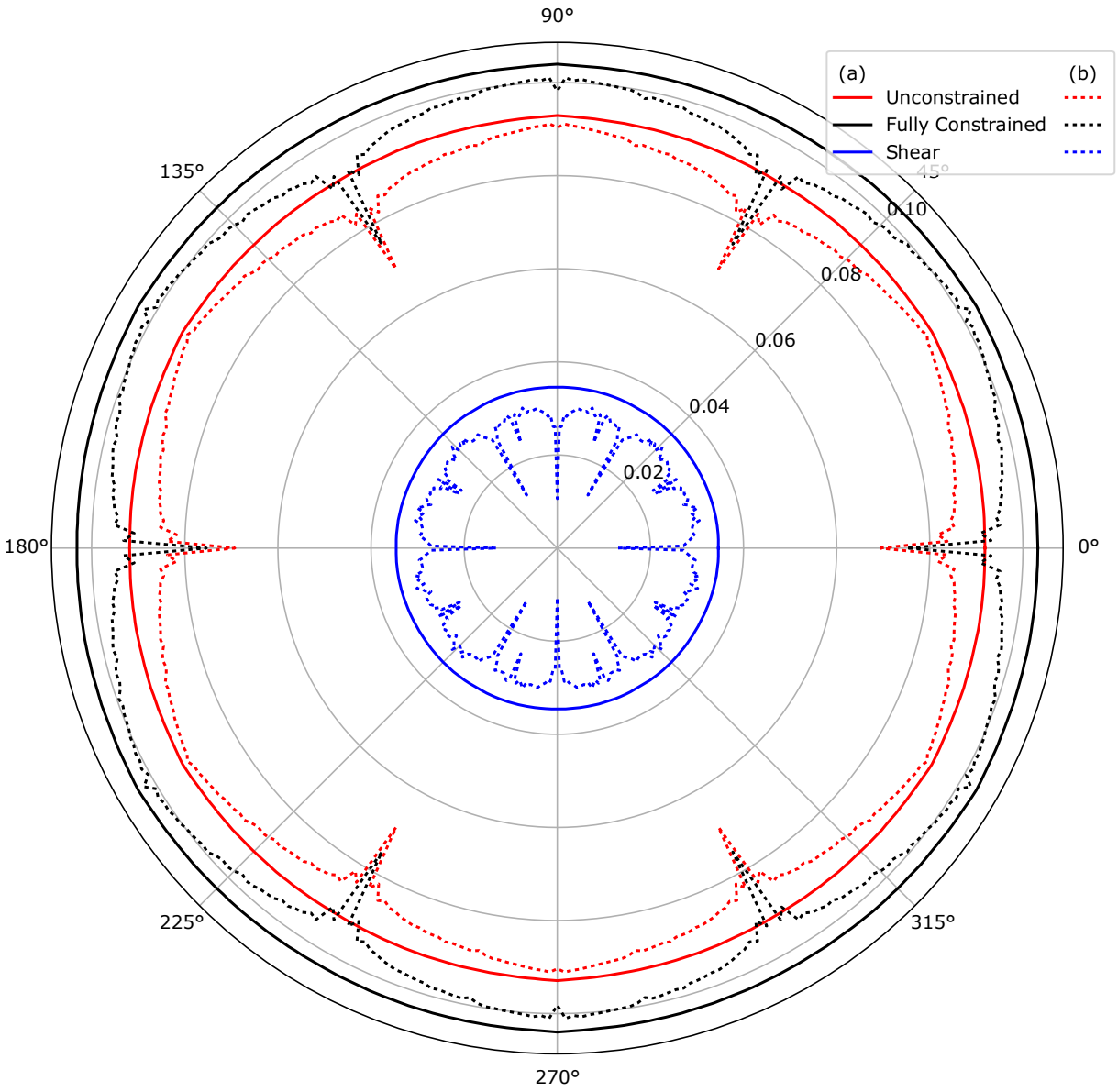

Figure 6.7: Polar plot showing the effective elastic moduli and shear modulus for using (a) whole element cropping (b) element intersection cropping .

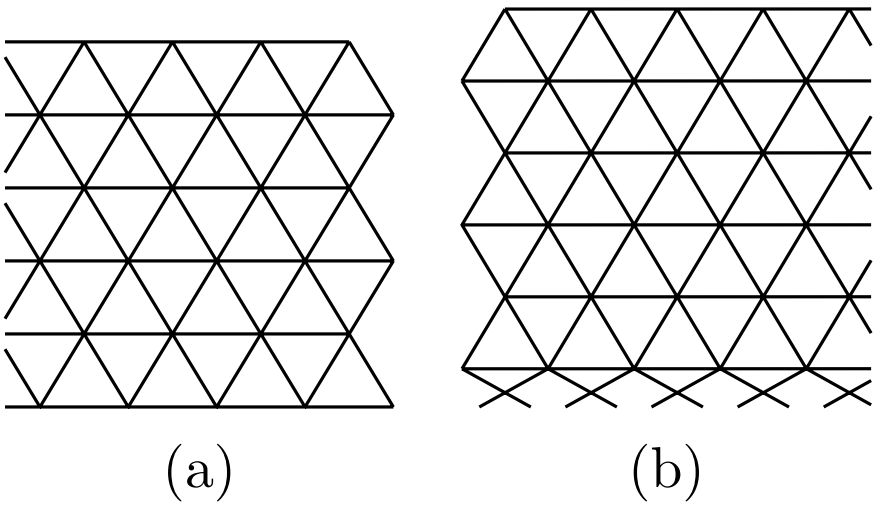

Figure 6.8: Zoomed in view of the boundary behaviour of triangular lattice for two different cropping schemes. Displacement factor of 20x is used to clearly show deformation. (a) Whole element cropping (b) element intersection cropping.

Figure 6.8b shows high levels of displacement on the bottom edge boundary, whilst the elements in Figure 6.8a don't show much displacement. The elements on the lower edge are hanging, which causes large amounts of bending deformation whereas the triangular lattice should have axial deformation as its primary deformation mode. This explains the element intersection cropping having lower predicted effective properties as beams axial stiffness is greater than its bending stiffness. Figure 6.8a shows the expected uniform displacement of all cells in the lattice.

Figure 6.9 shows the same mechanism causing spurious results in the 2D hexagonal and square lattices. The boundary elements deforming in bending with boundary nodes having high deformation relative to the lattice nodes.

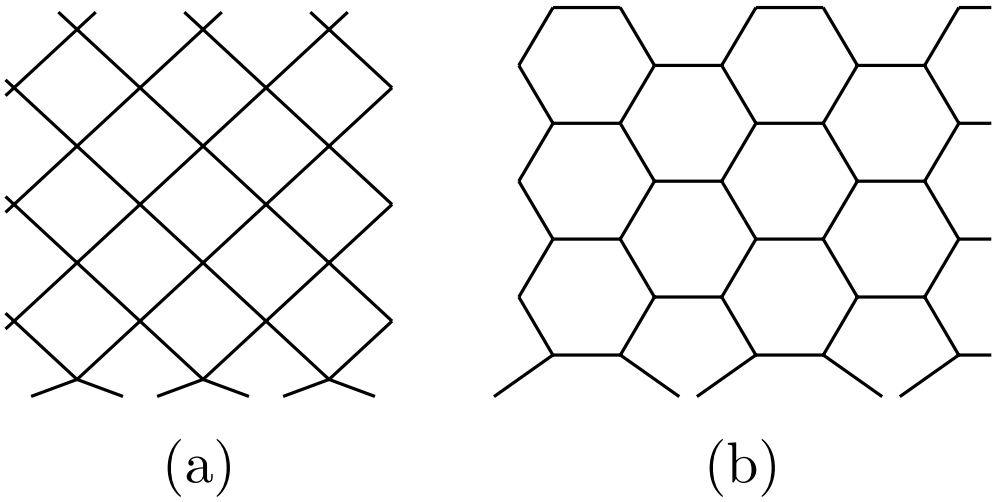

Figure 6.9: Zoomed in view of the boundary behaviour of square and hexagonal lattice for element intersection cropping. (a) Square lattice with 50x displacement factor at 45° (b) Hexagonal lattice with 20x displacement factor and 0°.

Figure 6.10 shows the polar plot for a square lattice using two different cropping schemes. The element intersection cropping leads to spurious results, however agreement is high between the two schemes near 0° and 90°. This is due to the arrangement of the lattice at those angles not inducing bending deformation as the beams are aligned with the loading direction. The difference is most prominent at 45° for shear and fully constrained cases. This is due to the boundary beams being at the largest angle at 45° and thus causing the highest bending deformation.

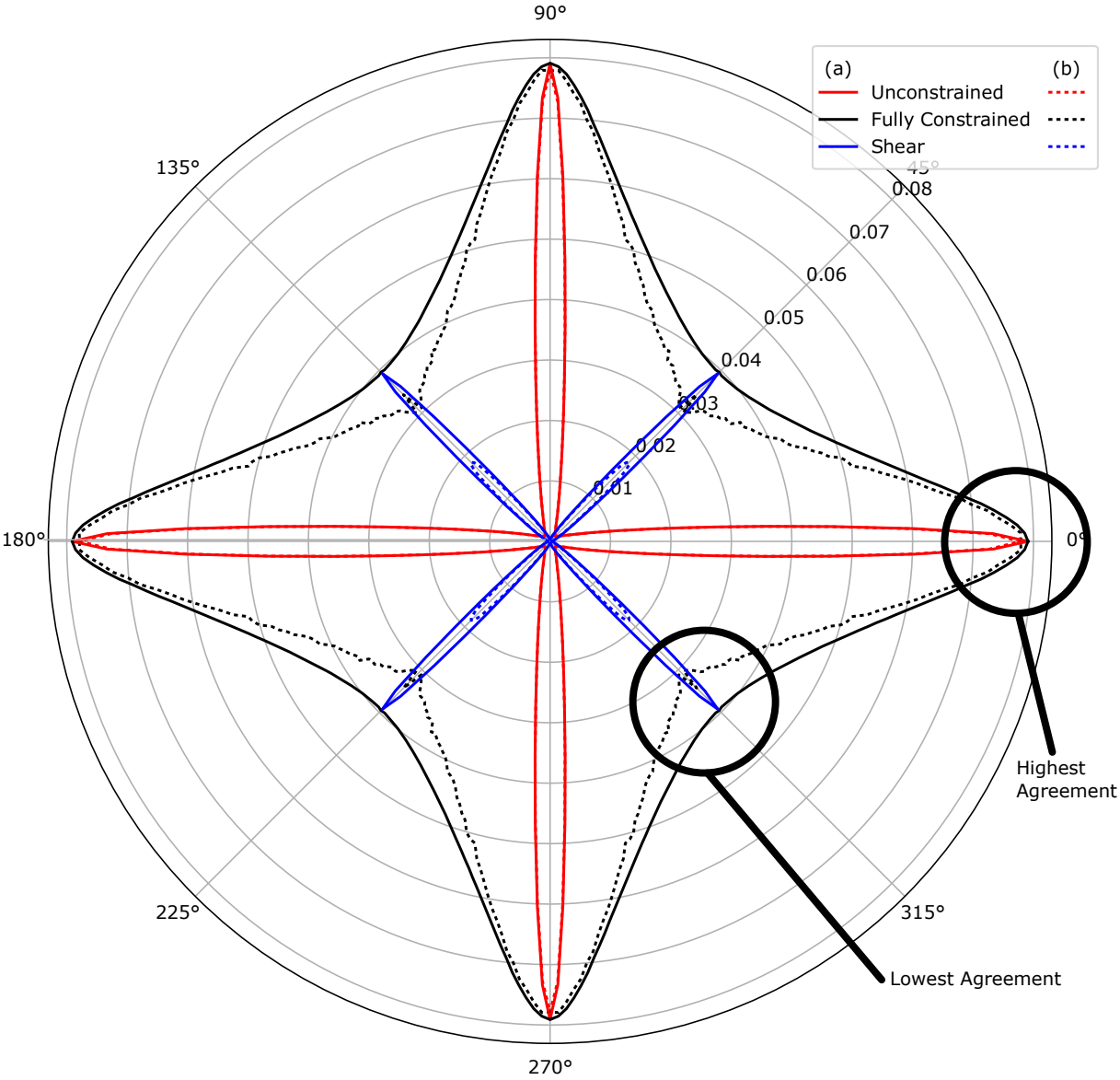

Figure 6.10: Polar plot showing the effective elastic moduli and shear modulus of the square lattice for using (a) whole element cropping (b) element intersection cropping .

Figure 6.11 shows the polar plot for a hexagonal lattice using two different cropping schemes. The element intersection cropping still causes spurious results, however the difference between element intersection cropping and whole beam cropping is more substantial in the fully constrained case. This is due to bending being the predominant deformation mode for the unconstrained case, while the fully constrained case has a higher degree of axial deformation and is therefore more sensitive to the boundary deforming in bending (see Figure 6.9 for view of deformation at the boundary for fully constrained hexagonal lattices).

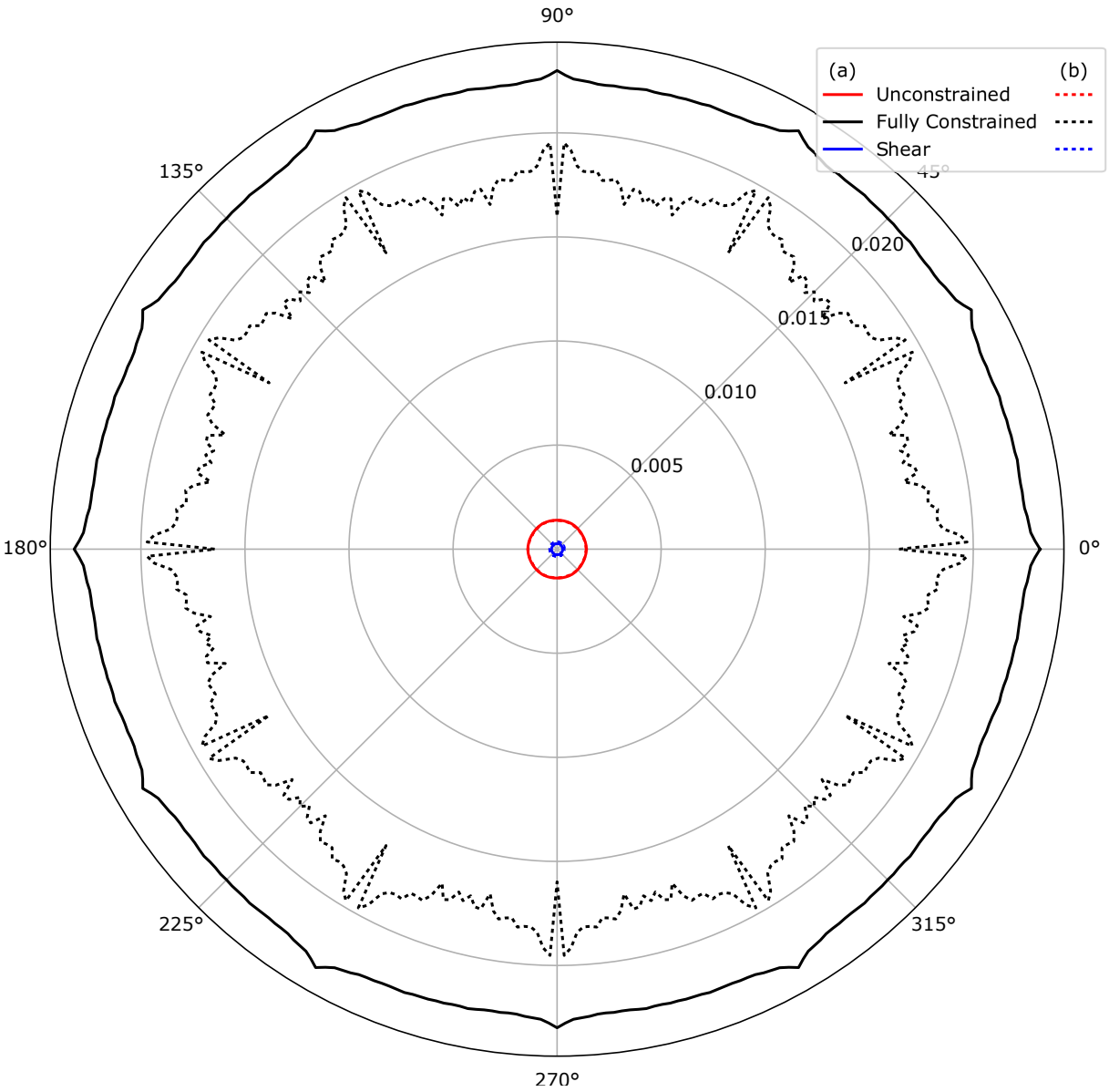

Figure 6.11: Polar plot showing the effective elastic moduli and shear modulus of the hexagonal lattice for using (a) whole element cropping (b) element intersection cropping.

The investigation of cropping schemes for the three 3D cases show that the element intersection cropping scheme leads to spurious results, however the degree of error is a function of the predominant deformation mode of the lattice. For example, the triangular lattice shows similar error when using the element intersection cropping for both unconstrained and fully constrained cases as both these boundary conditions result in a axially dominant deformation whilst the hexagonal lattice shows differing degree of error for the two compression constraints as the constraint type affects the dominant deformation mode.

The element intersection cropping method is akin to cutting out a sample from a larger specimen, and the error seen is akin to the take-up seen as the boundary collapses before the structure is loaded. As a static, small strain model is used to determine the effective elastic properties, the model does not go past the boundary collapse region.

6.3 2D Lattice Comparisons

This section shows comparisons between effective mechanical properties of the three 2D lattices investigated.

Figure 6.12 shows the effective elastic modulus in the unconstrained case for square, triangular and hexagonal lattices. The triangular lattice has the highest relative elastic modulus which is followed by the square lattice at 0° and 90°. The relative elastic modulus of the hexagonal lattice is overall the lowest, however it is greater than the square relative elastic modulus between 30° and 50°.

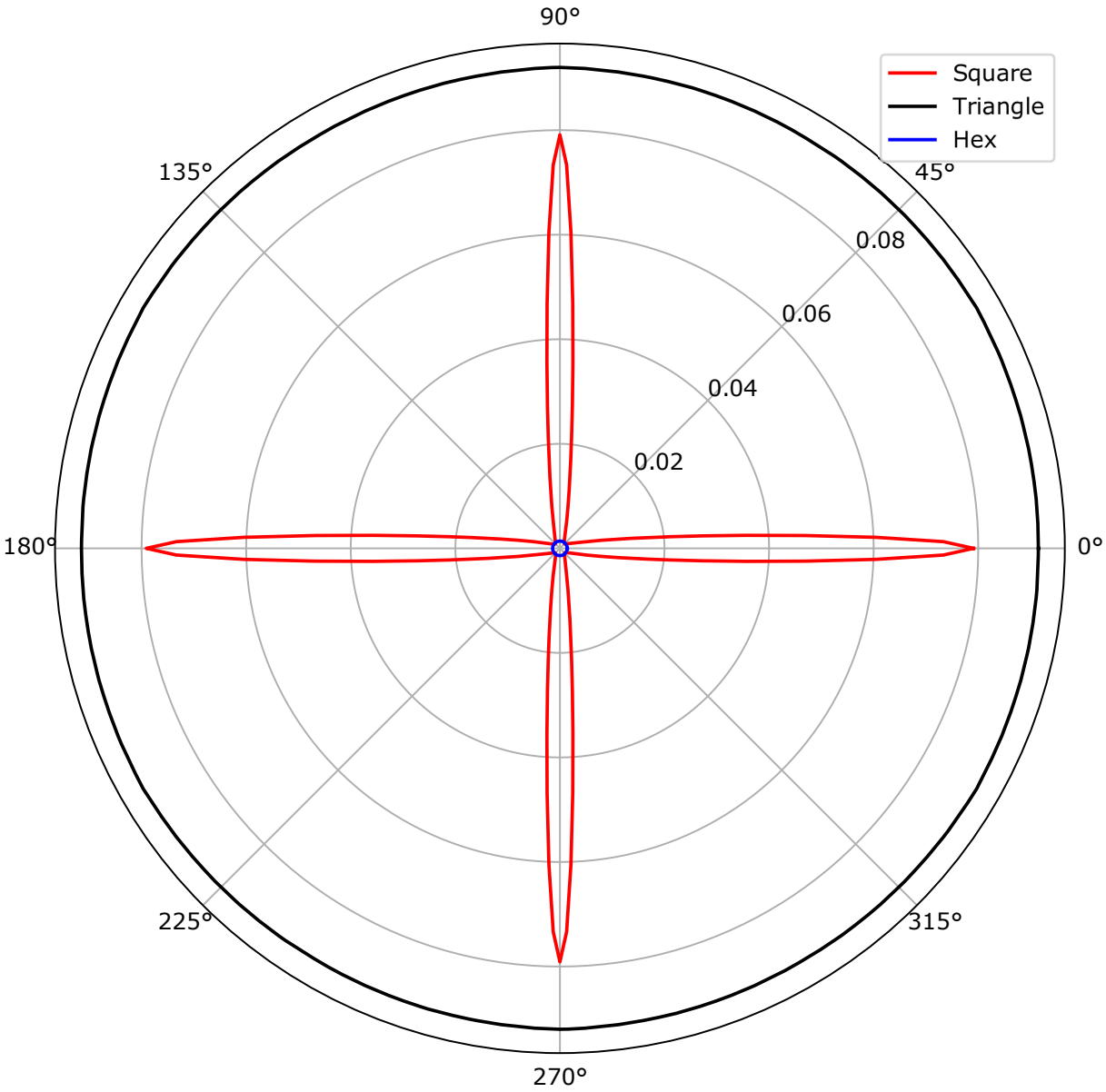

Figure 6.12: Polar plot showing the effective elastic modulus with no lateral constraint (unconstrained) for 2D square, triangular and hexagonal lattices.

Figure 6.13 shows the effective elastic modulus in the fully constrained case for square, triangular and hexagonal lattices. The effective elastic moduli can be listed in order of magnitude as there is no overlap between square and hexagonal lattices, as seen in the unconstrained case. The lattices can be easily ordered from highest to lowest effective elastic modulus as triangle, square and hexagonal. The local spiking behaviour of the hexagonal lattice is small at the scale of the other lattices.

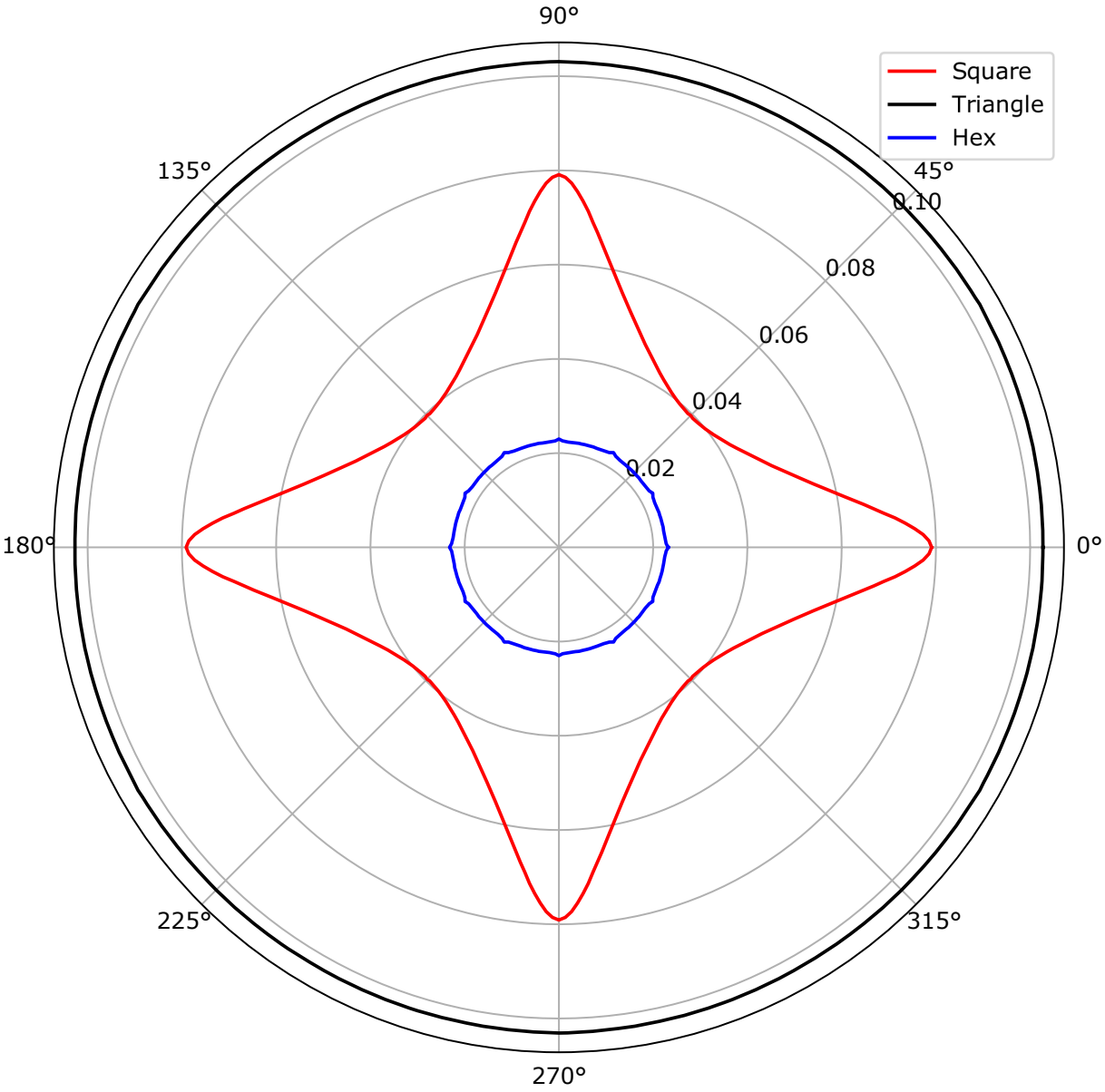

Figure 6.13: Polar plot showing the effective elastic modulus with lateral constraint (fully constrained) for 2D square, triangular and hexagonal lattices.

Figure 6.14 shows the effective shear modulus for square, triangular and hexagonal lattices. The square lattice has the lowest effective shear modulus at 30°, and the highest at 45°. The effective shear modulus of the square lattice is greater than that of the hexagonal lattice between 5° and 85° $\pm 90°n$; and greater than that of the triangular lattice between 44° to 46° $\pm 90°n$. The effective shear modulus of the triangular lattice is larger than that of the hexagonal lattice.

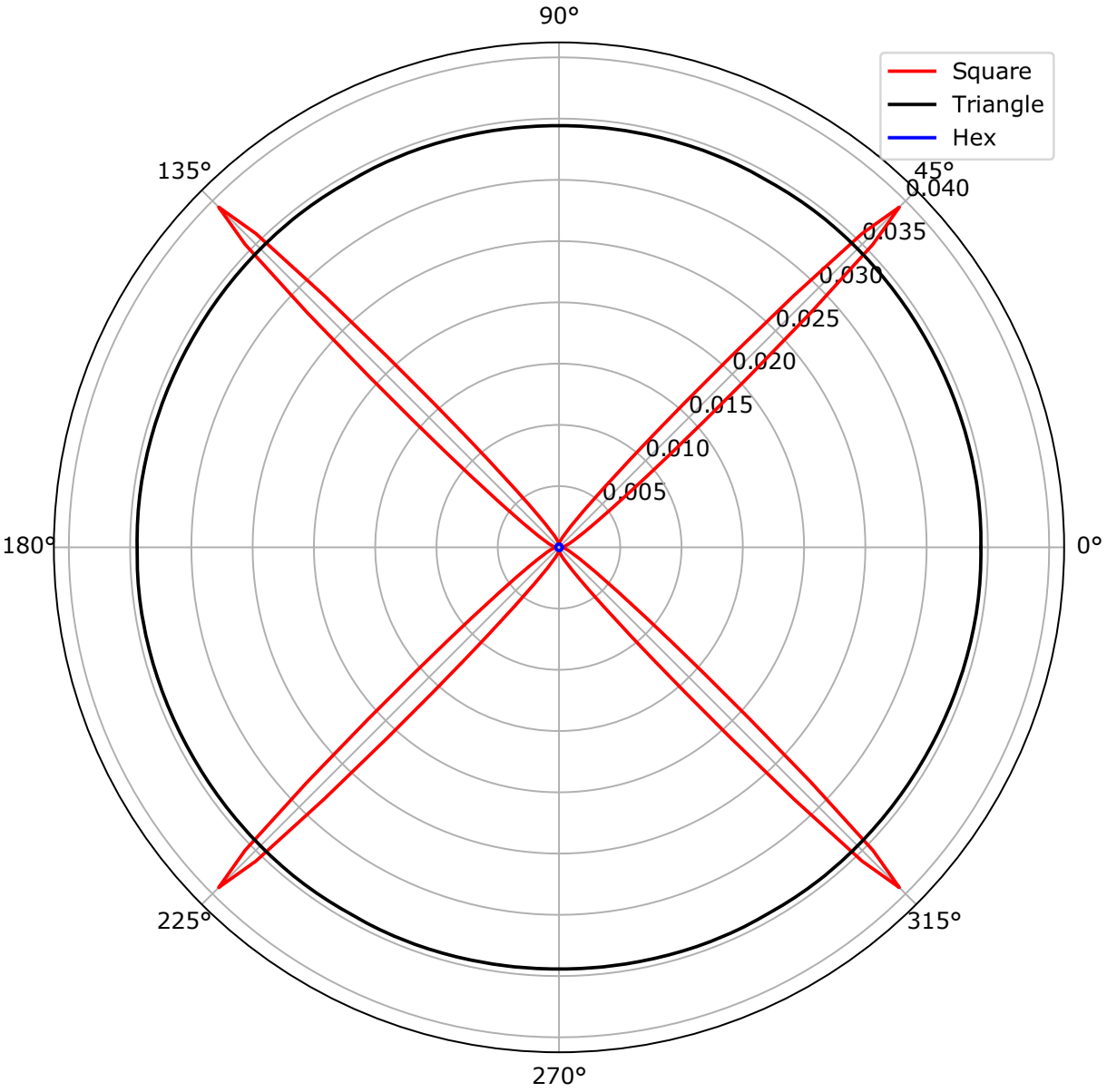

Figure 6.14: Polar plot showing the effective shear modulus with with lateral constraint (fully constrained) for 2D square, triangular and hexagonal lattices.

Overall, for the same beam geometry, the hexagonal lattice is the most compliant. It only exceeds the mechanical properties of the square lattice under certain angular regions. The triangular lattice has the greatest effective mechanical properties overall, only being exceeded by the shear modulus of the square lattice in a very small angular band (44° to 46° $\pm 90°n$).

6.3.1 Relative Density Normalisation

The lattices have varying relative densities (the amount of material vs. free space in a unit volume), which has a large effect on the mechanical properties [6]. Table 6.6 shows the relative densities of the three 2D lattices and the formula used [6].

Table 6.6: Relative densities of 2D square, triangular and hexagonal lattices.

Lattice	**Formulae**	**Relative Density** ρ_{rel}
Square	$\rho_{relsquare} = 2\frac{t}{l}(1 - \frac{1}{2}\frac{t}{l})$	0.190
Triangular	$\rho_{reltriangle} = 2\sqrt{3}\frac{t}{l}(1 - \frac{\sqrt{3}}{2}\frac{t}{l})$	0.316
Hexagonal	$\rho_{relhex} = \frac{2}{\sqrt{3}}\frac{t}{l}(1 - \frac{1}{2\sqrt{3}}\frac{t}{l})$	0.112

Figure 6.15 shows the density normalised response of the 2D lattices. Normalising by density is a measure of the efficiency of the structure as a function of material used, or weight of the final structure.

If the whole lattice has no lateral confinement (unconstrained boundary condition), the triangular is consistently stiffer than the hexagonal lattice as expected. However, the triangular lattice is more compliant than the square lattice between $-3°$ to $3°$ $\pm 90°n$. The hexagonal lattice is stiffer than the square at certain angles. Normalising by density increases this band by $5°$ where the new region is only $25°$ to $65° \pm 90°n$.

The lattice with lateral confinement (fully constrained) demonstrates that, like the unconstrained case, the triangular is least compliant overall. The square lattice is only stiffer over the angles $-10°$ to $10°$ $\pm 90°n$. Interestingly, the hexagonal lattice response is the most compliant at all angles even after normalising by density, unlike the unconstrained case.

The shear response shows that, similar to the previous, the triangular response is overall the least compliant with the square lattice response only becoming stiffer over a small angle band; namely $42°$ to $48°$ $\pm 90°n$. The hexagonal lattice has a greater shear modulus over the angles $-15°$ to $15°$ $\pm 90°n$.

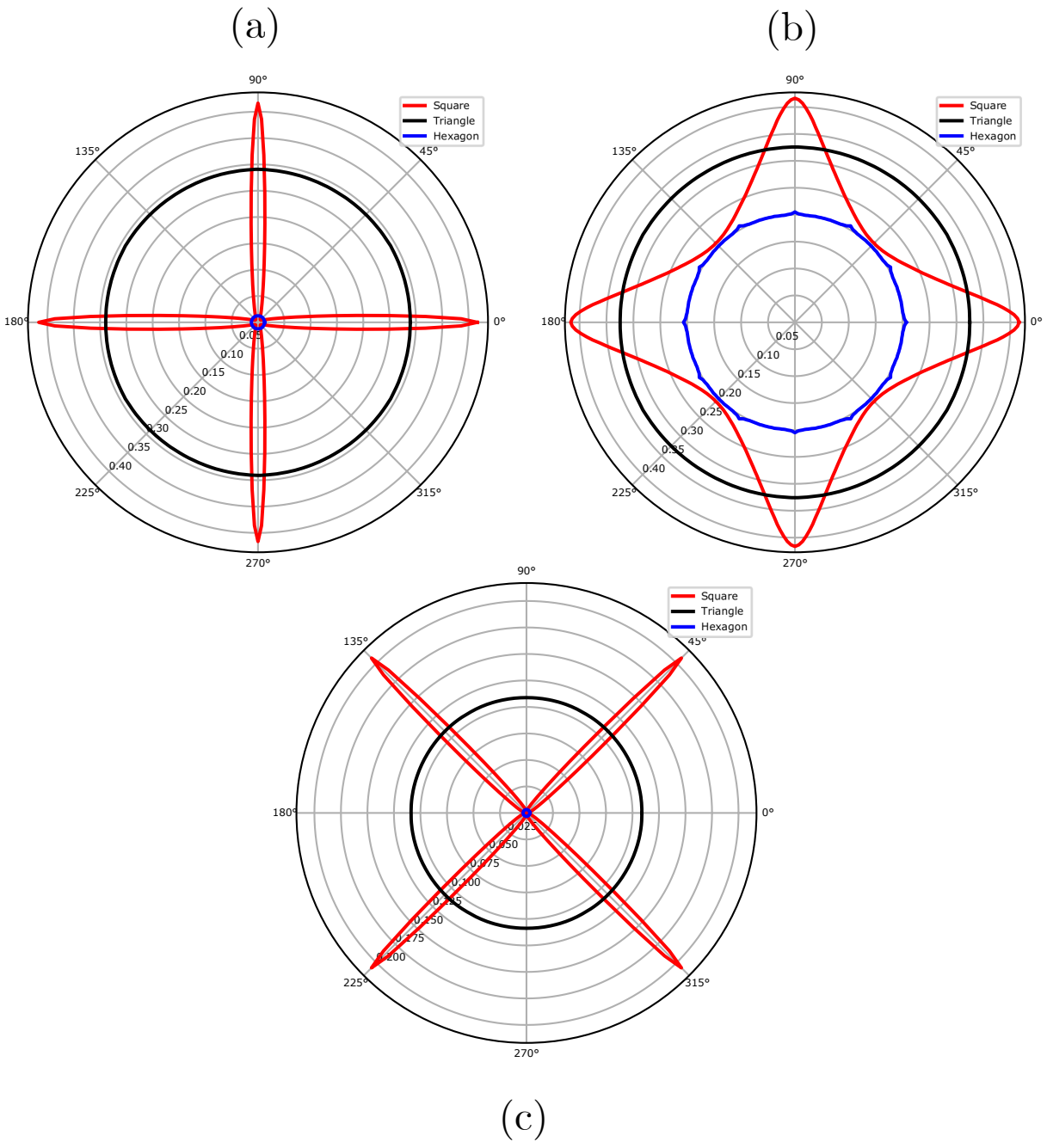

Figure 6.15: Polar plot showing the effective elastic modulus, normalised by relative density for 2D square, triangular and hexagonal. (a) Unconstrained (b) Fully constrained (c) Shear.

6.4 Effective Elastic Properties of 3D lattices

The following section outlines the effective mechanical properties of the 3D discrete lattice models investigated in this research. The effective properties are quoted as relative to the parent material, as in the 2D lattice response. The properties are presented as polar plot surfaces, where each point on the surface represents the effective property in that direction.

6.4.1 Cubic Lattice

The elastic modulus in the unconstrained and fully constrained boundaries along the principal direction (x, y, z) can be calculated as the ratio between the summation of cross sectional areas for each strut and the projected or total area. For a unit cell side length l and a number of struts n, the effective stiffness is calculated as (see Appendix C for derivation):

$$E_{rel} = \frac{A_{cs} n}{l(\sqrt{n} - 1)^2}. \tag{6.3}$$

Like the 2D square, the analytical solution of the cubic lattice is a function of the number of vertical columns in the whole lattice. The asymptote of Equation 6.3 represents the bulk behaviour. Equation 6.4 shows the bulk relative effective stiffness for the cubic lattice with a circular cross section.

$$E_{relBulk} = \frac{A_{cs}}{l} = \frac{\pi r^2}{l} \tag{6.4}$$

Figure 6.16 shows the relative effective elastic modulus converging to the analytical solution ($E_{relBulk} = 0.007853$) as the number of cells increases. The percentage difference between the numerically determined values and the theoretical values using Equation 6.3 are consistently under 0.03%, confirming the robustness of the derivation method. The difference between the numerically determined values and the bulk theoretical value decreases from 300% to 7% for 1 to 27^3 cells.

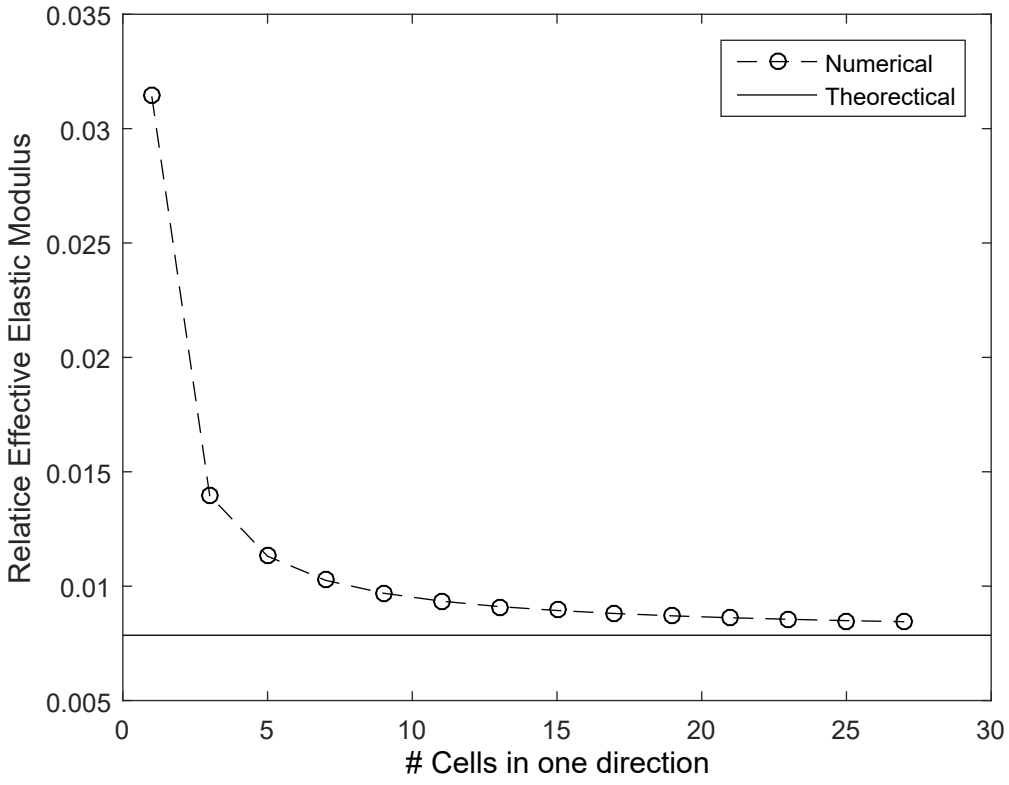

Figure 6.16: Relative effective elastic modulus for cubic lattice with different number of cells. Note: x-axis is the number of cells along any direction, the total number of cells in the lattice being $\#cells^3$.

Figure 6.17 shows the CPU time taken for varying number of unit cells. The time taken for a large number of cells remains small and was therefore not a consideration in deciding on number of cells to calculate the polar plot shown in Figure 6.18.

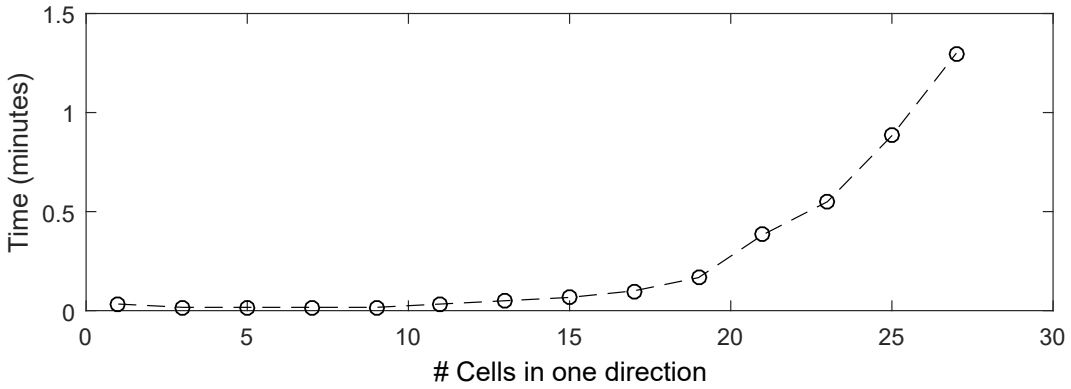

Figure 6.17: The simulation time for different size cubic lattices. Note: x-axis is the number of cells along any direction, the total number of cells in the lattice being $cells^3$.

Figure 6.18 shows the polar plot of effective elastic modulus for unconstrained and fully constrained cases. The polar plot was generated using a cubic lattice with 27^3 cells to approach bulk behaviour. The lattice was simulated at 271 orientations.

The response of the cubic lattice is the 3D extension of the 2D square lattice, for both unconstrained and fully constrained cases. The cubic lattice shows a high degree of mechanical anisotropy, with the relative elastic modulus along the principal directions being 92 times greater than the minimum relative elastic modulus, along the $(1, 1, 1)$ direction.

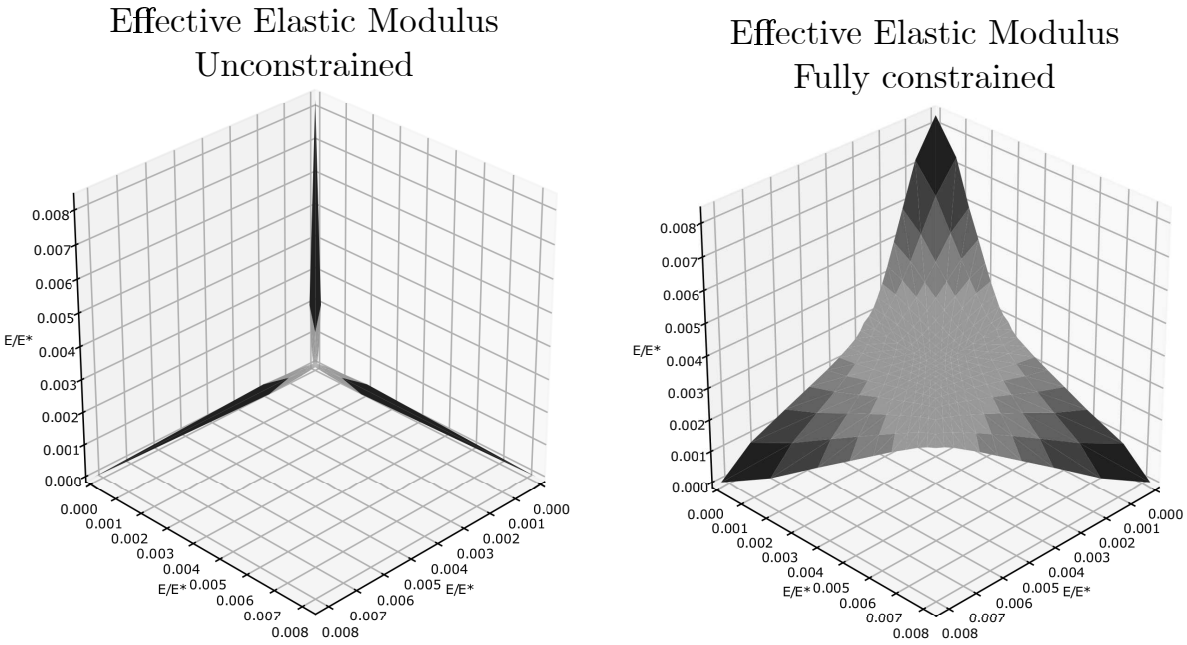

Figure 6.18: Polar plot showing the effective elastic modulus for unconstrained and fully constrained cases for the 3D cubic lattice.

Figure 6.18 shows that the effective elastic modulus in the unconstrained and fully constrained boundaries is the same in the (x, y, z) directions, as in that orientation the Poisson's ratio of the lattice is 0 and therefore the lateral confinement has no effect. Similarly, the Poisson's ratio is greatest in the $(1, 1, 1)$ direction, which corresponds to the largest difference in effective elastic modulus, where the fully constrained case is 28 times greater than the unconstrained case.

Table 6.7: Minimum and maximum effective elastic modulus for cubic lattice.

	Unconstrained	**Fully constrained**
Maximum	8.296×10^{-3}	8.296×10^{-3}
Minimum	9.390×10^{-5}	2.684×10^{-3}

The values shown in Table 6.7 correspond to a difference of 5.6% compared to the bulk behaviour ($E_{bulk} = 7.853 \times 10^{-3}$). It should be noted that this is not numerical error in the conventional sense as the numerically determined values have a very high agreement with the analytical solution shown in Equation 6.3. The difference is a measure of how close the response is to bulk behaviour which is dependent on the number of cells used.

6.4.2 Octet-Truss Lattice

Deshpande et al. [59] provides an analytical solution by assuming axial deformation dominant behaviour (no contribution of bending and shear deformation). Equation 6.5 shows the analytical solution to the effective elastic modulus for the octet truss along in the (x, y, z) directions:

$$E_{eff} = \frac{2\sqrt{2}\pi}{3}\left(\frac{r}{l}\right)^2, \tag{6.5}$$

where r and l are the radii and lengths of the beams. Figure 6.19 shows the convergence of the relative effective elastic modulus to the bulk behaviour calculated via Equation 6.5, which has a value of 7.4×10^{-3}. It clearly demonstrates that the numerically determined relative effective modulus does converge to the bulk behaviour with the percentage difference decreasing from 54% with one unit cell to 4% for 27^3 cells.

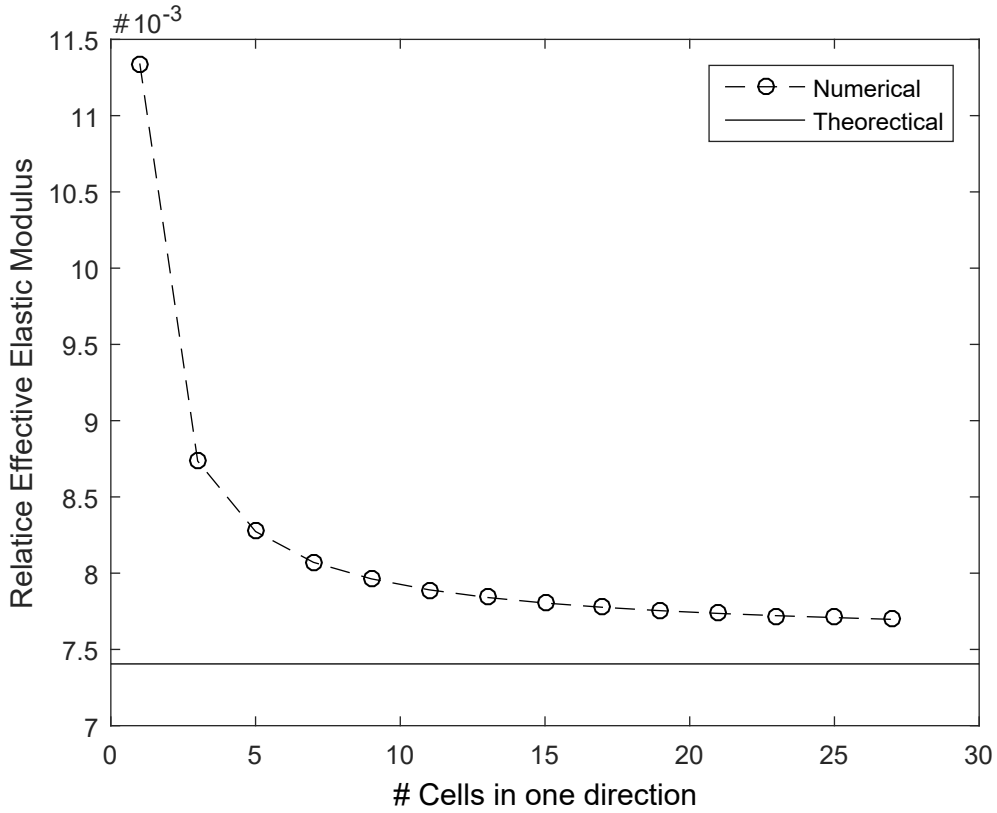

Figure 6.19: Relative effective elastic modulus for octet-truss lattice with different number of cells. (Note: x-axis is the number of cells along any direction, the total number of cells in the lattice being $\#cells^3$).

Figure 6.20 shows the simulation time taken for a different number of cells. The time taken for 27^3 cells is 11.1 minutes for a single orientation, which implies 5.1 days to generate the full polar plot with two constraint cases. The octet-truss lattice that was used to generate the polar plot of effective stiffness had 12^3 cells, which equates to roughly 6% difference compared to bulk behaviour and takes 5.5 hours to complete (30 seconds per simulation), excluding time to generate the lattice and process and generate the simulation jobs. The local maxima at 15^3 cells is likely to be due to computational load increased elsewhere on the computer as these were performed locally.

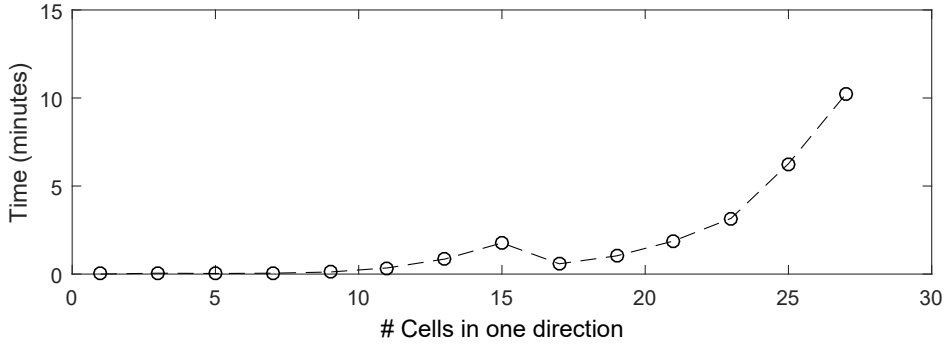

Figure 6.20: The simulation time for different size octet-truss lattices. (Note: x-axis is the number of cells along any direction, the total number of cells in the lattice being cells^3).

Figure 6.21 shows the relative effective elastic modulus for octet truss lattice structure. The response of the octet-truss was chosen as a 3D analogue for the 2D triangular lattice; which is isotropic with lateral constrained having a small effect due to a low Poisson's ratio. Figure 6.21 demonstrates that there is anisotropy present in the octet-truss lattices response, however a significantly lower degree of anisotropy than the cubic lattice. The constraint effect is small, similar to the 2D triangular lattice, which is indicative of a low Poisson's ratio.

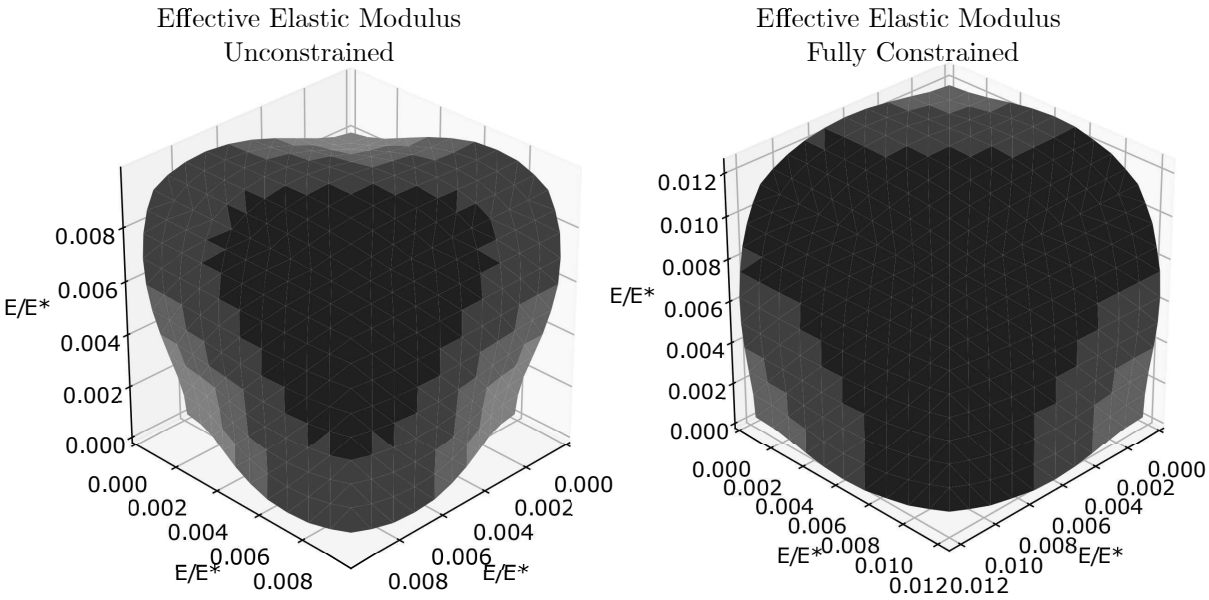

Figure 6.21: Polar plot showing the effective elastic modulus for unconstrained and fully constrained cases for the 3D octet-truss lattice.

Table 6.8 shows the minimum and maximum relative effective elastic modulus for unconstrained and fully constrained boundary conditions. The maximum relative effective elastic modulus is 1.8 and 1.4 times greater than the minimum for unconstrained and fully constrained cases respectively; demonstrating much lower mechanical anisotropy than the cubic lattice.

The effect of constraint is similarly small, as is the case with the 2D triangular lattice. The relative effective elastic modulus for the fully constrained case is 1.1 and 1.5 times greater than that of the unconstrained case for the maximum and minimum values respectively.

Table 6.8: Minimum and maximum effective elastic modulus for octet-truss lattice.

	Unconstrained	**Fully constrained**
Maximum	1.427×10^{-2}	1.595×10^{-2}
Minimum	7.881×10^{-3}	1.170×10^{-2}

Table 6.9 shows the differences between numerically determined and analytically calculated values for Figure 6.21. The numerically determined values are greater than that of the analytically determined

values; this is likely due to a combination of the analytical values ignoring bending and shear deformation and the number of cells being constrained by computational limitations.

The analytical solution for the effective elastic modulus in the $(1, 1, 1)$ direction is [59]:

$$E_{eff} = \frac{6\sqrt{2}\pi}{5}(\frac{r}{l})^2 \tag{6.6}$$

Table 6.9: Comparison between analytical and numerically determined effective elastic modulus for octet-truss lattice.

Direction	**Numerical**	**Analytical**	**Difference (%)**
x,y,z	7.881×10^{-3}	7.405×10^{-3}	6.42
(1,1,1)	1.427×10^{-2}	1.339×10^{-2}	6.57

6.4.3 Kelvin Cell Lattice

Zhu et al. [68] derives an analytical solution for the effective elastic modulus in the (x, y, z) direction, including axial, shear and bending deformation using a unit cell modelling approach. The analytical solution for the Kelvin cell is:

$$E_{eff} = \frac{3\sqrt{(2)}r^4}{2(1+3r^2)}. \tag{6.7}$$

Figure 6.22 shows a plot of the relative effective elastic modulus with increasing number of cells in the lattice. It demonstrates convergence with increasing number of cells, which is converging to the analytical value of 4.13×10^{-5}, calculated using Equation 6.7. The percentage difference, compared to bulk behaviour, decreases from 40% for a unit cell to 5% for 27^3 cells.

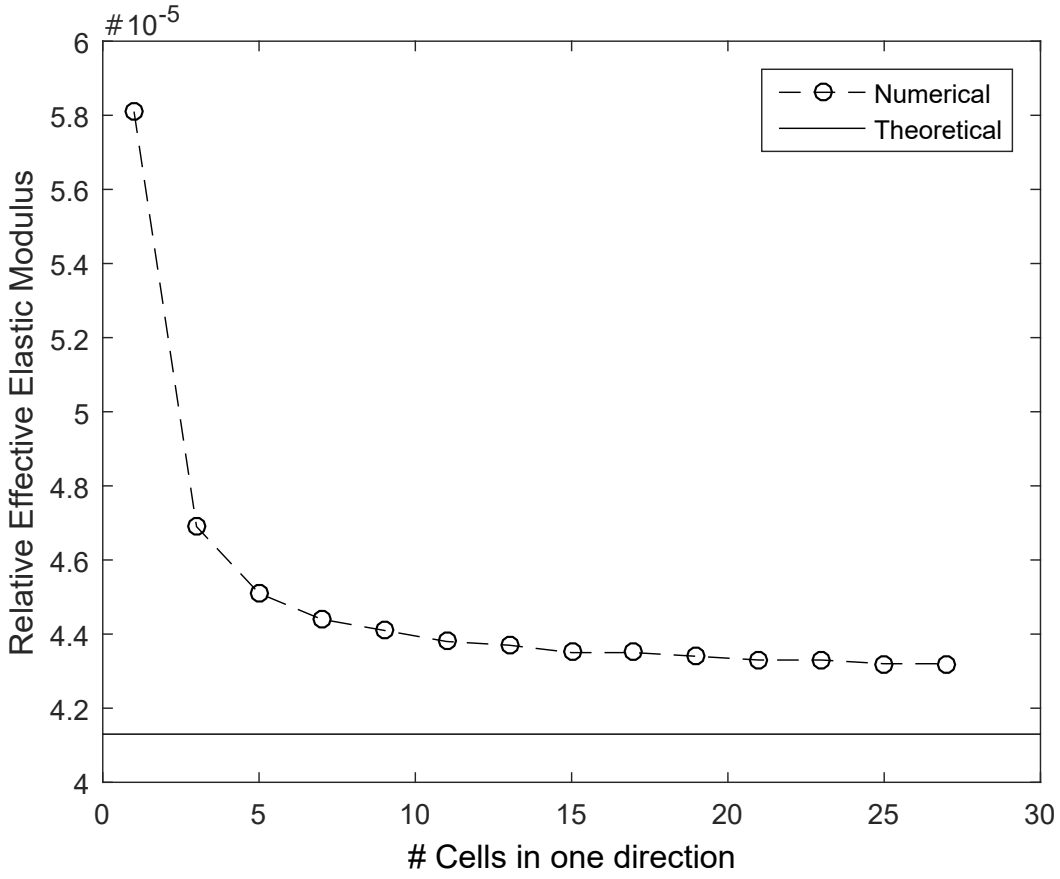

Figure 6.22: Relative effective elastic modulus for Kelvin cell lattice with different number of cells. (Note: x-axis is the number of cells along any direction, the total number of cells in the lattice being $\#cells^3$).

Figure 6.23 shows the simulation time for the Kelvin cell lattices with different number of cells. The time taken for 27^3 cells is 22 minutes, double than that of the octet-truss lattice at the same number of cells. Using that number of cells would equate to 9.8 days to generate the plot of anisotropy with two constraints, ignoring time taken to generate the lattice and process and generate the simulations at different orientations. This was not feasible due to computational and time constraints. The lattice used to generate the polar plot used 16^3 unit cells, which was predicted to take between 5.3 and 8.9 hours excluding lattice generation and processing and generation of simulations at different orientations. This was chosen due to the expected error being reasonable given the computational and time constraints.

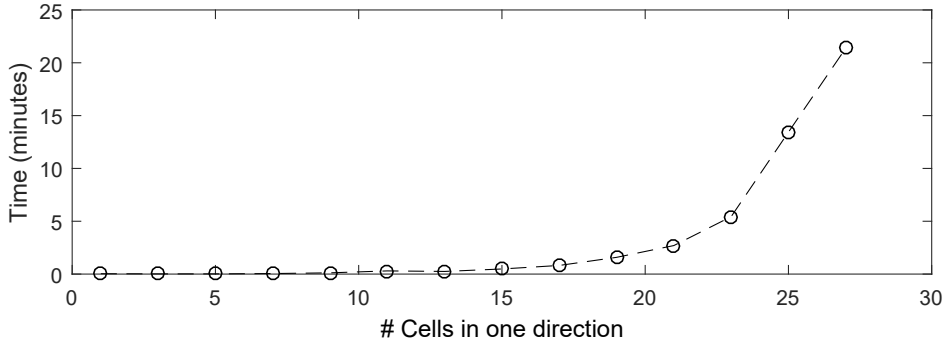

Figure 6.23: The simulation time for different size octet-truss lattices. Note: x-axis is the number of cells along any direction, the total number of cells in the lattice being cells^3.

Figure 6.24 shows the relative effective elastic modulus for the Kelvin cell lattice structure. The response of the Kelvin cell was investigated as a 3D facsimile for 2D hexagonal lattice. The response is isotropic with lateral constraint having a large effect. There is a similar behaviour to the fully constrained 2D hexagonal case with local maxima.

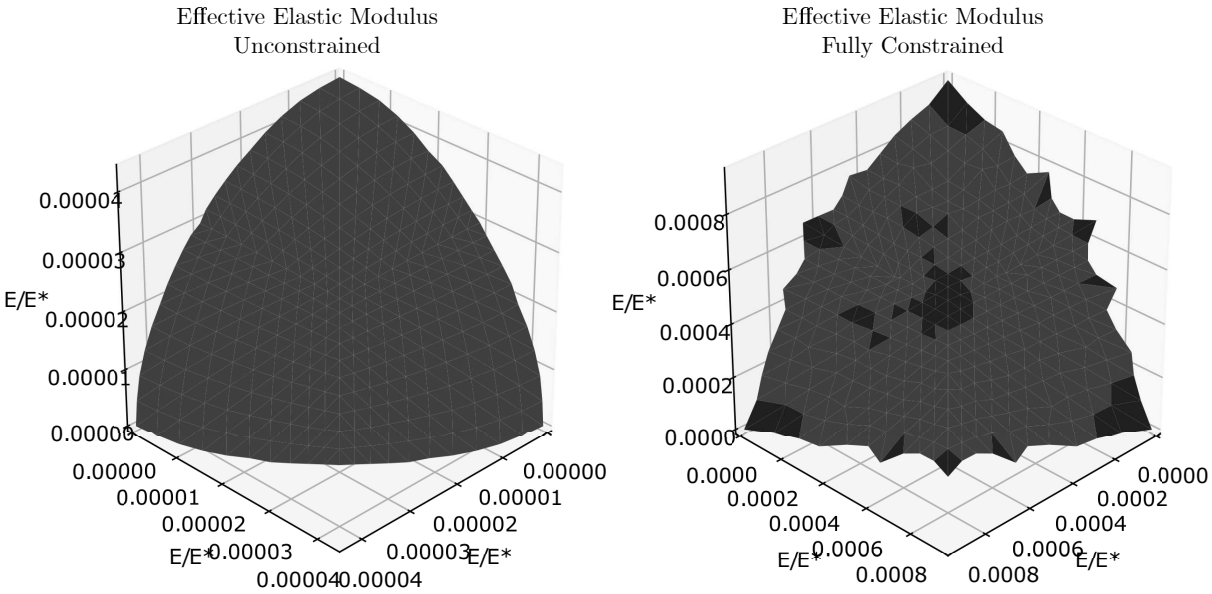

Figure 6.24: Polar plot showing the effective elastic modulus for unconstrained and fully constrained cases for the 3D kelvin cell lattice.

Table 6.10 shows the minimum and maximum relative effective elastic modulus for the unconstrained and fully constrained boundary conditions. The maximum unconstrained value occurs along the 3 principal directions, with the other directions having a slightly lower stiffness. The maximum unconstrained relative effective stiffness is 1.05 times greater than the minimum, and only 1.02 times greater than the average stiffness. The deviation from isotropy is small enough to be considered an difference associated with convergence to bulk behaviour.

The relative effective elastic modulus along the principal directions corresponds to an percentage difference of 5.33% compared to the bulk analytical solution [68].

Table 6.10: Minimum and maximum effective elastic modulus for Kelvin cell lattice.

	Unconstrained	**Fully constrained**
Maximum	4.35×10^{-5}	9.67×10^{-4}
Minimum	4.17×10^{-5}	7.32×10^{-4}

6.5 3D Lattice Comparison

Figure 6.25 shows the minimum and maximum effective elastic moduli for all three 3D lattices investigated. It demonstrates that the octet truss lattice has the highest average effective elastic moduli, however the cubic lattice's maximum elastic modulus (along x, y, z directions) are greater than that of the octet truss lattice's unconstrained minimum elastic modulus.

The Kelvin cell, like the 2D hexagonal lattice, has the lowest effective elastic moduli overall. The maximum and minimum unconstrained elastic moduli for the Kelvin cell are near coincident, verifying the isotropic behaviour. The effect of the local spiking in the fully constrained case is seen as the two markers for the minimum and maximum elastic modulus are not coincident.

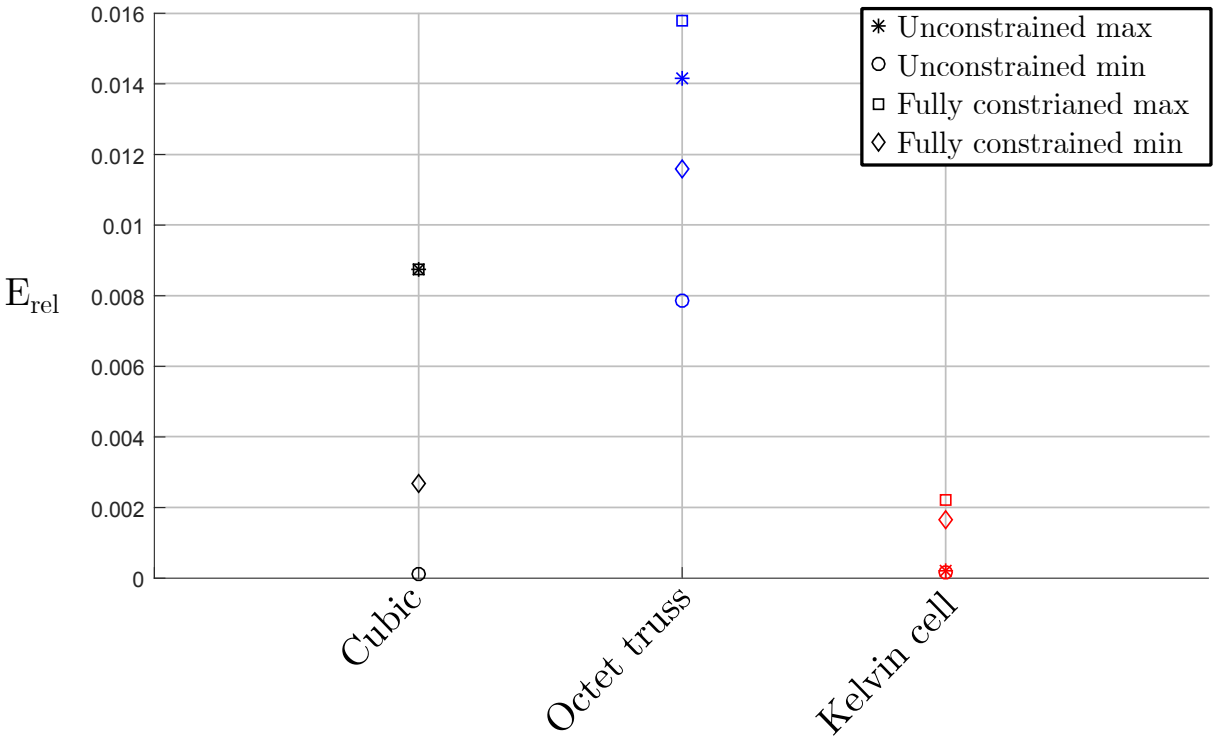

Figure 6.25: The effective elastic modulus for unconstrained and fully constrained cases for the cubic, octet-truss and Kelvin cell lattices.

6.5.1 Relative Density Normalisation

The effective elastic modulus was normalised by relative density which was calculated as the BV/TV microstructural index calculated using BoneJ (see Chapter 8). Similar to Section 6.3.1, this shows how efficiently each lattice uses the material. Table 6.11 shows the minimum and maximum values for the unconstrained and fully constrained effective elastic moduli for all 3D lattices.

Table 6.11: The density normalised effective elastic modulus with unconstrained (UC) and fully constrained (FC) boundary conditions for the cubic, octet-truss and Kelvin cell lattices.

	Cubic		**Octet Truss**		**Kelvin**	
	UC	**FC**	**UC**	**FC**	**UC**	**FC**
Maximum	3.073×10^{-1}	3.073×10^{-1}	2.068×10^{-1}	2.312×10^{-1}	4.350×10^{-3}	9.670×10^{-2}
Minimum	3.480×10^{-3}	9.941×10^{-2}	1.142×10^{-1}	1.696×10^{-1}	4.170×10^{-3}	7.321×10^{-2}

Figure 6.26 shows a plot of the above data. This clearly demonstrates that the maximum effective elastic modulus of the cubic lattice (which is along the principal directions) has the highest effective elastic modulus of all lattices. With the fully constrained boundary conditions, the cubic response has a greater elastic modulus than any of the Kelvin cell lattice. However if the unconstrained boundary is considered the cubic lattice is more compliant in the $(1, 1, 1)$ direction than the unconstrained Kelvin cell lattice.

Other than the cubic lattice in the principal directions, both the unconstrained and fully constrained response of the octet-truss lattice is less compliant than the other lattices. The octet-truss lattice has the most efficient usage of material in providing stiffness.

Similarly, the Kelvin cell has the least efficient usage of material in providing stiffness other than a small angular range around the most compliant response of the cubic lattice.

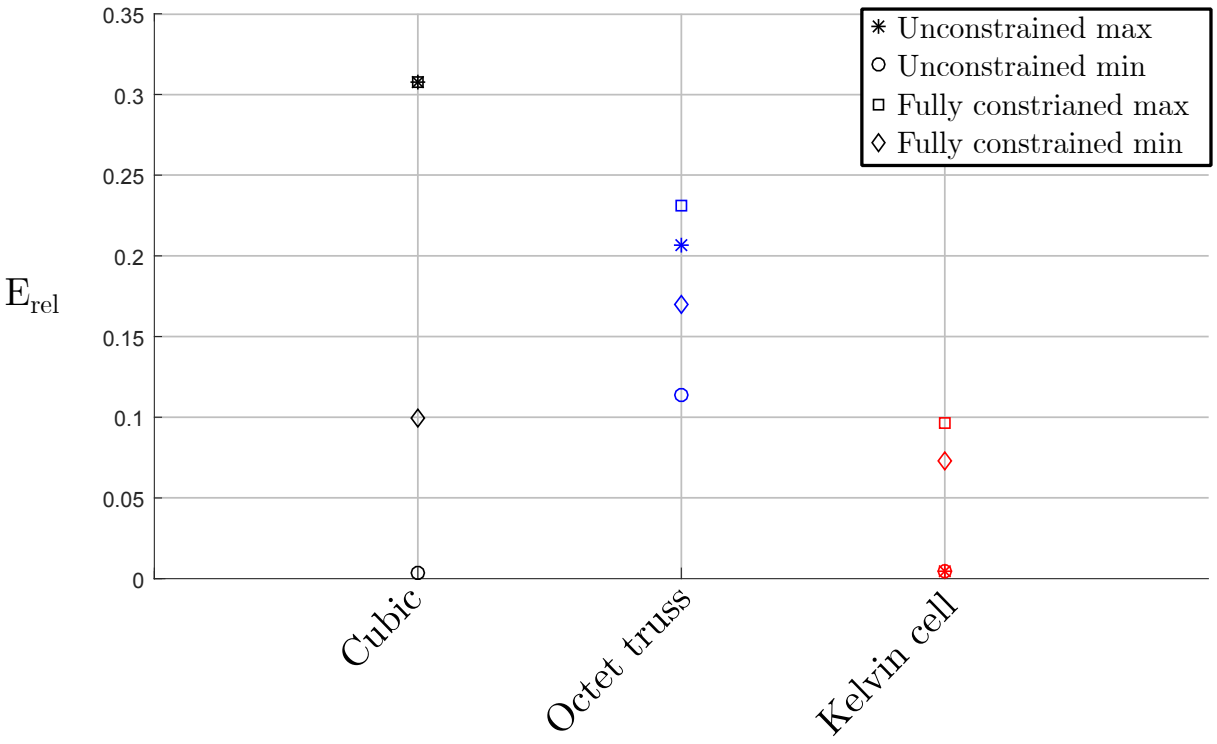

Figure 6.26: The effective elastic modulus, normalised by density, for unconstrained and fully constrained cases for the cubic, octet-truss and Kelvin cell lattices.

Chapter 7

Continuum Modelling Results

7.1 2D Continuum Model

This section outlines various tests showing the 2D continuum model converging to the discrete model by increasing mesh resolution. The mesh convergence is shown globally by comparing the macroscopic stiffness of the continuum model to the discrete model for the two confinement types (see Section 3.5 for more detail on how the macroscopic stiffness is calculated). The mesh convergence is also shown by visually comparing the displacement fields to confirm that the internal response converges to the discrete model results.

Figure 7.1 and Figure 7.2 show the effective stiffness of the discrete model and continuum models with increasing number of elements on a polar plot and the relative error at varying angles for the 2D square lattice. This demonstrates that the global response of the continuum model does converge to the discrete model with increasing mesh resolution. However, both the error and the rate at which convergence occurs does vary with the loading angle.

The unconstrained boundary condition (Figure 7.1) shows the response immediately convergences with only one element and the maximum relative error is acceptable at 0.61% regardless of mesh resolution. The fully constrained boundary condition (Figure 7.2) show convergence with increased mesh resolution, with the peak relative error going from 28% to 4.5% for 1 to 121 elements respectively. The error at 0°, 45° and 90° are the same regardless of mesh resolution.

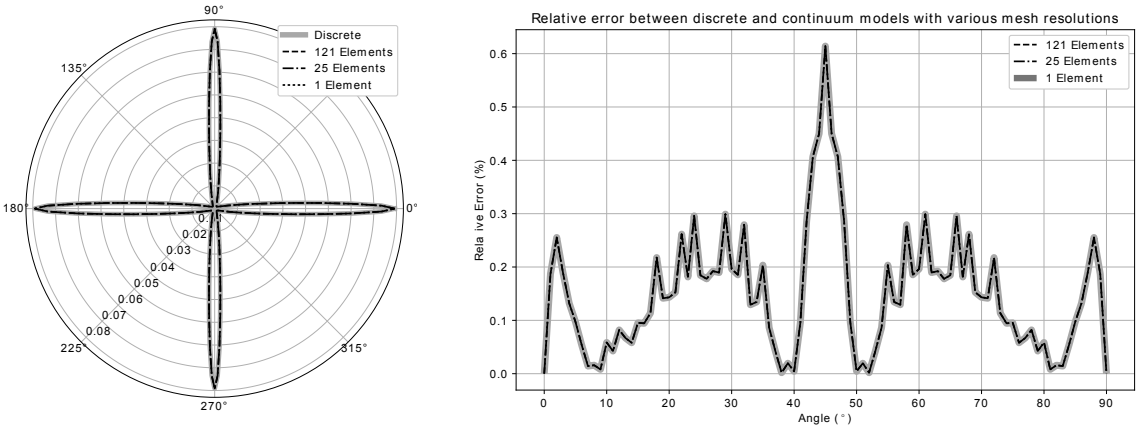

Figure 7.1: 2D Square lattice continuum model mesh convergence with unconstrained boundary type.

The error in continuum models are higher when non-uniform displacement fields are present. This can be demonstrated by comparing unconstrained and fully constrained cases, along with the changes in error with angle in the fully constrained case.

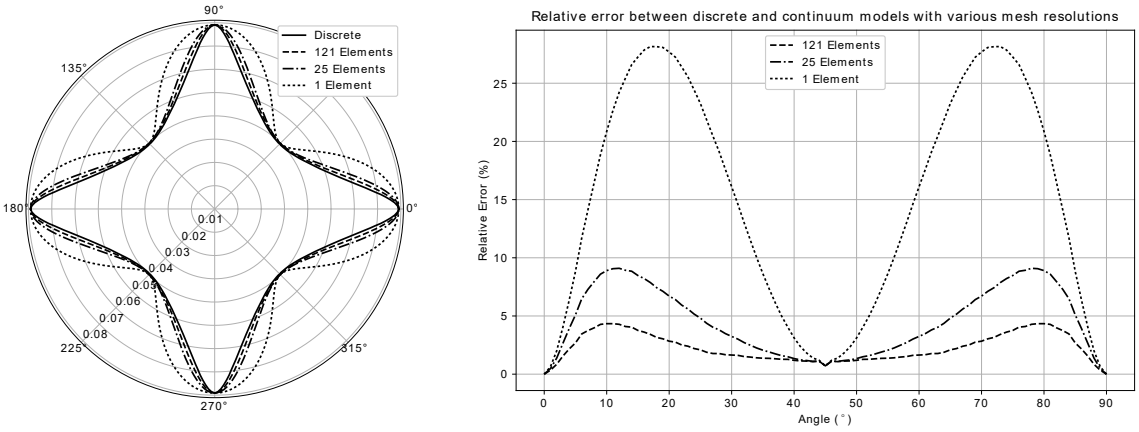

Figure 7.2: 2D Square lattice continuum model mesh convergence with fully constrained boundary type.

The unconstrained case results in simpler and uniform displacement fields, unlike the fully constrained case. Figure 7.3 shows contours of y-displacement for the same loading and rotation, demonstrating the difference between the displacement field in unconstrained and fully constrained boundaries.

The fully constrained error is zero at 0° and 90°, where fully uniform displacement is present. There is a local minima at 45°, which also has a uniform displacement field. The error locally spikes around 10° to 15°, where the highest non-uniformity can be seen in the displacement field; demonstrated by comparing 7.3a and 7.4j which show contours of y-displacement for 12° and 30° respectively.

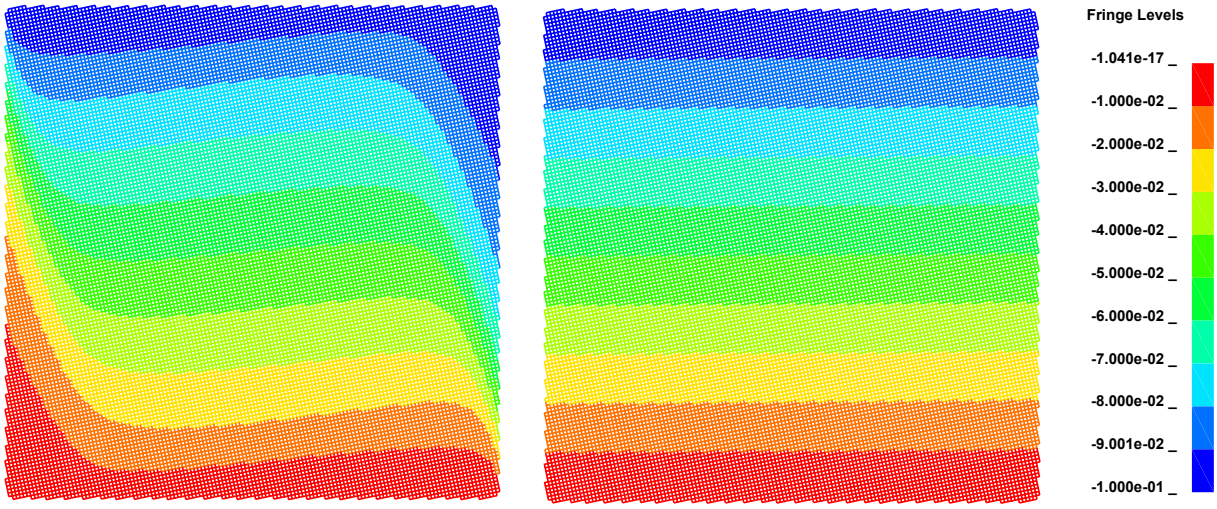

(a) (b)

Figure 7.3: Contours of y-displacment for 2D square lattice loaded at 12° with two confinement types: (a) Fully constrained (b) Unconstrained.

Figure 7.4 shows contours of the y-displacement for the 2D square lattice, rotated by 30°, under a fully constrained boundaries. This demonstrates the convergence of of the internal displacement field in the continuum model as the number of elements is increased from 1 to 289 elements (Figure 7.4a to i) to the displacement field in the discrete model. The number of elements and nodes are shown in Table 7.1.

Table 7.1: Number of nodes and elements in simulations shown in Figure 7.4.

	a	b	c	d	e	f	g	h	i	j
Nodes	4	16	36	64	100	144	196	256	324	56684
Elements	1	9	25	49	81	121	169	225	289	37664

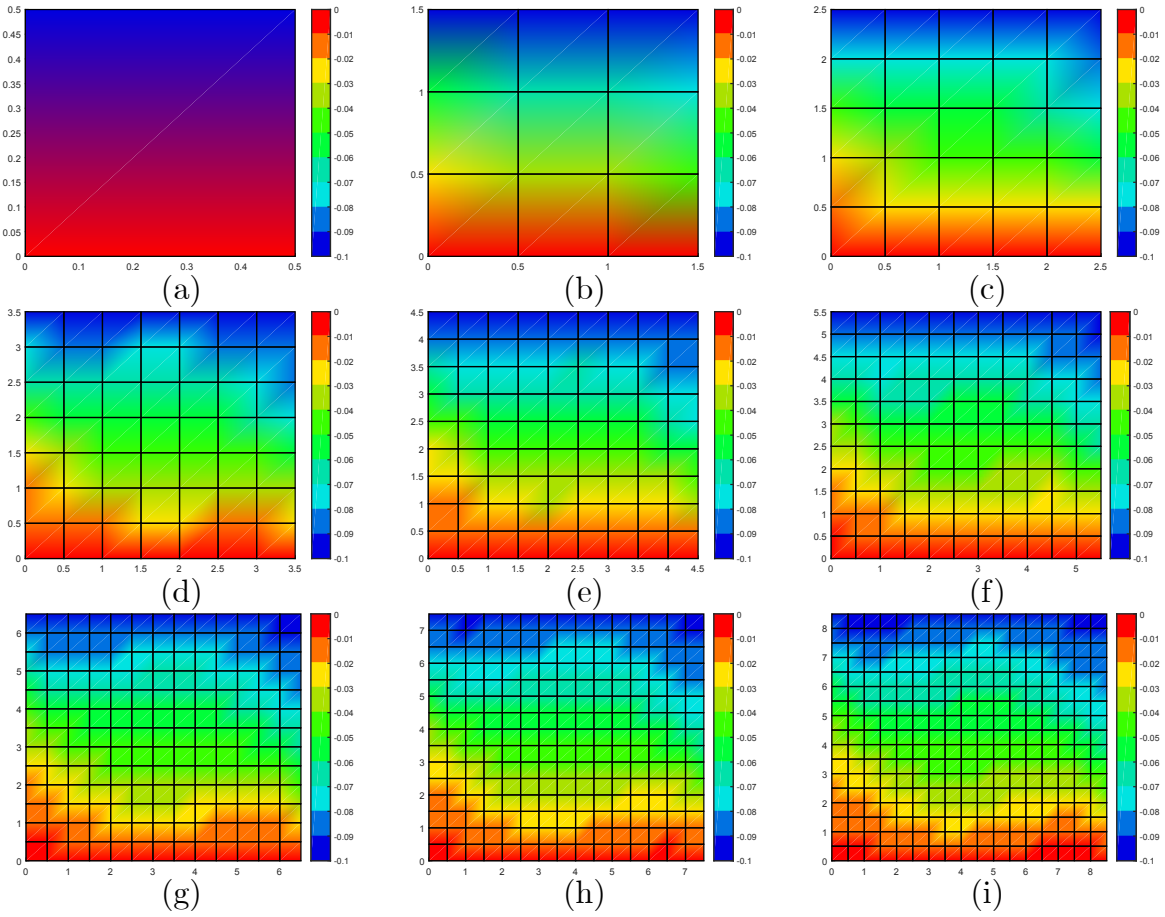

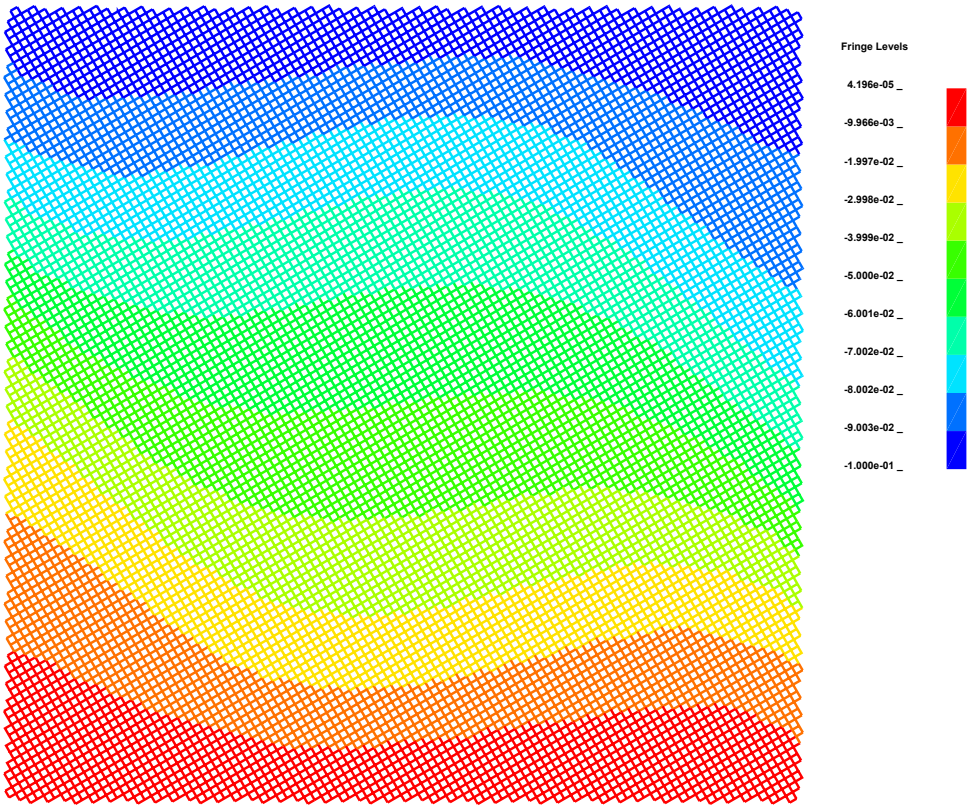

(j)

Figure 7.4: Contours of y-displacement for 2D square lattice rotated at 30°: (a-i) Continuum models (j) Discrete model solved in LS-DYNA.

Figure 7.5 shows the global error in macroscopic stiffness for both unconstrained and fully constrained cases for the triangular mesh. The continuum model converges with only one element as the triangular lattices induce uniform displacement states. This is similar to the unconstrained behaviour in the 2D square lattice in the unconfined case (see Figure 7.1). However, the error in all cases are acceptable with peak errors of 0.39% and 0.48% for the unconstrained and fully constrained respectively. The polar plots of effective stiffness are not shown for the triangular mesh as the error is so low that the discrete and continuum models are visually indistinguishable.

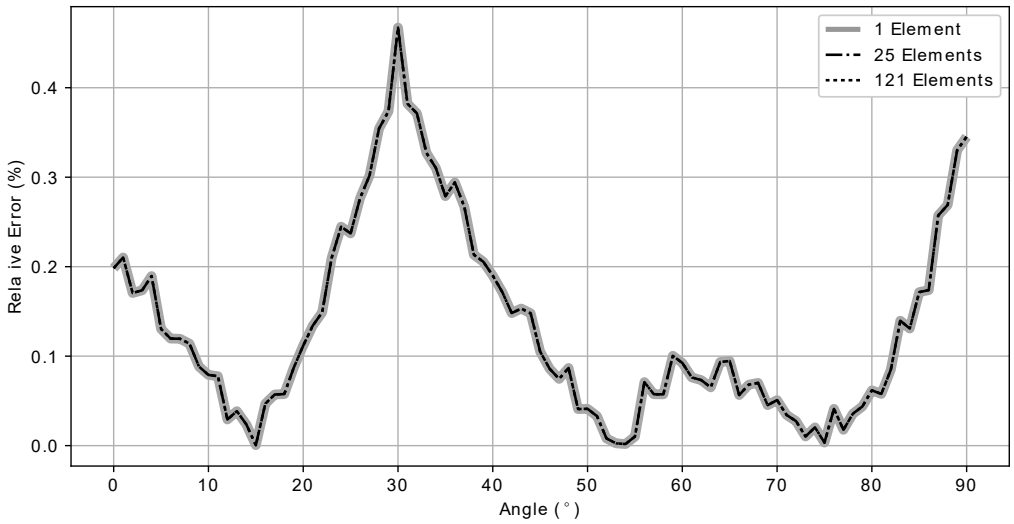

(a)

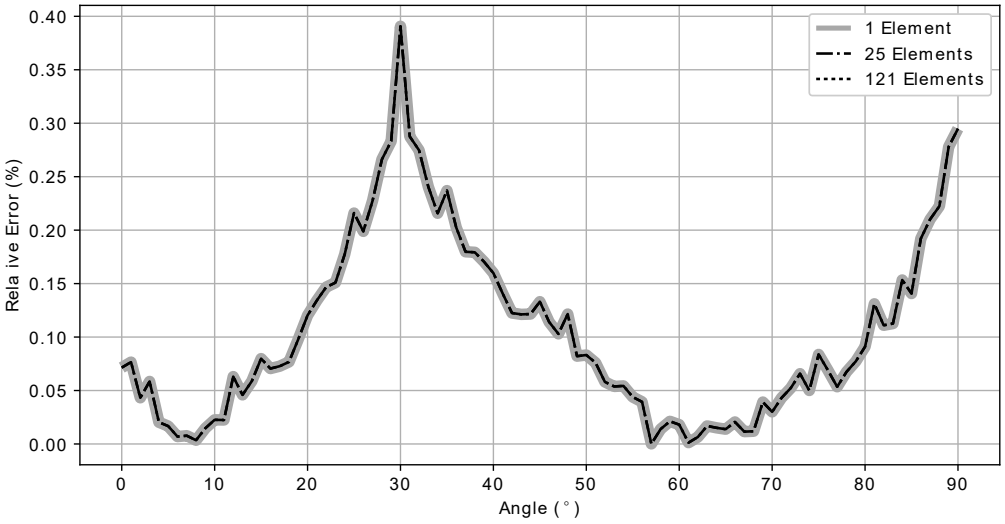

(b)

Figure 7.5: Relative error between discrete and continuum model of 2D triangular lattice for 2 constraint types: (a) Unconstrained boundary (b) Fully constrained boundary.

Figure 7.6 shows the global error in the macroscopic stiffness for both the unconstrained and fully constrained boundary conditions for the hexagonal lattice. Similar to the triangular lattice, increasing mesh resolution has no effect as the model converges with only one element due to the uniform strain state induced by the geometry. The error is acceptably low for the unconstrained case, with a peak error of 1.4% corresponding to a rotation of 30° and 90°, or the points down orientation. The error approaches zero for 0° and 60°, which both correspond to an unrotated state given the 60° rotational symmetry of hexagons.

The error is unacceptably high for the fully constrained boundary condition, with peak error of 20.7%. The error is lowest at 0° and 60° rotations (flats down orientation), with a value of 16.5%. There is a local minima in error at 30° and 90° with a value of 17.8%. Similar to the unconstrained state, the lowest errors are associated with the unrotated lattice. See Section 9.2.2.3 for discussion.

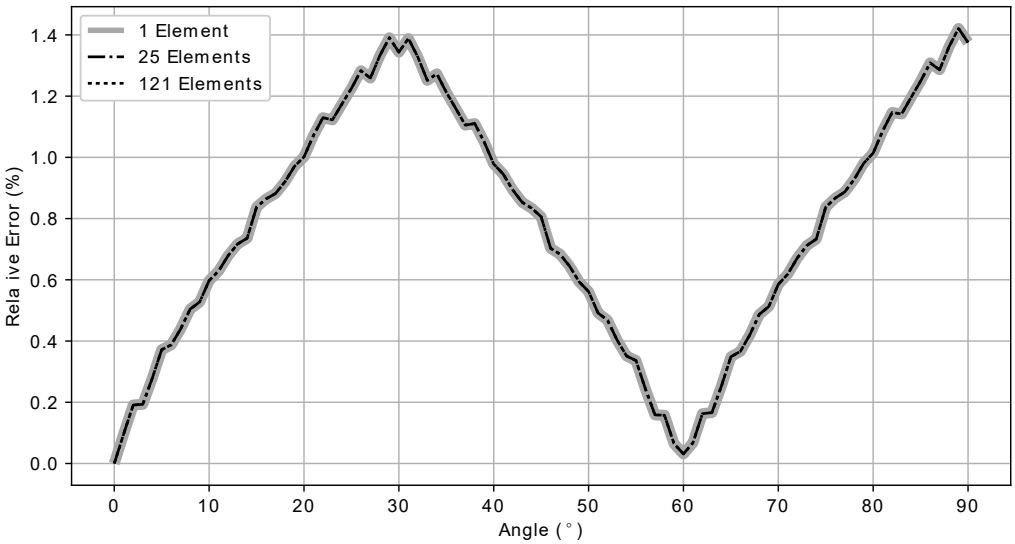

(a)

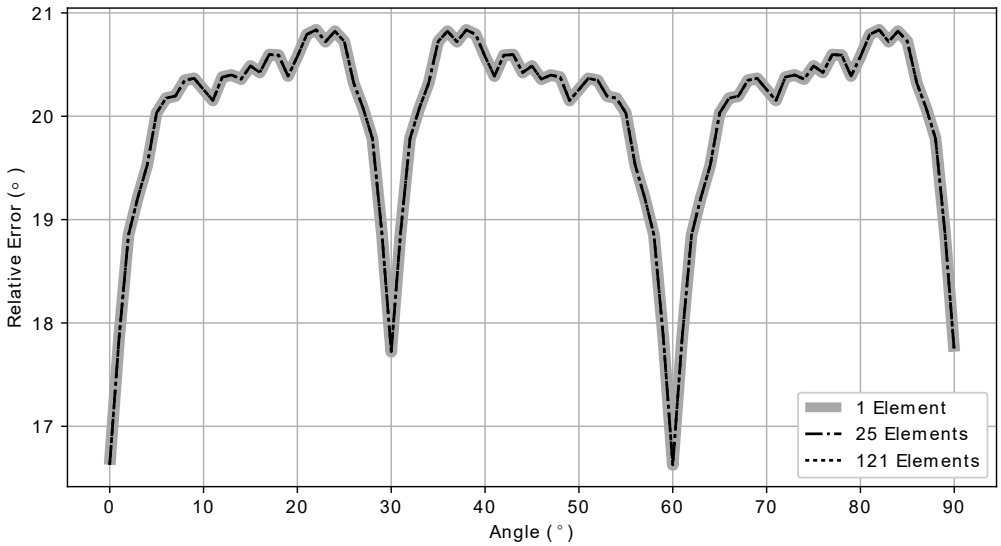

(b)

Figure 7.6: Relative error between discrete and continuum model of 2D hexagonal lattice for 2 constraint types: (a) Unconstrained boundary (b) Fully constrained boundary.

Figure 7.7 shows contour plots of the y-displacement for hexagonal and triangular lattices in the fully confined case, at an arbitrary rotation. This demonstrates the uniformity of the displacement field.

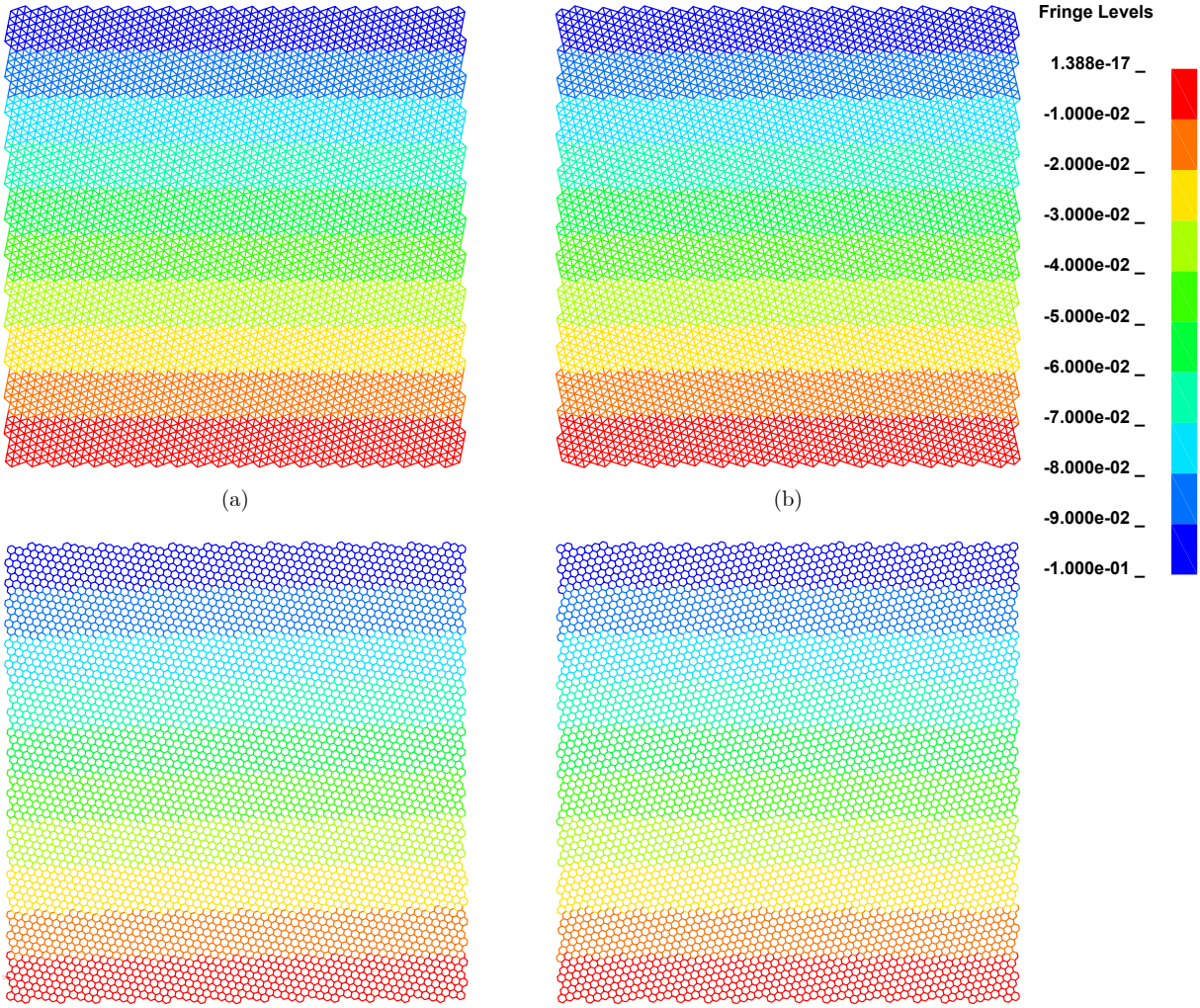

Figure 7.7: Contour plot of y-displacement demonstrating the uniform displacement fields for triangular and hexagonal lattices in arbitrary directions: (a) Triangular 19° (b) Triangular 43° (c) Hexagonal 19° (d) Hexagonal 43°.

7.2 3D Continuum Model

The elasticity matrices are calculated as described in Section 4.3. The same number of cells was used for all the lattices, namely 27^3.

7.2.1 Cubic Lattice Elasticity Matrix

Table 7.2 shows the effective mechanical properties for the cubic lattice. The elastic modulus and shear modulus is the same in all 3 principal directions, which is due to the symmetries of the lattice. Poisson's ratio is small enough to be considered zero due to floating point error, and is treated as being 0 in the calculation of the elasticity matrix.

Table 7.2: Effective mechanical properties for cubic lattice.

E_{11}	E_{22}	E_{33}	G_{23}	G_{13}	G_{12}
8.45×10^{-3}	8.45×10^{-3}	8.45×10^{-3}	3.61×10^{-5}	3.61×10^{-5}	3.61×10^{-5}
ν_{21}	ν_{31}	ν_{12}	ν_{32}	ν_{13}	ν_{23}
-1.57×10^{-18}	-3.73×10^{-19}	4.90×10^{-19}	8.56×10^{-20}	1.00×10^{-18}	-1.39×10^{-18}

Equation 7.1 shows the elasticity matrix for the cubic lattice.

$$E_{cubic} = \begin{bmatrix} 8.446\times10^{-3} & 0 & 0 & 0 & 0 & 0 \\ 0 & 8.446\times10^{-3} & 0 & 0 & 0 & 0 \\ 0 & 0 & 8.446\times10^{-3} & 0 & 0 & 0 \\ 0 & 0 & 0 & 3.606\times10^{-5} & 0 & 0 \\ 0 & 0 & 0 & 0 & 3.606\times10^{-5} & 0 \\ 0 & 0 & 0 & 0 & 0 & 3.606\times10^{-5} \end{bmatrix} \tag{7.1}$$

7.2.2 Octet-truss Lattice Elasticity Matrix

Table 7.3 shows the effective mechanical properties for the octet-truss lattice. The elastic modulus, shear modulus and Poisson's ratio is the same in all 3 principal directions. This is expected due to the symmetries in the octet-truss structure. The Poison's ratio of the octet-truss lattice is similar to the 2D triangular lattice, 0.328.

Table 7.3: Effective mechanical properties for cubic lattice.

E_{11}	E_{22}	E_{33}	G_{23}	G_{13}	G_{12}
7.697×10^{-3}	7.697×10^{-3}	7.697×10^{-3}	5.704×10^{-3}	5.704×10^{-3}	5.704×10^{-3}
ν_{21}	ν_{31}	ν_{12}	ν_{32}	ν_{13}	ν_{23}
0.329	0.329	0.329	0.329	0.329	0.329

Equation 7.2 shows the elasticity matrix for the octet-truss lattice.

$$E_{octet} = \begin{bmatrix} 1.140\times10^{-2} & 5.611\times10^{-3} & 5.611\times10^{-3} & 0 & 0 & 0 \\ 5.611\times10^{-3} & 1.140\times10^{-2} & 5.611\times10^{-3} & 0 & 0 & 0 \\ 5.611\times10^{-3} & 5.611\times10^{-3} & 1.140\times10^{-2} & 0 & 0 & 0 \\ 0 & 0 & 0 & 5.704\times10^{-3} & 0 & 0 \\ 0 & 0 & 0 & 0 & 5.704\times10^{-3} & 0 \\ 0 & 0 & 0 & 0 & 0 & 5.704\times10^{-3} \end{bmatrix} \tag{7.2}$$

7.2.3 Kelvin Cell Lattice Elasticity Matrix

Table 7.4 shows the effective mechanical properties for the Kelvin cell lattice. The elastic modulus, shear modulus and Poisson's ratio is the same in all 3 principal directions due to the symmetries present in the Kelvin cell structure. The Poisson's ratio can be compared to an analytical solution derived without assumption of predominant deformation modes [68]. Equation 7.3 shows the analytical solution for circular cross sections. The analytical Poisson's ratio is 0.4925, equating to a relative error of 0.08% when compared to numerically determined values.

$$\nu_{Kelvin} = 0.5(\frac{r^2 - 3r^4}{r^2 + 3r^4}) \tag{7.3}$$

Table 7.4: Effective mechanical properties for Kelvin cell lattice.

E_{11}	E_{22}	E_{33}	G_{23}	G_{13}	G_{12}
4.41×10^{-5}	4.41×10^{-5}	4.41×10^{-5}	1.49×10^{-5}	1.49×10^{-5}	1.49×10^{-5}
ν_{21}	ν_{31}	ν_{12}	ν_{32}	ν_{13}	ν_{23}
0.492	0.492	0.492	0.492	0.492	0.492

Equation 7.4 shows the elasticity matrix for the Kelvin cell lattice.

$$E_{Kelvin} = \begin{bmatrix} 9.520 \times 10^{-4} & 9.224 \times 10^{-4} & 9.224 \times 10^{-4} & 0 & 0 & 0 \\ 9.224 \times 10^{-4} & 9.520 \times 10^{-4} & 9.224 \times 10^{-4} & 0 & 0 & 0 \\ 9.224 \times 10^{-4} & 9.224 \times 10^{-4} & 9.520 \times 10^{-4} & 0 & 0 & 0 \\ 0 & 0 & 0 & 1.488 \times 10^{-5} & 0 & 0 \\ 0 & 0 & 0 & 0 & 1.488 \times 10^{-5} & 0 \\ 0 & 0 & 0 & 0 & 0 & 1.488 \times 10^{-5} \end{bmatrix} \tag{7.4}$$

7.2.4 Cubic Continuum Results

Figure 7.8 shows the results of the 3D continuum model of the cubic lattice. Similar to the 2D square results, the unconstrained boundary condition does converges with one element, affected by increasing the numbers of elements. This is again due to the uniform strain field. The fully constrained boundary condition does converge with increasing number of elements.

Figure 7.9 shows the profile views of the continuum model with 4^3 elements. It clearly demonstrates that the profiles are not equal for the $x-y$, $z-x$, and $z-y$ planes. This is erroneous behaviour as the response should be equal due to the symmetry of the cubic structure, which can be confirmed using the discrete modelling results (see Section 6.4.1). See Section 9.2.2.3 for discussion.

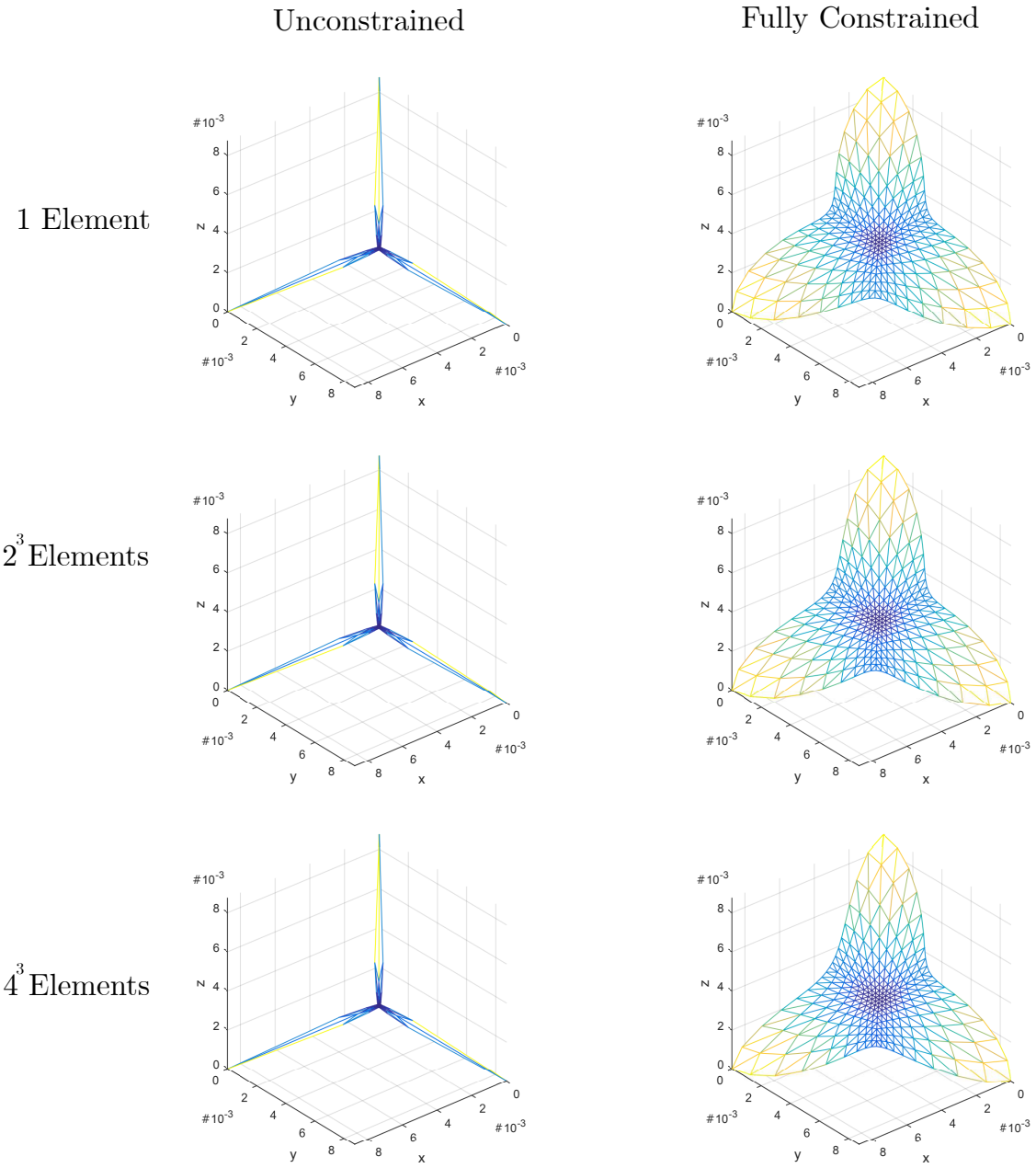

Figure 7.8: Continuum model of cubic lattice with increasing number of elements.

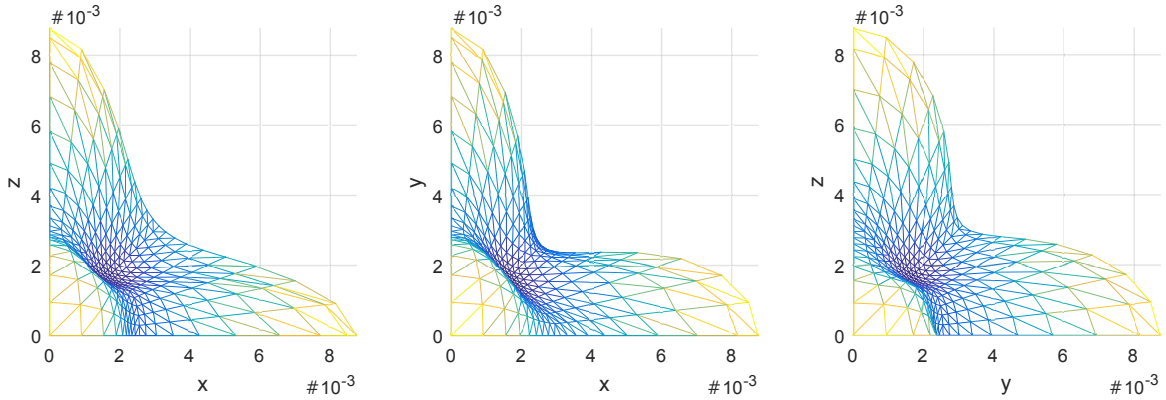

Figure 7.9: Profile views of the cubic fully constrained response with 4^3 elements.

7.2.5 Octet-Truss Continuum Results

Figure 7.10 shows the results of the 3D continuum model for the octet-truss lattice. The continuum model shows a similar response to the discrete model for both the unconstrained and fully constrained boundary conditions. The unconstrained response converges with a single element and is not affected by increasing mesh resolution, whereas the fully constrained does show convergence. The maximum deviation between different resolutions is 0.95% and 0.62% between 1 and 2^3 elements, and 2^3 and 4^3 elements.

The unconstrained behaviour of the octet-truss does not have the erroneous behaviour seen in the cubic results in Figure 7.9, i.e the profiles on orthogonal planes are identical.

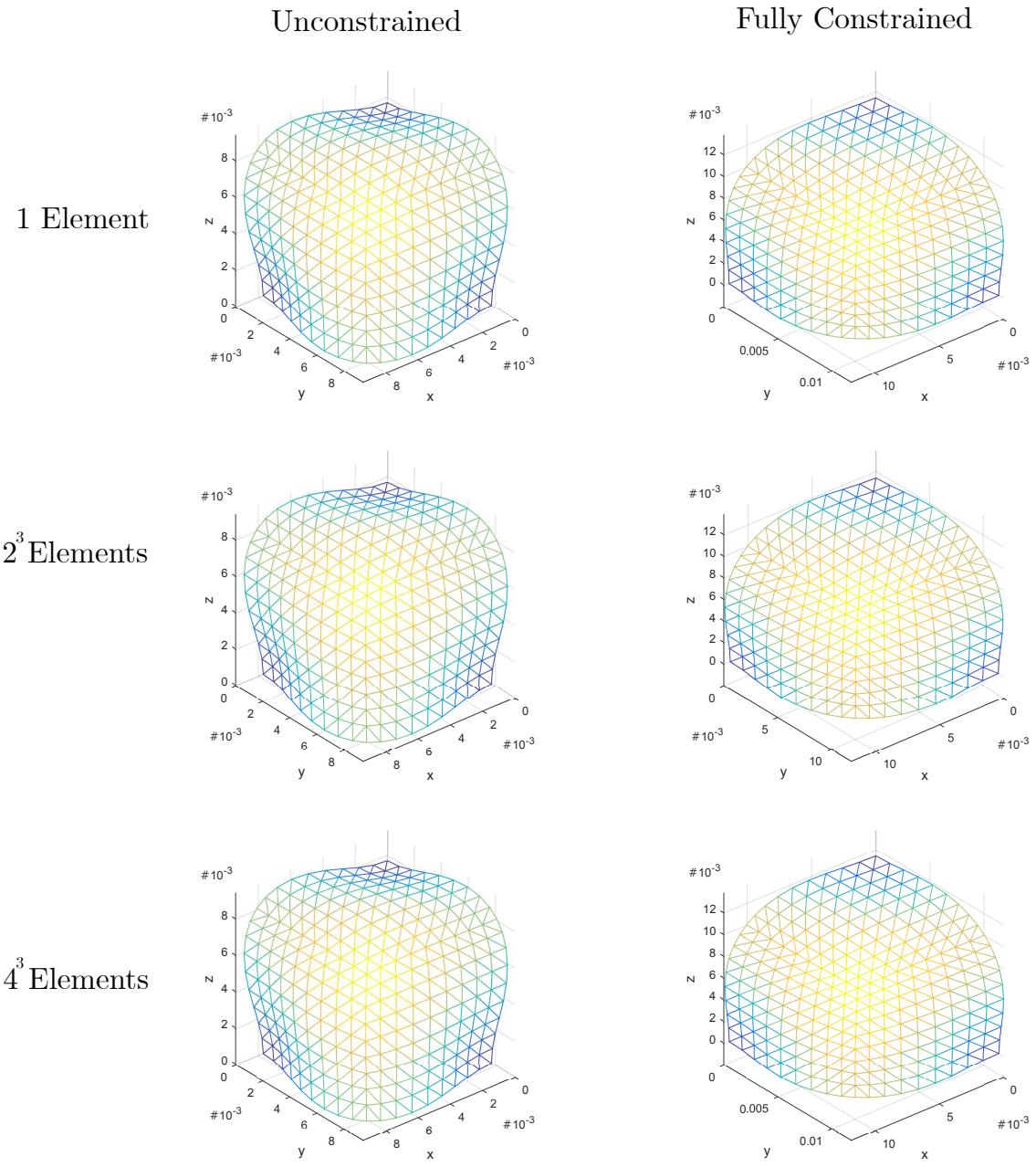

Figure 7.10: Continuum model of octet-truss lattice with increasing number of elements.

Table 7.5 shows the maximum and minimum relative effective elastic modulus for the octet-truss lattice using the continuum model with 4^3 elements. The continuum model shows similar degrees of anisotropy to the discrete model where the maximum stiffness is 1.77 and 1.33 times greater than the minimum for the unconstrained and fully constrained respectively.

The effect on the stiffness for the model that is laterally constrained is similar to the discrete model, where the fully constrained boundary condition has a relative effective elastic modulus 1.12 and 1.48 times greater than the unconstrained for the maximum and minimum values respectively.

Table 7.5: Minimum and maximum effective elastic moduli for octet-truss lattice using continuum model.

	Unconstrained	**Fully constrained**
Maximum	1.361×10^{-2}	1.521×10^{-2}
Minimum	7.672×10^{-3}	1.143×10^{-2}

Table 7.6 shows the difference between the continuum results for the octet-truss lattice and an analytical solution for bulk behaviour. The difference between the analytical solution and the numerically determined value is lower than when using the discrete model. However this is only because the number of cells in the lattice used to generate the elasticity matrix used in the continuum model was greater than the discrete model due to computational limitations.

Table 7.6: Comparison between analytical and numerically determined effective elastic moduli for octet-truss lattice using a continuum model.

Direction	**Numerical**	**Analytical**	**Difference (%)**
x, y, z	7.672×10^{-3}	7.405×10^{-3}	3.94
(1,1,1)	1.361×10^{-2}	1.333×10^{-2}	2.83

7.2.6 Kelvin cell Continuum Results

Figure 7.11 shows the results of the 3D continuum model of the Kelvin cell lattice with increasing number of elements. The continuum results show near perfect isotropy with both the unconstrained and fully constrained boundaries. Increasing the mesh resolution does not have an effect on the global properties. This is due to the uniform strain state induced by the Kelvin cell lattice.

As the response is isotropic, it does not have the erroneous behaviour seen in the cubic lattice when considering profiles at orthogonal planes (see Figure 7.9).

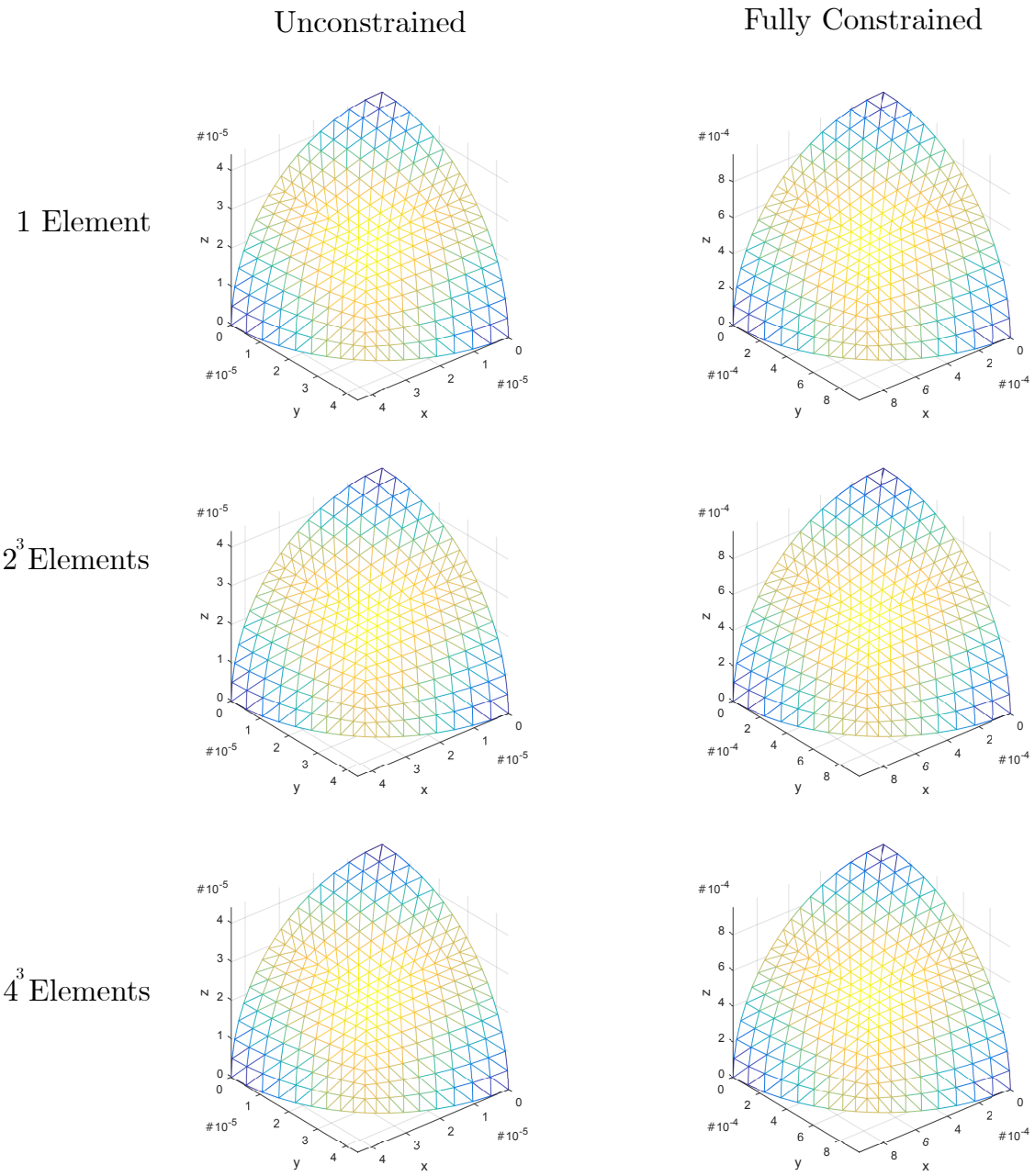

Figure 7.11: Continuum model of Kelvin cell lattice with increasing number of elements.

Table 7.7 shows the minimum and maximum values for the relative effective modulus. The error compared to the analytical solution is 4.6%, which is lower than the discrete model due to the higher number of cells used to generate the elasticity matrix.

Table 7.7: Minimum and maximum effective elastic moduli for Kelvin cell lattice using continuum model.

	Unconstrained	**Fully constrained**
Maximum	4.321×10^{-5}	9.732×10^{-4}
Minimum	4.313×10^{-5}	9.731×10^{-4}

The fully constrained relative effective elastic modulus is 22.5 times greater than with no lateral constraints; this shows high agreement with the discrete model where the ratio is 22.2.

The fully constrained response does not show the local maxima when using the continuum modelling approach that is seen in the discrete model for the 2D hexagonal lattice and the 3D Kelvin cell lattice. As the geometry of the lattice is ignored in the continuum model the boundary effects are mitigated.

Chapter 8

Microstructural Indices Results

This chapter details the microstructural analysis of the three 3D lattices, performed in BoneJ [16]. The lattices are prepared for microstructural analysis using the method outlined in Chapter 5. Figure 8.1 shows the three lattices as 3D skinned models with volume. The 2D lattices are not analysed as BoneJ requires a volumetric test specimens. The number of unit cells were chosen per lattice to keep the overall dimensions similar to ensure a common voxel size for all lattices. Table 8.1 shows the size of the resulting voxel dimension for each lattice, with the number of slices and the overall lattice geometry.

Table 8.1: Size of lattices, and resulting voxel resolution, used in determining microstructural indices.

	Cubic	**Octet-Truss**	**Kelvin Cell**
Number of cells	10	7	5
Size	10	9.90	14.14
Number of layers	500	494	707
Voxel Dimension	2.000×10^{-2}	2.003×10^{-2}	2.003×10^{-2}

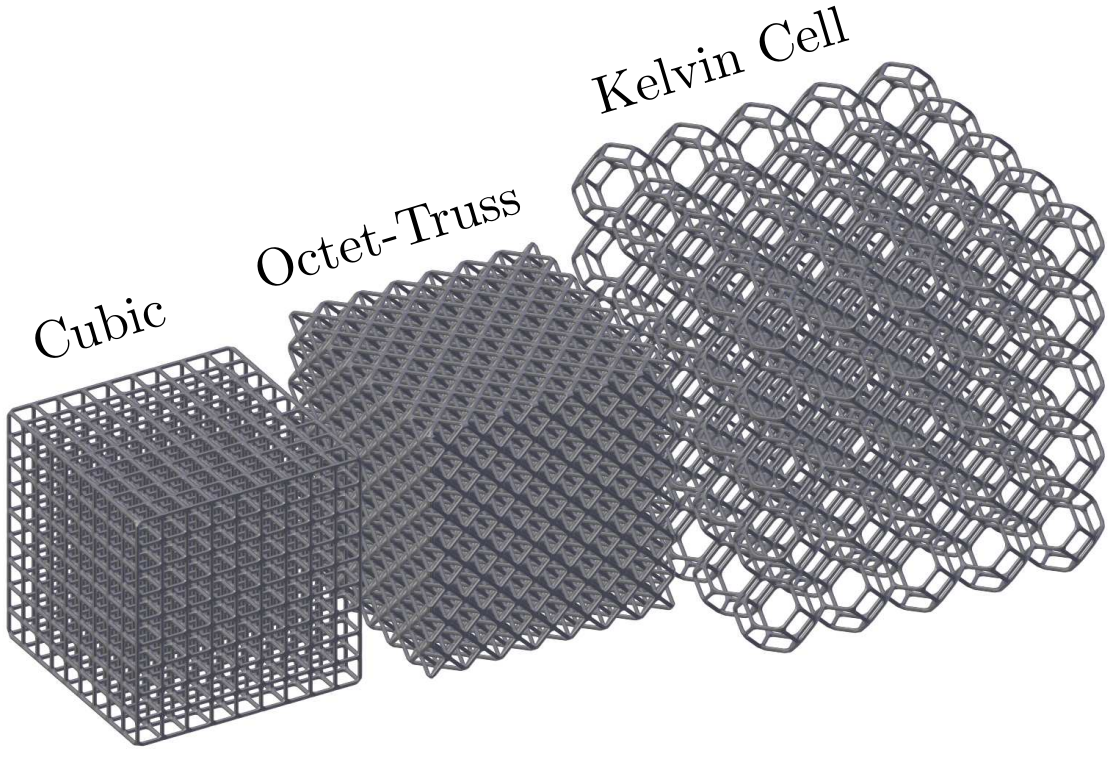

Figure 8.1: Three skinned 3D lattices.

8.1 Analyse Skeleton Tool

BoneJ contains a tool called Analyse Skeleton which takes a skeletonised stack of the lattice, created using the Skeletonise 3D tool, and outputs the number of branches (trabeculae) and junctions (nodes) in the lattice, along with information regarding the length of the branches. Table 8.2 shows the full output of the Analyse Skeleton tool for the three 3D lattices.

Table 8.2: Full output of Analyse Skeleton BoneJ tool.

	Cubic	**Octet - Truss**	**Kelvin cell**
Number of Branches	3097	8844	4472
Number of Junctions	998	1710	2057
Number of End-point Voxels	802	0	2070
Number of Junction Voxels	5502	17756	5040
Number of Slab Voxels	136853	284607	117874
Average Branch Length (pixels)	48.36	48.55	38.59
Number of Triple Points	8	20	1613
Number of Quadruple Points	94	12	314
Maximum Branch Length (pixels)	112.17	57.33	406.06
Longest Shortest Path (pixels)	1554.87	1053.94	4059.75

The number of branches and junctions, along with the average branch length, can be trivially found from the finite element mesh as the number of elements, nodes and the element length. Table 8.3 shows the comparison between the values from the finite element meshes with the calculated values from BoneJ. Where, elements are equivalent to branches, nodes are equivalent to junctions and lenght is equivalent to average length.x

Table 8.3: Difference between the results from Analyse Skeleton and the information captured directly from the finite element meshes.

		Cubic	**Octet - Truss**	**Kelvin cell**
Elements	Mesh	2700	8820	3300
	Error (%)	14.70	0.27	35.52
Nodes	Mesh	1000	1688	1800
	Error (%)	0.20	1.30	14.28
Length	Mesh	0.97	0.97	0.77
	Error (%)	3.27	2.89	22.81

The error in results from Analyse Skeleton likely originate during the skeletonisation, where elements are broken up into multiple pieces. Figure 8.2 shows a comparison between the skeletonised and the original stack. The artifacting is greatest for the Kelvin cell lattice, which corresponds to the lattice with the highest error.

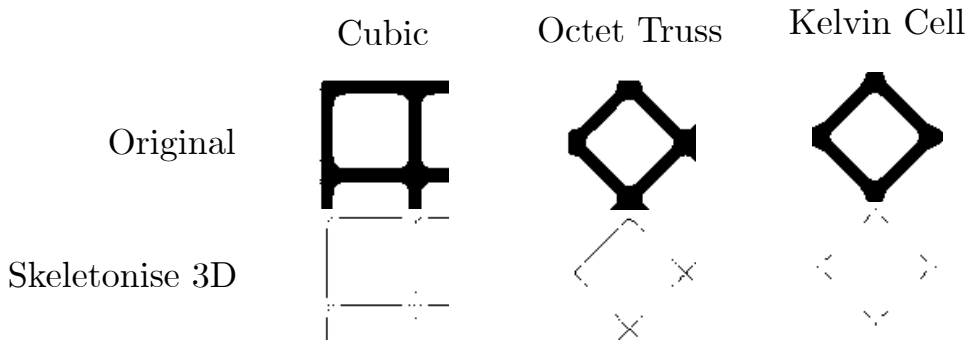

Figure 8.2: Zoomed in view of Skeletonise 3D artifacting.

8.2 Anisotropy

The mean intercept length is calculated using the default settings in BoneJ. The calculation runs a maximum of 2000 times or until the coefficient of variation of the degree of anisotropy is under a tolerance of 0.05. The calculation is run 10 times for each lattice to gain an understanding of the variation of the results.

The degree of anisotropy is a scalar measure of how elongated the fitted MIL ellipsoid is; See Chapter 5 and Equation 5.1 for more detail.

See Appendix D for the full output of all anisotropy trials.

8.2.1 Mean Intercept Length of Cubic Lattice

The mean intercept length analysis of the cubic lattice resulted in the average degree of anisotropy of 0.1315 with a standard deviation of 0.0217. Figure 8.3 and Table 8.4 show the results of the 10 calculations.

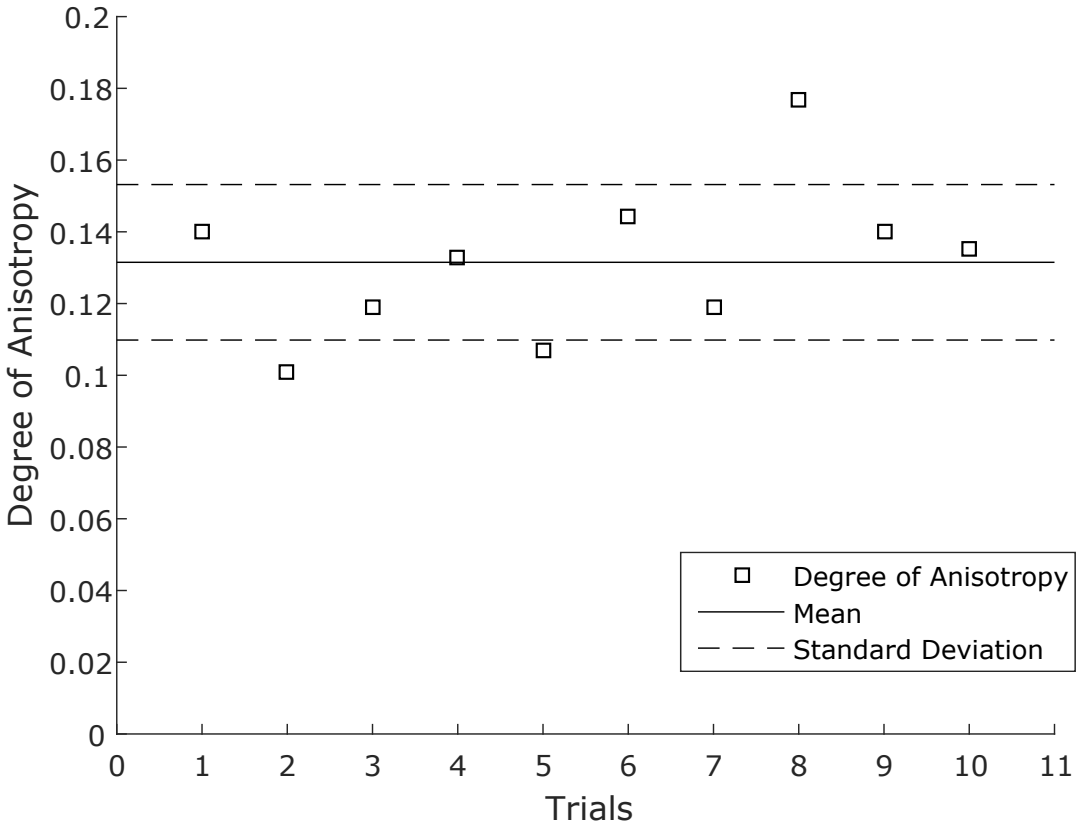

Figure 8.3: Degree of Anisotropy for cubic lattice.

Table 8.4: Degree of Anisotropy for cubic lattice.

Trial	1	2	3	4	5	6	7	8	9	10
DA	0.140	0.101	0.119	0.133	0.107	0.144	0.119	0.177	0.140	0.135

Figure 8.4 shows the mean intercept point cloud and its associated fitted ellipsoid. The fitted ellipse with the degree of anisotropy shown in Figure 8.3 and Table 8.4 demonstrates the mean intercept length analysis calculates a low degree of anisotropy for the cubic lattice.

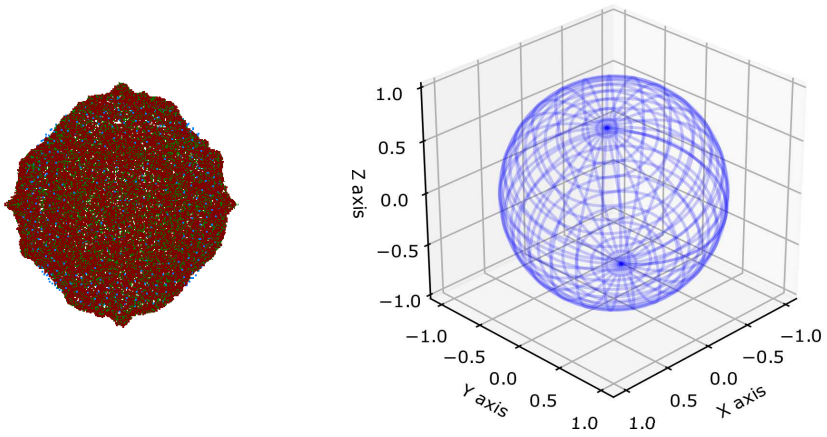

(a) (b)

Figure 8.4: Mean intercept length for cubic lattice. (a) Point cloud and (b) the associated fitted ellipsoid for trial 4.

8.2.2 Mean Intercept Length of Octet-Truss Lattice

The mean intercept length analysis of the octet-truss lattice showed an average degree of anisotropy of 0.1328 with a standard deviation of 0.0080. Figure 8.5 and Table 8.5 show the results of the 10 calculations. In all of the trials the coefficient of variation tolerance was met before the maximum recalculation limit.

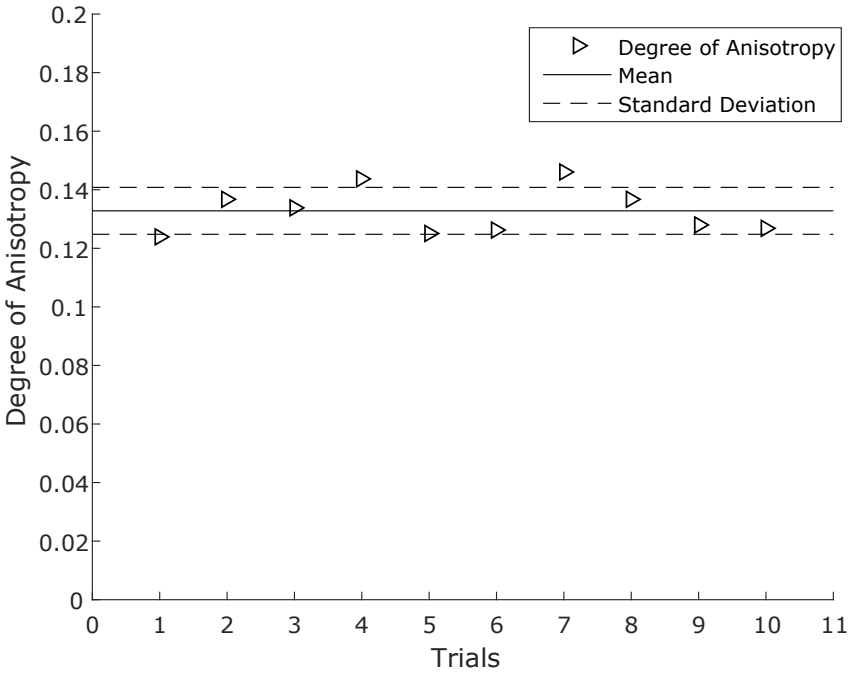

Figure 8.5: Degree of Anisotropy for Octet-truss lattice.

Table 8.5: Degree of Anisotropy for octet-truss lattice.

Trial	1	2	3	4	5	6	7	8	9	10
DA	0.124	0.137	0.134	0.144	0.125	0.126	0.146	0.137	0.128	0.127

Figure 8.6 shows the mean intercept length point cloud and the associated fitted ellipsoid. Figures 8.6 and 8.5 show the octet-truss lattice has a low degree of anisotropy, as calculated by the mean intercept length.

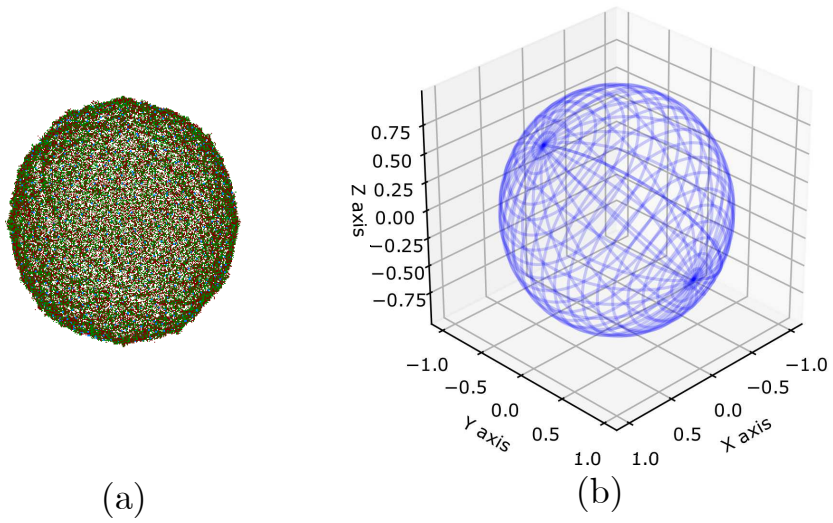

Figure 8.6: Mean intercept length for Octet-truss lattice. (a) Point cloud and (b) and the associated fitted ellipsoid for trial 7.

8.2.3 Mean Intercept Length of Kelvin Cell Lattice

The mean intercept length analysis of the Kelvin cell lattice showed an average degree of anisotropy of 0.1543 with a standard deviation of 0.0165. Figure 8.7 and Table 8.6 show the results of the 10 calculations.

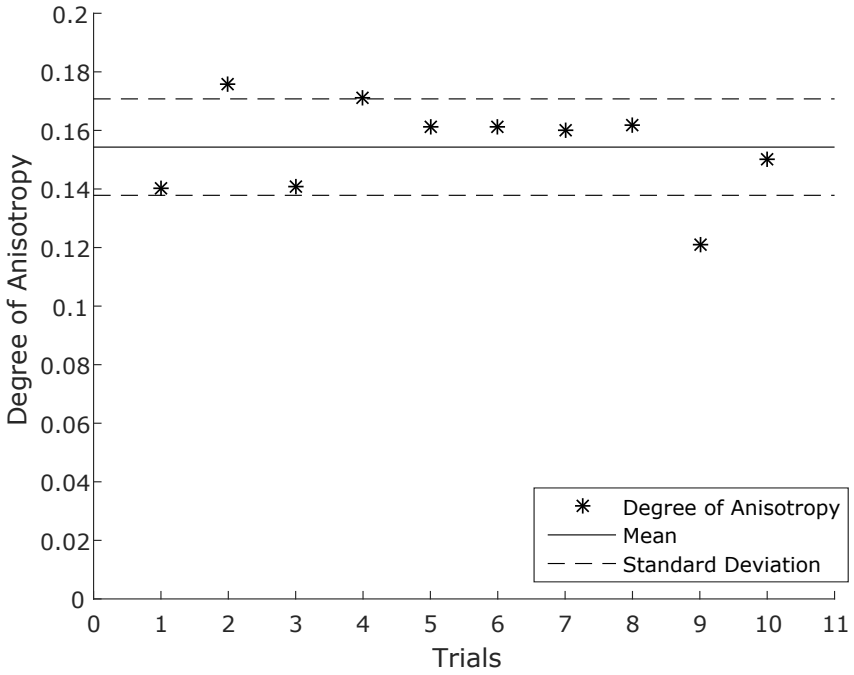

Figure 8.7: Degree of Anisotropy for Kelvin cell lattice.

Table 8.6: Degree of Anisotropy for Kelvin cell lattice.

Trial	1	2	3	4	5	6	7	8	9	10
DA	0.140	0.176	0.141	0.171	0.161	0.161	0.16	0.162	0.121	0.150

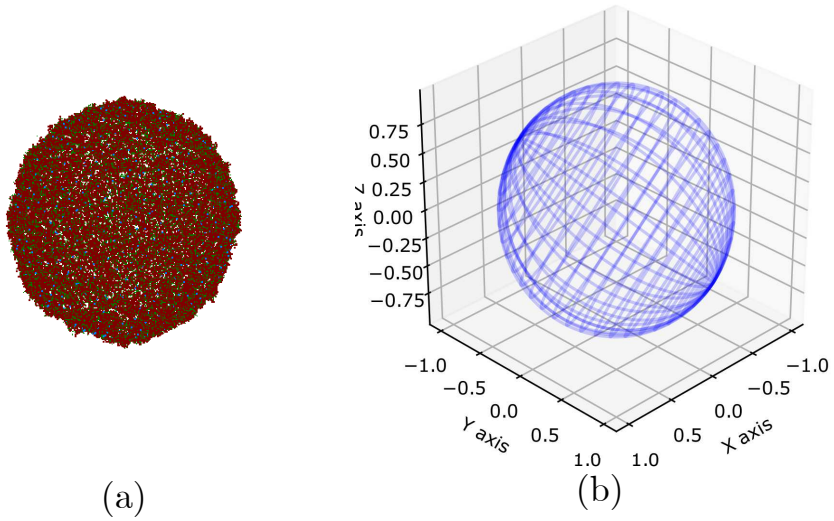

Figure 8.8: Mean intercept length for Kelvin cell lattice. (a) Point cloud and (b) and the associated fitted ellipsoid for trial 10.

8.2.4 Comparison of Mean Intercept Length

Figure 8.9 shows all the results for degree of anisotropy for all lattices.

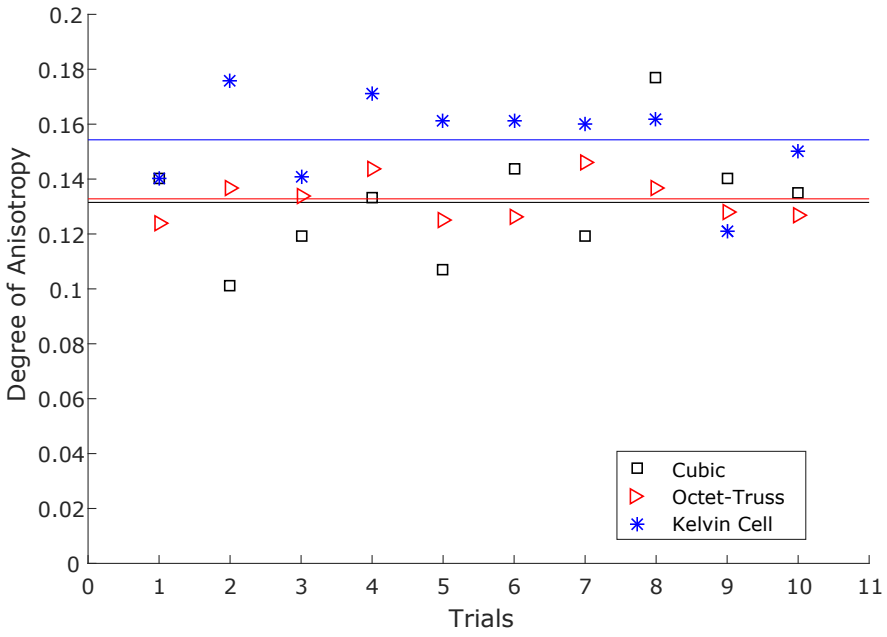

Figure 8.9: Degree of anisotropy for cubic, octet-truss and Kelvin cell lattices along with the mean value shown as a line in the corresponding colour.

An analysis of variance (ANOVA) was performed on the three sets to assess the similarities with an significance tolerance α of 0.05. Table 8.7 shows the result of the analysis of variance; there is a statistically significant difference between the groups as F is larger than F_{crit}.

Table 8.7: Analysis of variance for the degree of anisotropy for cubic, octet-truss and Kelvin cell lattices.

SUMMARY

Groups	*Average*	*Variance*
Cubic	0.1315	0.00047
Octet-truss	0.1328	6.42E-05
Kelvin cell	0.1543	0.000271

ANOVA

Source of Variation	*SS*	*df*	*MS*	*F*	*P-value*	*F crit*
Between Groups	0.003279	2	0.00164	6.109423	0.006475	3.354131

The same analysis was performed between the cubic and octet-truss lattices as their means were similar. Table 8.8 shows that there is no significant statistical variance between the cubic and octet-truss degree of anisotropy, as the F value is less than F_{crit}.

Table 8.8: Analysis of variance for the degree of anisotropy for cubic and octet-truss lattices.

Source of Variation	*SS*	*df*	*MS*	*F*	*P-value*	*F crit*
Between Groups	8.45E-06	1	8.45E-06	0.031647	0.860791	4.413873

Figure 8.9, along with Tables 8.7 and 8.8 demonstrate that the cubic and octet-truss lattices have the same degree of anisotropy, while the Kelvin cell has a higher degree of anisotropy as calculated by the mean intercept length method.

8.3 Connectivity

Table 8.9 shows the result of the connectivity analysis performed in BoneJ on the three 3D lattices investigated. It shows the Euler characteristic, along with the connectivity and connectivity density which is converted from pixels to metres using the voxel size shown in Table 8.1.

Table 8.9: Results of connectivity analysis of cubic, octet truss and Kelvin cell lattices performed in BoneJ.

	Cubic	**Octet-Truss**	**Kelvin Cell**
Euler characteristic	-1700	-7132	-1988
Connectivity	1701	7133	1989
Connectivity Density (pixel^{-3})	1.347×10^{-5}	5.86×10^{-5}	5.589×10^{-5}
Connectivity Density (m^{-3})	1.68	7.29	0.69

The octet-truss lattice has the highest connectivity density of 7.29 trabeculae per unit volume, which is 4 times greater than the cubic connectivity density and 10 times greater than the Kelvin cell connectivity density.

The connectivity density can be calculated directly, as the total number of elements and the total volume of the lattices are known from the finite element mesh. Table 8.10 shows the result of the exact connectivity density calculation.

Table 8.10: Exact calculation of connectivity density.

	Cubic	**Octet-Truss**	**Kelvin cell**
Elements	2700	8820	3300
Total Volume	1000	970.15	2828.43
Elements per unit volume	2.70	9.09	1.18

Table 8.10 demonstrates that the connectivity analysis in BoneJ underestimates the connectivity density for all lattices tested. The exact values are between 1.67 to 1.25 times greater than calculated using BoneJ. However, the general trends are still present with the octet-truss lattice having the greatest connectivity density, followed by the cubic lattice and the Kelvin cell lattice having the smallest connectivity density.

8.4 Thickness

Table 8.11 shows the result of the trabecular thickness and separation analysis performed in BoneJ. The results were converted from pixels to metres using the voxel size shown in Table 8.1.

Table 8.11: Results of trabecular thickness and separation analysis of cubic, octet truss and Kelvin cell lattices.

	Cubic		**Octet-Truss**		**Kelvin Cell**	
	pixels	**m**	**pixels**	**m**	**pixels**	**m**
Tb.Th Mean	6.47	1.295×10^{-1}	5.72	1.145×10^{-1}	5.527	1.106×10^{-1}
Tb.Th Std Dev	1.87	3.732×10^{-2}	1.89	3.792×10^{-2}	1.361	2.722×10^{-2}
Tb.Th Max	11.31	2.263×10^{-1}	11.66	2.336×10^{-1}	8.718	1.743×10^{-1}
Tb.Sp Mean	69.39	1.387×10^{0}	38.21	7.653×10^{-1}	141.773	2.835×10^{0}
Tb.Sp Std Dev	7.83	1.565×10^{-1}	8.48	1.699×10^{-1}	7.209	1.442×10^{-1}
Tb.Sp Max	72.14	1.442×10^{0}	50.16	1.005×10^{-0}	143.792	2.876×10^{0}

The mean thickness calculated using BoneJ overestimates the element thickness from the finite element mesh (which is 0.1 m). This is due to the method used in generating the skinned 3D meshes in Blender, which results in a local thickening at the nodes. Figure 8.10 demonstrates the local thickening at the nodes of the mesh.

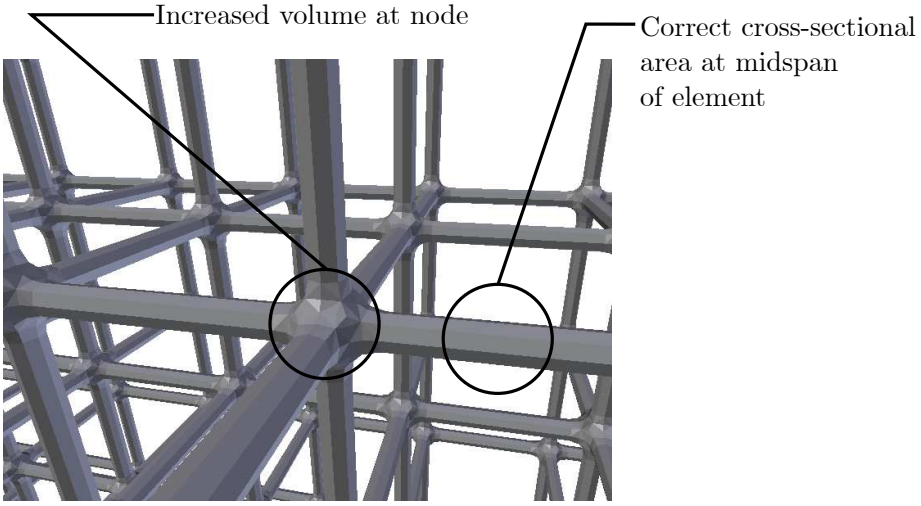

Figure 8.10: Perspective render of 3D skinned model of cubic lattice showing the increased volume at the nodes.

8.5 Volume Fraction

Table 8.12 shows the results of the volume fraction analysis performed in BoneJ for cubic, octet-truss and Kelvin cell lattices.

Table 8.12: Volume fraction analysis performed in BoneJ for cubic, octet-truss and Kelvin cell lattices.

	Cubic	**Octet-Truss**	**Kelvin Cell**
BV (pixels)	1528679	8081571	3471941
TV(pixels)	56622720	117124217	347194100
BV/TV	0.027	0.069	0.010

Table 8.13 shows the analytical solutions for the relative density of the cubic, octet-truss and Kelvin cell lattice [6, 59], along with the associated errors.

The analytically solutions for the Kelvin cell and cubic lattice are for square cross sections [6], as analytical solutions for circular cross sections are not apparent in literature.

Table 8.13: Analytical solutions of relative density for cubic, octet-truss and Kelvin cell lattices.

Lattice	**Relative Density**	**Value**	**Error (%)**
Cubic	$3\frac{d^2}{l^2}$	0.030	10
Octet-truss	$6\sqrt{2}\pi(\frac{r}{l})^2$	0.066	3.45
Kelvin cell	$1.06\frac{d^2}{l^2}$	0.011	5.66

Chapter 9

Discussion

This chapter includes a discussion on the mesh generation approach, followed by the modelling methodology. The advantages and disadvantages of both modelling approaches used are discussed, along with the results of the lattices investigated. The shortcomings of the continuum approach are outlined, along with potential explanations. The framework for the microstructural analysis is assessed, with discussion of the results and finally the comparison between the mechanical anisotropy and structural anisotropy is made and discussed.

9.1 Mesh Generation

The mesh generation technique described in Section 3.2 successfully created sufficiently large periodic lattice structures based on the geometry of a unit cell. This approach intuitively allowed for the creation of the three 3D periodic lattice structures, as the geometry is directly defined in the unit cell.

All of the lattices investigated had cubic unit cells. As such the mesh generation method does assume that the unit cells tile in a cubic manner. However, the methodology is easily extendable to account for unit cells that tile in other ways such as triangular or hexagonal tiling. To achieve this, the way in which the unit cells are translated to create larger structures and definition for which cells are neighbouring any particular cell need to be defined. The rest of the methodology does not consider the geometry of the unit cell and only looks at which nodes and elements are coincident.

By reducing the number of data reads and writes to the whole element and node list the time taken to add each new cell was not dependent on the size of the whole lattice. As such the time taken to add new cells plateaus as the size of the total lattice increases. This meant that the methodology performed well in generating everything from a single unit cell to a large periodic lattice structure.

The performance of the mesh generation was more dependant on the connectivity between neighbouring cells than the internal complexity of the unit cell. As such, care must be taken when defining the unit cell to limit the number of potential neighbours the cell has. For example, Figure 9.1 shows two variants of the unit cell for the octet-truss lattice. As the unit cell (b) does not have any corner nodes, it can only attach to 22 cells whilst cell (a) does have corner nodes and therefore it can attach to 26 cells.

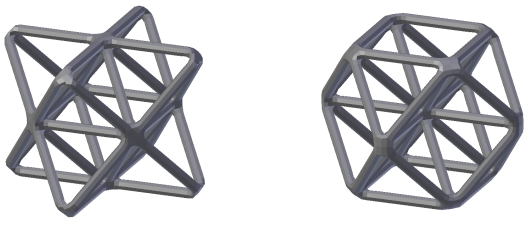

(a) (b)

Figure 9.1: Two variants for the unit cell of an octet-truss lattice.

9.2 Modelling Methodology

This section outlines the discussion of the two finite element modelling techniques employed in this research (see Chapters 3, 4). The results of each method are discussed, along with a comparison between the advantages and disadvantages

9.2.1 Discrete Modelling

The discrete modelling approach was successful overall, showing high agreement with literature. The methodology directly simulates the structure of the lattice which results in accurate representation of the response however there were two major drawbacks. The computational time was extensive to both simulate, process and generate all the jobs required to give a sufficiently high resolution view of mechanical anisotropy with large enough lattice size to converge to infinite or bulk behaviour. The other drawback was the difficulty in removing boundary effects with certain lattices as the geometry is directly simulated, causing the boundaries to be jagged.

9.2.1.1 2D Discrete Modelling Discussion

The response of the three 2D lattices investigated showed high agreement with the highest difference compared to analytical solutions being present with the hexagonal lattice. The square and triangular lattice both had a percentage difference compared to analytical solutions of under 1%.

The hexagonal lattice had an percentage difference of 2.2% compared to analytical solutions for the unconstrained case and showed local maxima in the fully constrained case which was due to the lattice being more sensitive to boundary effects than the other two. The percentage difference between numerical and analytical values for the fully constrained case was lower, with a maximum percentage difference of 0.42% ($0°\pm60°n$) as the numerical value oscillated higher and lower than the analytical value at different angles.

Despite the local error due to boundary sensitivity being evident in the hexagonal lattice. All the 2D lattices investigated show high agreement with analytical results in literature with regards to the overall macroscopic response and anisotropy.

9.2.1.2 3D Discrete Modelling Discussion

The discrete modelling method was successful in determining the macroscopic response of the 3D lattices investigated. The method was demonstrated to converge to bulk properties, and the convergence study was used to weigh the computational cost versus the degree of convergence to find an acceptable level of accuracy.

The 3D lattices were only loaded in compression with the unconstrained and fully constrained boundary conditions as boundary conditions in shear loading were particularly problematic to define in 3D and out of the scope of the project. However, the anisotropy of the shear response was not the focus and not an important factor in assessing the mean intercept length. The shear response was investigated only in the principal directions for use in the continuum modelling.

The cubic lattice was a perfect analogue for the 2D square behaviour, demonstrating a large discrepancy between the stiffness along the principal directions and any other direction with the unconstrained boundary conditions. The fully constrained boundary conditions showed no changes to the unconstrained case along the principal directions, with differences only occurring at the off angles. The largest discrepancy between the unconstrained and fully constrained boundary conditions was in the $(1, 1, 1)$ direction. The response for both loading conditions was symmetric about each of the principal directions as expected.

The octet-truss was the closest analogue to the 2D triangular lattice found in literature. The response is not isotropic, however it is substantially less anisotropic than the cubic and thus acts as a middle ground between the other two lattices in terms of anisotropy for the mean intercept length analysis.

The response of the octet-truss, in terms of the effect of lateral constraint was similar to the 2D triangular lattice. Both the octet-truss and the triangular lattice have a low Poisson's ratio (0.3298 and 0.3286 respectively) and do not have a large shift in predominant deformation (i.e axially dominant) mode when adding lateral constraints.

The Kelvin cell lattice was a good analogue for the 2D hexagonal lattice. The response was perfectly isotropic and lateral confinement had a very large effect, where lateral confinement increased the effective stiffness by 22.2 times.

The Kelvin cell also exhibited the same local maxima as the 2D hexagonal lattice when loaded using the fully constrained boundary conditions. This is also likely due to boundary effects. However the exact reason is unknown and could be researched further.

The Kelvin cell and 2D hexagonal lattices could be particularly sensitive to the boundary effects due to the relative size of the cell versus the element length being the greatest of the lattices investigated. This makes the effect of the jagged boundary caused by the boundary deletion cropping used more pronounced.

9.2.1.3 Convergence to Bulk Properties

The convergence to bulk properties was not of primary concern during the investigation of the 2D lattices; as the relatively low number of elements required was under computational limitations. However, as the 3D lattices require substantially greater number of elements the computational limitations were more of a concern; which lead to an investigation of how quickly the lattices converged to bulk behaviour, or behaviour assuming an infinite lattice.

The convergence studies on the three 3D lattices show that the responses do converge, and to known analytical solutions. The number of cells in the total lattice however are very high to only achieve reasonable difference between analytical and numerical solutions. With 27^3, or 19683, total cells the percentage difference is only 7.54%, 3.94% and 4.57% for the cubic, octet-truss and Kelvin cell lattices respectively.

The cubic lattice can be used as a case study as both an analytical solution (see Appendix C) for the bulk behaviour and for the behaviour of a lattice with any number of cells (assuming square lattice aspect ratio) are available. The number of cells as a function of the error is:

$$n_{cells} = \left(\sqrt{\frac{e}{100} + 1} - 1\right)^{-3}, \tag{9.1}$$

where n_{cells} is the total number of cells, e is the relative error as a percentage. Using Equation 9.1, it is shown that to get a relative error of under 1% the number of cells in the lattice would have to be greater than 8 060 000, or 200 cells along each side of a cubic sample.

The number of cells required to reach bulk behaviour raises concerns about the experimental testing methodology of removing small samples of trabecular bone and using the response to infer properties of the bone as a whole. This is has implications specifically if the inferred properties are used in a continuum modelling approach. The number of cells in any sample must be taken into consideration before any conclusions as to bulk properties can be drawn.

9.2.2 Continuum Modelling

The continuum modelling approach was successful in the majority of cases investigated, but suffered unacceptable error and failure with specific cases. The methodology treats the lattice structure as a solid material, abstracting the actual structure and calculating the response by means of an elasticity tensor which is transformed to arbitrary orientations. This method has far greater performance than the discrete method for two main reasons, namely as the structure is abstracted, individual elements for each beam are not required which results in far fewer elements and that the rotation is calculated using linear algebra vs. a rotation and complex cropping procedure. The continuum modelling approach also solves the jagged boundary problem the discrete modelling approach suffers from as the continuum elements can have any shape.

The discrete modelling is, however, still used in the generation of the elasticity tensor. There are a total of 6 discrete model simulations required to populate an orthotropic material (which was assumed for the lattices investigated). As far fewer discrete model simulations are required, a much higher resolution of discrete model can be used which results in lower error compared to the analytical bulk properties.

9.2.2.1 2D Continuum Modelling

The continuum modelling in 2D was successful for the square and triangular lattices. However, the hexagonal lattice showed erroneous results at non-zero rotations and when loaded under confined boundary conditions . Detailed discussion of errors in Section 9.2.2.3.

The square lattice results demonstrate that the continuum model can capture complex internal strain states induced in the square lattice when loaded with lateral confinement. Both the internal response and the macroscopic elastic modulus converge to the behaviour seen in the discrete model. The response of the unconstrained boundary conditions does not need to converge as the strain states are uniform, therefore only one element is required which results in a peak relative error of 0.6% compared to the discrete model. The fully constrained boundary conditions converge to under 5% error compared to the discrete model when 121 elements are used (11 elements along each edge), with the highest error being around 10° which corresponds to the least uniform internal displacement fields.

The continuum model of the triangular lattice performed well, with both the unconstrained and fully constrained boundary conditions converging instantly with one element. The errors were also very similar for both boundary conditions with a peak of 0.4% at a 30° orientation. This lattice is likely well conditioned for the continuum approach as it is isotropic with uniform internal displacement fields which can be captured by a single linear element.

The continuum model of the hexagonal lattice performed poorly. The response using the unconstrained response instantly converged with one element with a peak error of 1.4% compared to the discrete model. This peak error corresponded to a 90° rotation. This is similar to the results of the triangular lattices continuum model, due to the uniform displacement field of the hexagonal lattice. In contrast, the fully constrained boundary condition demonstrated that the continuum model can fail dramatically, with unacceptable errors ranging between 16.5% and 20.8%/. However, as the internal displacement field is also uniform, the response does converge with only one element (see Section 9.2.2.3 for discussion).

9.2.2.2 3D Continuum Modelling

The 3D continuum modelling was successful for the octet-truss and Kelvin cell lattices, however erroneous results were present in the cubic lattice response.

The cubic response with the unconstrained boundary conditions converged instantly with one element, similar to the 2D square unconstrained response. The fully constrained case did show convergence with increased number of elements, however it was demonstrated that the $x-z$,$z-y$ and $y-z$ profiles did not align. The reason for the lack of symmetry was not apparent.

The octet-truss lattice showed high agreement with both the discrete modelling results and the analytical solutions from literature. The response with unconstrained boundary conditions with a single element, resulted in a percentage difference of 3.94% in the principal directions and 2.83% in the $(1,1,1)$ direction compared to analytical solutions in literature. The fully constrained boundary conditions do induce internal non-uniform displacement fields in the octet-truss lattice, and therefore show convergence with increasing mesh resolution. The maximum deviation is 0.95% and 0.62% between 1 and 2^3 elements, and 2^3 and 4^3 elements respectively; the small deviation between different resolutions (that is decreasing with greater element numbers) show the response quickly converges.

The Kelvin cell lattice similarly showed high agreement with both discrete modelling results and the analytical solutions in literature. Unlike the discrete model which suffers from jagged boundaries, the continuum model shows a much higher degree of isotropy with both the fully constrained and unconstrained boundary conditions. The fully constrained behaviour also does not have the local maxima errors seen in the discrete model. The error compared to analytical is lower than the discrete (4.6%) which is due to a larger discrete lattice being able to be used to generate the elasticity tensor. The constraint effect was also similar to what was demonstrated in the discrete model with the fully constrained elastic modulus being 22.5 times greater than the unconstrained case (compared to 22.2 in the discrete model).

9.2.2.3 Problems Associated with Continuum Modelling

The error in the fully constrained behaviour of the hexagonal lattice illuminated a larger problem associated with using this continuum modelling approach of open cell lattice structures.

Table 9.1: Summary of the success of the continuum modelling approach

2D			**3D**		
	Unconstrained	Fully Constrained	Unconstrained	Fully Constrained	
Square	Success	Success	Cubic	Success	Failure
Triangular	Success	Success	Octet-truss	Success	Success
Hexagonal	Success	Failure	Kelvin cell	Success	Success

It is important to note that the error approaches zero for zero degree rotations for all of the cases investigated, even when erroneous behaviour was present. This demonstrates that the calculation of the elasticity tensor is not the source of the erroneous behavour. Therefore, it caused by the method of rotating the elasticity tensor for open cell lattice structures, and applying the tensor to the simulation of varying boundary conditions.

The problem arises from the continuum model being purely a function of the input elasticity tensor, without regard to the structure the elasticity tensor represents. Thus, structurally determined shifts in behaviour can not be captured with this method, and one important factor is the predominant deformation mode of the lattice.

The 2D hexagonal lattice has bending dominant deflection [6, 17], in both effective elastic modulus and effective shear modulus. However, this changes from bending dominant to axial deformation dominant when lateral confinement is added [17]. As the elements of the elasticity tensor used in continuum modelling are generated using unconstrained boundary conditions, the elasticity tensor does not consider or contain axial stiffness components. Thus, when the lateral confinement is added in the fully constrained case the increase in stiffness in only due to the Poisson effect and ignores the shift in predominant deformation mode.

This problem does not arise in the triangular lattice as the axial dominant deformation mode does not transition based on orientation or lateral confinement.

The problem is also not associated with the square lattice, which does have a shift in predominant deformation mode based on orientation of the lattice. The square lattice is fully axially dominant in the 0° and 90° degree orientations where the upright columns take all of the load. However at 45° degrees the lattice has bending dominant deformation. The continuum model manages to capture this behaviour well, considering the error with the fully confined boundary conditions has local minima at 0°,45° and 90°. This is captured as the elasticity tensor is defined using multiple elements; the effective direct stiffness captures the axially dominant behaviour and the effective shear modulus captures the bending dominant behaviour.

It is important to note that the square would fail as the hexagonal lattice did if the shift in predominant deformation mode was caused by a change in boundary conditions, as the elasticity tensor is not impacted by the boundary conditions applied to the finite element stiffness matrix.

Surprisingly the Kelvin cell did not fail similarly to the hexagonal lattice. It was assumed that the predominant deformation mode is in bending in the unconstrained case however literature is not clear on the predominant deformation mode. Similarly, as there is little to no investigation of lateral confinement in literature the predominant deformation mode in the fully constrained case is unknown. Thorough analytical work on 3D lattices with lateral confinement is required.

The error could be mitigated by regenerating the elasticity tensor for different boundary conditions. This would require running computationally expensive discrete models for any investigated confinement. As the purpose of investigating continuum models was to reduce computational cost, this would indicate a failure of the method.

9.3 Microstructural Analysis Results

The methodology described in Chapter 3 was successful in determining a wide range of microstructural indices. The analysis was performed on prepared image stacks for each 3D lattice using BoneJ [16].

9.3.1 Generating Image Stacks

The generation of the image stacks from a finite element mesh was successful; the methodology involved using the Python module of Blender (an open source and free 3D modelling software suite) to generate a skinned model with correctly specified radii of the elements. The 3D skinned model is saved as an .STL file, which is then sliced into images representing slices through the sample.

The disadvantages of the methodology were that the skinning of the finite element model in Blender results in increased volume at the nodes (see Section 8.4), which would have a definite effect on the results of the microstructural analysis. The other disadvantage was one of workflow. Generating the images required using multiple software suites and multiple steps which could be optimised by going directly to the image stack, forgoing the process of creating the skinned mesh in Blender (see Section 11.2 for recommendations).

The resulting image stacks were a successful representation of the input lattices, capturing the overall features of the geometry despite the errors associated with the nodes.

9.3.2 Results of Microstructural Analysis

BoneJ was used to analyse the skeletal information, anisotropy, connectivity, thickness and volume fraction of the lattices. The lattices used a different number of cells to ensure the size of each voxel was similar such that the images had the same resolution across the lattices. An advantage of the methodology employed in this research is that exact solutions for many of the indices can be calculated directly from the finite element mesh. In this way the accuracy of BoneJ and the skinning process can be assessed.

The analysis of the skeleton calculates a number of indices related to the structure of the lattice. The number of branches and junctions (elements and nodes, using nomenclature from finite element analysis), along with the average branch length could be directly compared to the input lattice by simply counting the number of elements and nodes. The analysis overestimated the number of branches in the sample for all lattices and underestimated the branch length. The number of nodes showed no consistent error. The Kelvin cell had substantially higher errors than the other two lattices, which could be attributed to a higher degree of artifacting during the skeletonisation process.

The anisotropy analysis had no exact solution that could be calculated from the finite element mesh. The analysis is non-deterministic and therefore was performed 10 times such that statistical conclusions could be drawn between the results of the lattices. It was demonstrated that the cubic and octet-truss lattice results showed no statistically significant differences, while the Kelvin cell was significantly different. The Kelvin cell lattice had the highest degree of anisotropy, but all lattices had a low degree of anisotropy.

The connectivity analysis calculates the density of branches or elements in a sample. This can be directly calculated from the finite element model by dividing the total number of elements with the volume of the lattice. The connectivity density calculated by BoneJ was consistently lower than the exact calculations, by between 1.67 to 1.25 times. Despite this error, the analysis could still be used to show relative differences as the same trend is apparent comparing the connectivity density with BoneJ results as the exact results; that being in order of lowest density to highest is Kelvin cell, cubic and the octet-truss lattices.

The thickness analysis performed in BoneJ could be compared directly to the beam thickness specified in the finite element analysis. The BoneJ results overestimate the thickness of the trabeculae between 3% to 1% for the different lattices. This is likely due to the local increase in volume at the nodes as the trabecular thickness is quoted as an average trabecular thickness.

The volume fraction analysis calculates the BV/TV index, or the relative density. This would also suffer error due to the increased volume at the nodes. There was an analytical solution for the octet-truss with a circular cross section in literature [59], however the cubic and Kelvin cell lattice solutions used a square cross section and therefore the error would naturally be higher. The BoneJ results for relative density overestimated the octet-truss lattice, which is aligned with the error introduced by the increased volume at the nodes.

Overall, the BoneJ analysis of the microstructure showed a small error is present with all results; however the results can be still used to compare relative differences between lattices. The error is likely associated with the increased nodal volume, however that would not affect certain analyses; notably the mean intercept length.

9.4 Comparison Between Mechanical Anisotropy and Geometric Anisotropy

The mechanical anisotropy for the cubic, octet-truss and Kelvin cell lattices is shown in Chapters 6 and 7 using two different approaches. It was demonstrated that the cubic lattice is highly anisotropic; the octet-truss lattice has a lesser degree of anisotropy and the Kelvin cell lattice was isotropic.

Chapter 8 showed the results of the microstructural analysis of the three 3D lattices investigated. The anisotropy analysis used the mean intercept length method to calculate the degree of anisotropy. The mean intercept length analysis showed low degrees of anisotropy for all lattices investigated. There was no significant statistical difference between the degree of anisotropy calculated for the cubic and octet-truss lattices, both with a low degree of anisotropy. The degree of anisotropy calculated for the Kelvin cell was slightly higher than the other two lattices, despite being the only purely isotropic 3D lattice investigated.

As a measure of mechanical anisotropy, a similar approach can be used such that the results of the direct calculation of anisotropy can be compared to the degree of anisotropy calculated using the mean-intercept analysis. Equation 9.2 defines the mechanical degree of anisotropy such that 0 corresponds to fully isotropic behaviour and 1 corresponds to highly anisotropic behaviour.

$$DA_{mechanical} = 1 - \frac{E_{min}}{E_{max}} \tag{9.2}$$

This scalar measure is not an exact equivalent to the mean intercept length degree of anisotropy as that is calculated using the lengths of the minor and major axes of the fitted ellipsoid, which are perpendicular whereas the minimum and maximum relative effective stiffness can be in any orientation.

Table 9.2 shows the degree of mechanical anistropy as calculated using Equation 9.2, along with the degree of geometric anisotropy calculated using the mean intercept length method. It clearly demonstrates that there is a large range of mechanical anisotropic behaviours, whilst the degree of anisotropy calculated by means of microstructural analysis shows little to no difference between the lattices investigated.

Table 9.2: Comparison between degree of anisotropy calculated from finite element modelling and via microstructural analysis.

	Degree of Anisotropy	
	Mechanical	**Mean intercept length**
Cubic	0.989131	0.1315
Octet-truss	0.447777	0.1328
Kelvin Cell	0.043	0.1543

The mechanical degree of anisotropy for the Kelvin cell is the lowest, however it is theoretically zero. The deviation is due to the discrete model not reaching full convergence to bulk behaviour yet. The mechanical degree of anisotropy does however correctly order the three lattices from most anisotropic to most isotropic (cubic, octet-truss and Kelvin cell).

Furthermore, this demonstrates that the lattice with the lowest degree of mechanical anisotropy, the Kelvin cell, has the highest degree of microstructural anisotropy. The cubic and octet-truss lattices have vastly different mechanical responses, with the mechanical degree of anisotropy for the cubic being more than double that of the octet-truss; while the degree of anisotropy calculated using the mean intercept length shows no significant statistical difference.

Even if the mean intercept length analysis could capture the anisotropy, the cubic lattice's anisotropy is highly irregular and could not be accurately fitted with an ellipsoid and thus a higher rank tensorial representation would be needed.

Chapter 10

Conclusions

A framework for generating lattices; calculating their macroscopic response using finite element analysis, solved in LS-DYNA, with focus on anisotropy and determining the microstructural indices associated with the lattices was developed using mainly free and open source software suites. The mechanical response was validated using analytical solutions from literature for the mechanical response in certain directions.

The method developed for generating periodic lattice structures for use in finite element analysis was robust and successful for a wide range of lattice sizes.

Two approaches to modelling the mechanical response of the lattices were used; a discrete model where the geometry of the structure is directly simulated and a continuum model. The discrete model was successful in determining the mechanical behaviours, however boundary effects were difficult to mitigate for certain lattices and the models had a high computational cost due to high resolutions required to reach convergence to bulk behaviour (see Chapter 6). The continuum model was not successful in reliably capturing the response. The boundary effects were mitigated and the method was more computationally efficient but abstracting away from the geometry introduced unacceptable errors, as it was unable to capture certain phenomena (see Chapter 7).

The anisotropic mechanical response of the lattices investigated were determined within acceptable error, compared to analytical solutions in literature. The effect of lateral confinement was dramatic; changing effective stiffness globally, changing the degree of anisotropy and having an effect on the predominant deformation modes.

The method developed for calculating microstructural indices was successful, however improvements can be made to the method of generating the required image stack from a finite element model. The anisotropy of the lattices were investigated using the mean intercept length method in BoneJ (see Chapter 8).

Correlations were assessed between the anisotropy calculated via microstructural analysis and simulation of the mechanical response (see Section 9.4). It was determined that no reasonable correlations were present between the known mechanical response of the lattices and the degree of anisotropy calculated using the mean intercept length method. There was large variation in the anisotropy of the lattices investigated ranging from highly anisotropic to purely isotropic. However the degree of anisotropy calculated from the microstructural analysis showed little to no variation for the three lattices, even predicting the highest degree of anisotropy for the only isotropic 3D lattice tested. Therefore a new means of correlating geometric anisotropy to mechanical anisotropy is required.

Chapter 11

Recommendations

11.1 Numerical Investigations

One of the aims of this research was quantifying the anisotropic macroscopic response of periodic lattices. However the framework developed could easily be used to investigate other lattices and phenomenon. The following are recommendations on work that could be done using the framework developed:

- A full and in depth investigation into the mechanical response of lattice structures. Particularly, an investigation into predominant deformation modes in lattices with fully constrained boundary conditions.
- Investigate correlations between all the microstructural indices calculated in this research with the periodic lattice responses.
- Investigate and mitigate the errors associated with continuum modelling of open cell lattice structures.
- Develop a more robust method of determining elasticity tensor for lattices that does not assume orthotropy for use with non-periodic lattices.
- Investigate the effects of geometric anisotropy by deforming periodic lattices. The periodic lattices can be trivially deformed by changing nodal positions by matrix transformation.
- Investigate the effects of non-periodicity in the microstructure by adding random offsets to the nodal positions with varying intensity and/or effects of random element or nodal deletions.
- Investigate the macroscopic response of non-periodic lattices and correlation to microstructural indices; by randomly generating lattice structures, such as Voronoi lattices.
- Extend the framework developed to beam and shell lattice models.
- Investigate the anisotropy of trabecular bone samples using the framework developed on beam and shell models of the bone samples and compare response to microstructural analysis

11.2 Direct Lattice Voxelization

The methodology used to generate the image stacks required to calculate the microstructural indices had disadvantages in both workflow and accuracy. Both of these disadvantages could be mitigated by developing a method to directly go from the finite element model to the image stack, instead of creating the skinned 3D model and processing the .STL file to create the stack.

One potential method is to use a line drawing algorithm in a 3D array, drawing lines of the correct thickness specified by the cross sectional area of the beams. Each slice of the 3D array could then be saved as a separate image. There are many efficient line drawing algorithms that could be used, for example to rasterise lines with different thickness's a modified Bresenham line algorithm could be used [69].

This approach should mitigate the local thickening of nodes; could trivially be used to work with lattices that have different beam properties and could be used, in conjunction with a planar flood fill algorithm, for models with beams and shell elements. The method could also be implemented in whatever development framework is used for the rest of the project, improving the workflow.

11.3 Confirm Microstructural Indices

The consistent errors present in the microstructural analysis, shown in Chapter 8, could be due to the calculation method employed in BoneJ or due to accuracy of the image stacks generated in this research, namely the local increase in volume at the nodes.

The local increase in volume at the nodes could be mitigated using a different method of generating the image stack representation of the lattices (see Section 11.2). Once a more robust and accurate method of creating the stacks is developed, the microstructural indices calculated using BoneJ could be verified by comparison with exact solutions to certain indices calculated from the finite element mesh.

Appendices

Appendix A

Software

Table A.1 contains a list of all software used. As a large portion of the project used free and open-source software, the version numbers used are very important in reproducing the work or further development as the software is subject to change.

Table A.1: Software used.

Software Name	Version Number	URL
Blender	2.78c	https://www.blender.org/
ImageJ	1.51h	https://imagej.nih.gov/ij/
BoneJ	1.4.2	http://bonej.org/
Python	3.6	https://www.python.org/

Appendix B

LS-DYNA Cards

B.1 Control Card

```
*KEYWORD
*TITLE
$#                                                                         title
LS-DYNA keyword deck by LS-PrePost
*CONTROL_IMPLICIT_AUTO
$#   iauto    iteopt    itewin     dtmin     dtmax     dtexp     kfail    kcycle
0        11         5       0.0       0.0       0.0         0         0
*CONTROL_IMPLICIT_GENERAL
$#  imflag       dt0    imform      nsbs       igs     cnstn      form    zero_v
1       1.0         2         1         2         0         0         0
*CONTROL_IMPLICIT_SOLUTION
$#  nsolvr    ilimit    maxref     dctol     ectol     rctol     lstol    abstol
1        11        15     0.001      0.011.00000E10       0.91.0000E-10
$#   dnorm    diverg     istif   nlprint    nlnorm   d3itctl     cpchk
2         1         1         0         2         0         0
$#  arcctl    arcdir    arclen    arcmth    arcdmp    arcpsi    arcalf    arctim
0         0       0.0         1         2         0         0         0
$#   lsmtd     lsdir      irad      srad      awgt      sred
1         2       0.0       0.0       0.0       0.0
*CONTROL_IMPLICIT_SOLVER
$#  lsolvr    lprint     negev     order      drcm    drcprm   autospc   autotol
4         2         2         0         4       0.0         1       0.0
$#  lcpack    mtxdmp
2         0
*CONTROL_TERMINATION
$#  endtim    endcyc     dtmin    endeng    endmas
1.0         0       0.0       0.01.000000E8
*DATABASE_NODFOR
$#      dt    binary      lcur     ioopt
1.0         1         0         1
*DATABASE_NODOUT
$#      dt    binary      lcur     ioopt   option1   option2
1.0         1         0         1       0.0         0
*DATABASE_NODOUT
$#      dt      lcdt      beam     npltc    psetid
0.01         0         0         0         0
$#   ioopt
0
*PART
$#                                                                         title
Beam
$#     pid     secid       mid     eosid      hgid      grav    adpopt      tmid
```

```
1         1         1         0         0         0         0         0
*PART
$#                                                                    title
beamBoudnary
$#     pid     secid       mid     eosid      hgid      grav    adpopt      tmid
2         2         1         0         0         0         0         0
*DEFINE_CURVE_TITLE
Load Curve
$#    lcid      sidr       sfa       sfo      offa      offo    dattyp     lcint
1         0       1.0       1.0       0.0       0.0         0         0
$#                a1                  o1
0.0                 0.0
1.0                 1.0
2.0                 1.0
*END
```

B.2 Material Property Card

```
*KEYWORD
*SECTION_BEAM_TITLE
Beam.2x.6
$#   secid    elform      shrf   qr/irid       cst     scoor       nsm
1        13       1.0          2         1       0.0       0.0
$#       a       iss       itt         j        sa       ist
0.0078544.90900E-64.90900E-6       0.0  0.007854       0.0
*MAT_ELASTIC_TITLE
Trabecula
$#     mid        ro         e        pr        da        db  not used
1    2500.02.00000E10       0.2       0.0       0.0         0
*SECTION_BEAM_TITLE
boundary element
$#   secid    elform      shrf   qr/irid       cst     scoor       nsm
2         4       0.0          2         1       0.0       0.0
$#     ts1       ts2       tt1       tt2
0.106066  0.106066       0.0       0.0
*END
```

B.3 Geometry Card

Below is an example of a geometry card. Only the first row of the element and node lists are shown for brevity.

```
*KEYWORD
*NODE
$#   nid               x               y               z      tc      rc
1065 8.000000000E+00-9.000000000E+00 0.000000000E+00       0       0
ect
*ELEMENT_BEAM
$#   eid     pid      n1      n2      n3     rt1     rr1     rt2     rr2   local
1       1     106     105     522       0       0       0       0       2
ect
*SET_NODE_LIST_TITLE
Dirichlet
$#     sid       da1       da2       da3       da4    solver
1       0.0       0.0       0.0       0.0MECH
$#    nid1      nid2      nid3      nid4      nid5      nid6      nid7      nid8
505       506       507       508       509       510       511       512
*SET_NODE_LIST_TITLE
Load
$#     sid       da1       da2       da3       da4    solver
2       0.0       0.0       0.0       0.0MECH
$#    nid1      nid2      nid3      nid4      nid5      nid6      nid7      nid8
105       106       107       108       109       110       111       112
*BOUNDARY_PRESCRIBED_MOTION_SET_ID
$#      id                                                                heading
0Prescribed Displacement
$#    nsid       dof       vad      lcid        sf       vid     death     birth
2          2         2         1-1.000E-01         01.00000E28       0.0
*DATABASE_NODAL_FORCE_GROUP
$#    nsid       cid
1         0
*INCLUDE
C:/...................../control.k
*INCLUDE
:/...................../materialProp.k
*BOUNDARY_SPC_SET_ID
$#      id
0Unconstraiend BC
$#    nsid       cid      dofx      dofy      dofz     dofrx     dofry     dofrz
1         0         0         1         1         1         1         1
*SET_NODE_LIST_TITLE
Stablising boundary condition
$#     sid       da1       da2       da3       da4    solver
3       0.0       0.0       0.0       0.0MECH
$#    nid1      nid2      nid3      nid4      nid5      nid6      nid7      nid8
392         0         0         0         0         0         0         0
*END
```

Appendix C

Derivation of Cubic Effective Modulus

The effective modulus can be calculated in the principal directions by considering the axial deflection of the vertical struts.

- F_1 is the force on one column
- F_T is the total force
- $n_{x,y,z}$ is the number of struts in the respective direction
- n_T is the total number of vertical struts
- l_{el} is the length of an individual element
- l_T is the length of a side of the whole lattice: $l_T = (n_1 - 1)l_{el}$
- δ is the prescribed displacement
- A_{cs} is the cross sectional area of the elements
- A_T is the projected area of the lattice
- E_s is the Young's modulus of the element

The force on a single strut can be calculated using Hooke's law as follows:

$$\begin{aligned} \epsilon_1 &= \frac{\delta}{l_T} \\ \sigma_1 = E_s\epsilon_1 &= \frac{\delta E_s}{l_T} \\ F_1 = \sigma_y A_{cs} &= \frac{\delta E_s A_{cs}}{l_T} \end{aligned} \tag{C.1}$$

The total force is the summation of the force on each vertical strut.

$$F_T = \sum_{n=1}^{n_T} nF_1 = n_T F_1 = \frac{n_T \delta E_s A_{cs}}{l_T} \tag{C.2}$$

The total stress over the lattice is defined as:

$$\sigma_T = \frac{F_T}{A_T} = \frac{n_T \delta E_s A_{cs}}{A_T l_T} \tag{C.3}$$

The total strain is equal to the strain of one strut:

$$\epsilon_T = \epsilon_1 = \frac{\delta}{l_T} \tag{C.4}$$

The total stiffness of the lattice is then given by Hooke's law:

$$E_T = \frac{\sigma_T}{\epsilon_T} = \frac{\frac{n_T \delta E_s A_{cs}}{A_T l_T}}{\frac{\delta}{l_T}} = \frac{n_T E_s A_{cs}}{A_T} \tag{C.5}$$

Diving by the Young's modulus of the element material yields the relative Young's modulus of the lattice.

$$E_T = \frac{n_T A_{cs}}{A_T} \tag{C.6}$$

Expanding out and subsituting $l_T = (n_1 - 1)l_{el}$ and $n_T = \sqrt{(}n_1)$ yields the following:

$$E_T = \frac{A_{cs} n_T}{l_{el}(\sqrt{n_T} - 1)^2} \tag{C.7}$$

C.1 Bulk Property

Equation (C.7) is a function of the number of columns, or is a function of the geometry of the lattice itself. To calculate the behaviour of an infinite lattice, the limit of the function must be calculated.

As the limit of the following function is:

$$\lim_{x \to \infty^+} \frac{x}{(\sqrt{x} - 1)^2} = 1 \tag{C.8}$$

The relative effective stiffness can be written, with the number of columns tending to infinity, as:

$$E_{bulk} = \lim_{n_T \to \infty^+} \frac{A_{cs} n_T}{l_{el}(\sqrt{n_T} - 1)^2} = \frac{A_T}{l_{el}} (\lim_{n_T \to \infty^+} \frac{n_T}{(\sqrt{n_T} - 1)^2}) = \frac{A_T}{l_{el}} \tag{C.9}$$

Appendix D

Mean Intercept Length Data

D.1 Cubic Lattice

Table D.1: Cubic lattice anisotropy analysis performed in BoneJ; all trials (1/3).

Trial	Point Cloud	Convergence	*FabricTensor*
1	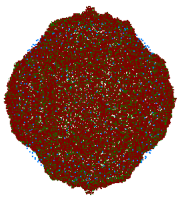	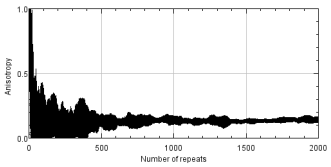	$\begin{bmatrix} -0.014 & 0.998 & -0.068 \\ -0.994 & -0.006 & 0.11 \\ 0.11 & 0.069 & 0.992 \end{bmatrix}$
2	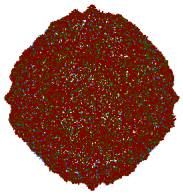	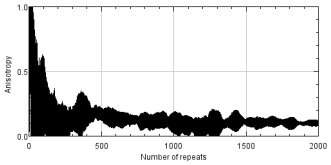	$\begin{bmatrix} 0.015 & 0.448 & -0.894 \\ -0.992 & 0.119 & 0.043 \\ -0.125 & -0.886 & -0.446 \end{bmatrix}$
3	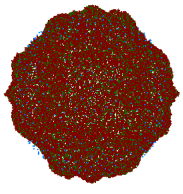	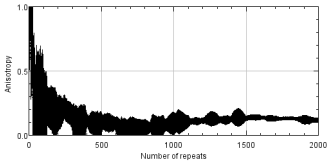	$\begin{bmatrix} -0.07 & 0.955 & -0.289 \\ -0.995 & -0.047 & 0.087 \\ 0.07 & 0.294 & 0.953 \end{bmatrix}$

Table D.2: Cubic lattice anisotropy analysis performed in BoneJ; all trials (2/3).

Trial	Point Cloud	Convergence	*FabricTensor*
4	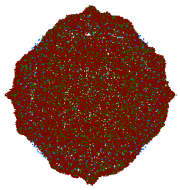	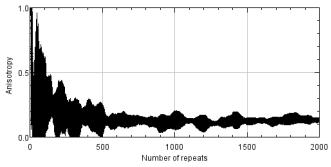	$\begin{bmatrix} 0.132 & -0.176 & -0.975 \\ -0.991 & -0.047 & -0.125 \\ 0.024 & -0.983 & 0.181 \end{bmatrix}$
5	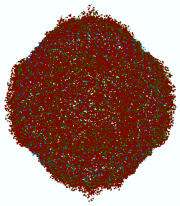	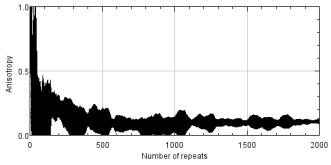	$\begin{bmatrix} -0.101 & -0.445 & -0.89 \\ -0.994 & -0.001 & 0.113 \\ 0.051 & -0.896 & 0.442 \end{bmatrix}$
6	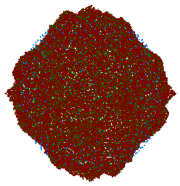	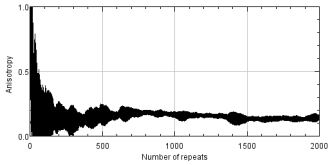	$\begin{bmatrix} 0.067 & 0.965 & -0.255 \\ 0.995 & -0.045 & 0.09 \\ 0.076 & -0.26 & -0.963 \end{bmatrix}$
7	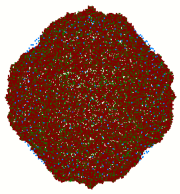	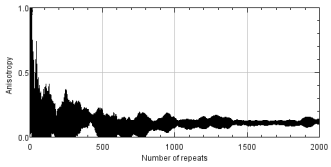	$\begin{bmatrix} 0.04 & 0.993 & -0.108 \\ -0.998 & 0.044 & 0.038 \\ 0.042 & 0.107 & 0.993 \end{bmatrix}$
8	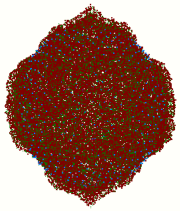	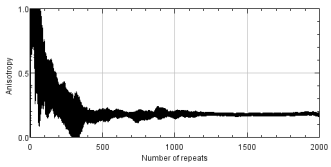	$\begin{bmatrix} 0.027 & -0.992 & 0.124 \\ 1.0 & 0.027 & -0.0005556 \\ -0.003 & 0.124 & 0.992 \end{bmatrix}$

Table D.3: Cubic lattice anisotropy analysis performed in BoneJ; all trials (3/3).

Trial	Point Cloud	Convergence	*FabricTensor*
9	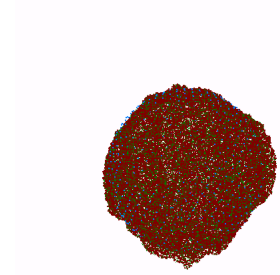	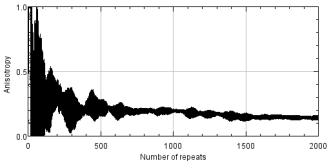	$\begin{bmatrix} 0.003 & 0.162 & 0.987 \\ 1.0 & -0.01 & -0.001 \\ -0.01 & -0.987 & 0.162 \end{bmatrix}$
10	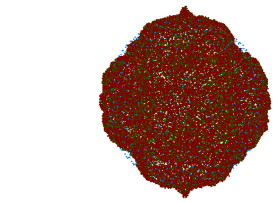	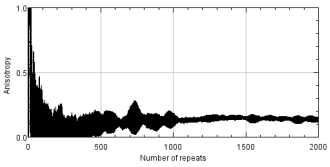	$\begin{bmatrix} 0.088 & 0.988 & -0.127 \\ 0.995 & -0.08 & 0.068 \\ 0.057 & -0.133 & -0.99 \end{bmatrix}$

D.2 Octet-Truss lattice

Table D.4: Octet-truss anisotropy analysis performed in BoneJ; all trials (1/3).

Trial	Point Cloud	Convergence	*FabricTensor*
1	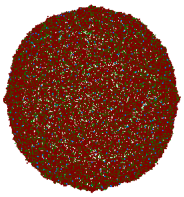	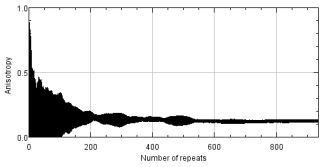	$\begin{bmatrix} -0.069 & -0.461 & -0.885 \\ -0.997 & 0.004 & 0.075 \\ 0.031 & -0.888 & 0.459 \end{bmatrix}$
2	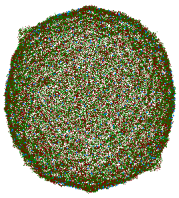	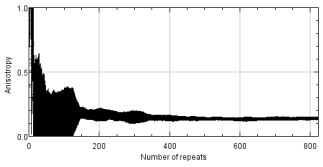	$\begin{bmatrix} -0.046 & 0.717 & 0.695 \\ -0.999 & -0.034 & -0.031 \\ 0.001 & -0.696 & 0.718 \end{bmatrix}$
3	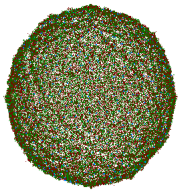	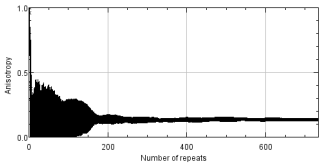	$\begin{bmatrix} 0.027 & 0.131 & -0.991 \\ -0.999 & -0.041 & -0.033 \\ 0.045 & -0.99 & -0.13 \end{bmatrix}$
4	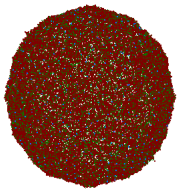	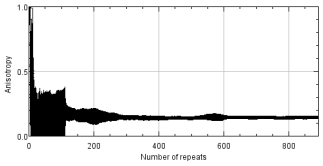	$\begin{bmatrix} 0.062 & -0.94 & 0.336 \\ 0.998 & 0.059 & -0.017 \\ -0.004 & 0.336 & 0.942 \end{bmatrix}$

Table D.5: Octet-truss anisotropy analysis performed in BoneJ; all trials (2/3).

Trial	Point Cloud	Convergence	*FabricTensor*
5	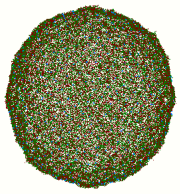	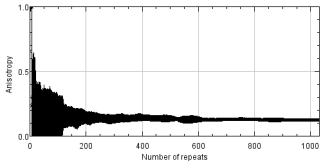	$\begin{bmatrix} -0.043 & -0.832 & 0.553 \\ 0.999 & -0.023 & 0.043 \\ -0.023 & 0.554 & 0.832 \end{bmatrix}$
6	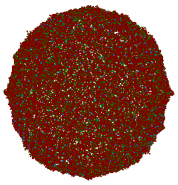	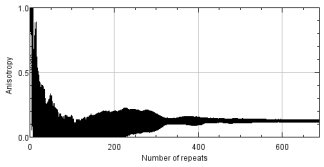	$\begin{bmatrix} 0.057 & 0.966 & 0.254 \\ -0.988 & 0.019 & 0.153 \\ 0.143 & -0.259 & 0.955 \end{bmatrix}$
7	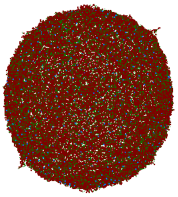	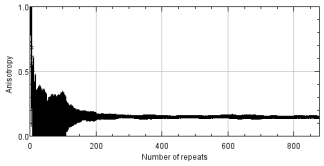	$\begin{bmatrix} 0.067 & 0.986 & -0.151 \\ -0.998 & 0.068 & -0.0008758 \\ 0.009 & 0.151 & 0.989 \end{bmatrix}$
8	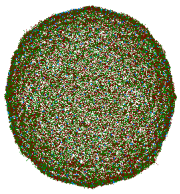	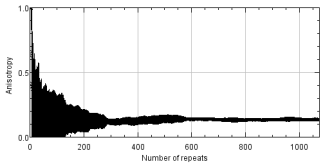	$\begin{bmatrix} 0.103 & -0.785 & -0.611 \\ 0.995 & 0.092 & 0.049 \\ 0.018 & -0.613 & 0.79 \end{bmatrix}$
9	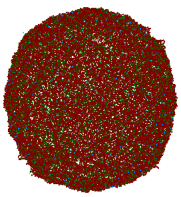	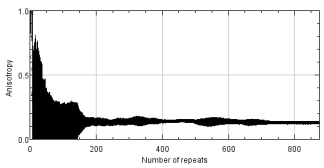	$\begin{bmatrix} -0.103 & 0.993 & 0.065 \\ -0.993 & -0.107 & 0.047 \\ 0.053 & -0.06 & 0.997 \end{bmatrix}$

Table D.6: Octet-truss anisotropy analysis performed in BoneJ; all trials (3/3).

Trial	Point Cloud	Convergence	*FabricTensor*
10	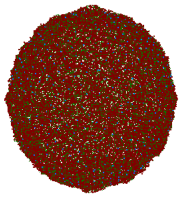	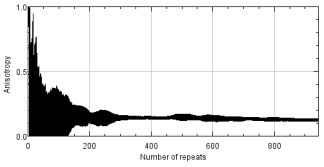	$\begin{bmatrix} 0.026 & -0.912 & -0.41 \\ -0.996 & -0.056 & 0.063 \\ -0.081 & 0.407 & -0.91 \end{bmatrix}$

D.3 Kelvin cell lattice

Table D.7: Kelvin cell lattice anisotropy analysis performed in BoneJ; all trials (1/3).

Trial	Point Cloud	Convergence	*FabricTensor*
1	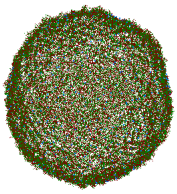	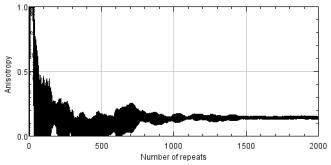	$\begin{bmatrix} -0.075 & -0.83 & -0.552 \\ 0.984 & -0.152 & 0.094 \\ -0.162 & -0.536 & 0.828 \end{bmatrix}$
2	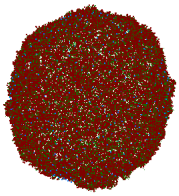	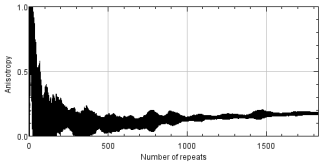	$\begin{bmatrix} 0.196 & 0.947 & -0.254 \\ -0.98 & 0.194 & -0.033 \\ 0.018 & 0.255 & 0.967 \end{bmatrix}$
3	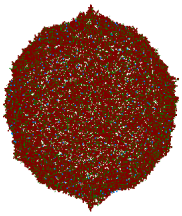	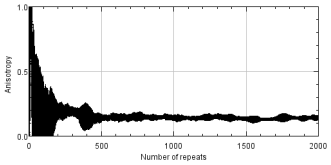	$\begin{bmatrix} -0.009 & -0.795 & -0.607 \\ -0.99 & -0.08 & 0.119 \\ -0.144 & 0.602 & -0.786 \end{bmatrix}$

Table D.8: Kelvin cell lattice anisotropy analysis performed in BoneJ; all trials (2/3).

Trial	Point Cloud	Convergence	*FabricTensor*
4	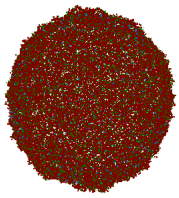	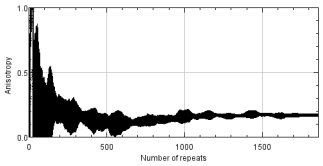	$\begin{bmatrix} -0.038 & -0.96 & -0.277 \\ 0.996 & -0.014 & -0.089 \\ 0.081 & -0.28 & 0.957 \end{bmatrix}$
5	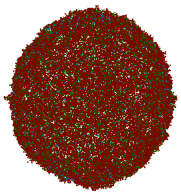	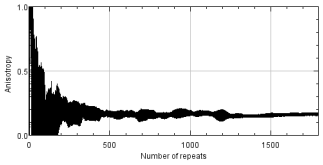	$\begin{bmatrix} -0.138 & -0.874 & -0.465 \\ 0.973 & -0.207 & 0.1 \\ -0.184 & -0.439 & 0.88 \end{bmatrix}$
6	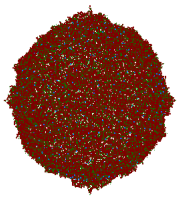	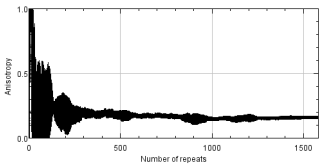	$\begin{bmatrix} 0.007 & 0.997 & 0.07 \\ -0.999 & 0.003 & 0.054 \\ 0.053 & -0.071 & 0.996 \end{bmatrix}$
7	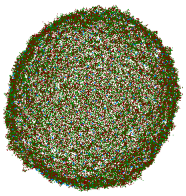	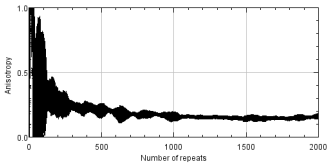	$\begin{bmatrix} 0.154 & 0.301 & -0.941 \\ -0.984 & 0.136 & -0.118 \\ -0.093 & -0.944 & -0.317 \end{bmatrix}$
8	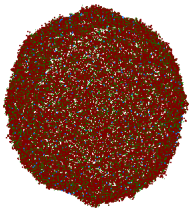	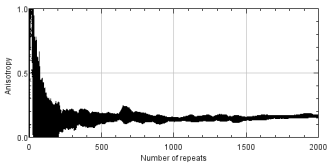	$\begin{bmatrix} 0.074 & -0.664 & 0.744 \\ 0.994 & 0.109 & -0.001 \\ -0.08 & 0.74 & 0.668 \end{bmatrix}$

Table D.9: Kelvin cell lattice anisotropy analysis performed in BoneJ; all trials (3/3).

Trial	Point Cloud	Convergence	*FabricTensor*
9	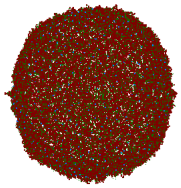	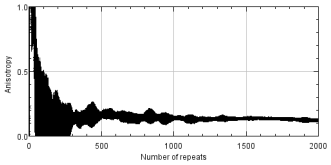	$\begin{bmatrix} 0.082 & 0.016 & -0.997 \\ -0.995 & 0.065 & -0.08 \\ -0.064 & -0.998 & -0.021 \end{bmatrix}$
10	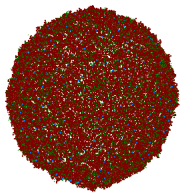	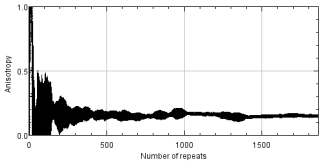	$\begin{bmatrix} -0.074 & -0.978 & 0.193 \\ 0.997 & -0.072 & 0.017 \\ -0.003 & 0.194 & 0.981 \end{bmatrix}$

References

[1] T. M. Keaveny and W. C. Hayes, "A 20-Year Perspective on the Mechanical Properties of Trabecular Bone," *Journal of Biomechanical Engineering*, vol. 115, no. 4B, p. 534, 1993. [Online]. Available: http://biomechanical.asmedigitalcollection.asme.org/article.aspx?articleid=1399632

[2] J. A. Kanis, L. J. Melton, C. Christiansen, C. C. Johnston, and N. Khaltaev, "The Diagnosis of Osteoporosis," *Journal of Bone and Mineral Research*, vol. 9, no. 8, pp. 1137–1141, 1995.

[3] O. Johnell and J. A. Kanis, "An estimate of the worldwide prevalence and disability associated with osteoporotic fractures," *Osteoporosis International*, vol. 17, no. 12, pp. 1726–1733, 2006.

[4] Kurtz SM, Roder C, Lau E, "International survey of primary and revision total hip replacement. Paper #365. Presented at the 56th Annual Meeting of the Orthopaedic Research Society. March 6-9, 2010. New Orleans." no. 365, p. 2007, 2007. [Online]. Available: http://www.healio.com/orthopedics/business-of-orthopedics/news/print/orthopedics-today/{%}7Bb5b93ea6-d765-491e-b6ce-a8df67c32494{%}7D/total-hip-arthroplasty-demand-rising-on-a-global-level

[5] A. Odén, E. V. McCloskey, J. A. Kanis, N. C. Harvey, and H. Johansson, "Burden of high fracture probability worldwide: secular increases 2010–2040," *Osteoporosis International*, vol. 26, no. 9, pp. 2243–2248, 2015.

[6] L. J. Gibson and M. F. Ashby, *Cellular solids: Structure and properties*, 2nd ed. Cambridge: Cambridge University Press, 1997.

[7] T. Hildebrand, A. Laib, R. Müller, J. Dequeker, and P. Rüegsegger, "Direct Three-Dimensional Morphometric Analysis of Human Cancellous Bone: Microstructural Data from Spine, Femur, Iliac Crest, and Calcaneus," *Journal of Bone and Mineral Research*, vol. 14, no. 7, pp. 1167–1174, 1999. [Online]. Available: http://doi.wiley.com/10.1359/jbmr.1999.14.7.1167{%}5Cnhttp://www.ncbi.nlm.nih.gov/pubmed/10404017

[8] M. Ding, A. Odgaard, C. C. Danielsen, and I. Hvid, "Mutual associations among microstructural, physical and mechanical properties of human cancellous bone," *The Journal of Bone and Joint Surgery*, vol. 84, no. 6, pp. 900–907, 2002. [Online]. Available: http://www.bjj.boneandjoint.org.uk/cgi/doi/10.1302/0301-620X.84B6.11994

[9] S. A. Goldstein, R. Goulet, and D. McCubbrey, "Measurement and significance of three-dimensional architecture to the mechanical integrity of trabecular bone," *Calcified Tissue International*, vol. 53, no. 1 Supplement, 1993.

[10] W. Q. Cui, Y. Y. Won, M. H. Baek, and K. K. Kim, "Contribution of Three-Dimensional Trabecular Bone Microstructure of the Proximal Femur to its Mechanical Properties as Assessed by Micro-Finite Element Analysis," *Key Engineering Materials*, vol. 321-323, no. March, pp. 278–281, 2006.

[11] D. Ulrich, B. Van Rietbergen, A. Laib, and P. Ruegsegger, "The ability of three-dimensional structural indices to reflect mechanical aspects of trabecular bone," *Bone*, vol. 25, no. 1, pp. 55–60, 1999.

[12] B. Helgason, E. Perilli, E. Schileo, F. Taddei, S. Brynjólfsson, and M. Viceconti, "Mathematical relationships between bone density and mechanical properties: A literature review," *Clinical Biomechanics*, vol. 23, no. 2, pp. 135–146, 2008.

[13] T. Keller and D. Spengler, "Predicting the compressive mechanical behavior of bone," *Journal of Biomechanics*, vol. 24, no. 9, p. 453, 1991.

[14] J. Galante, W. Rostoker, and R. D. Ray, "Physical properties of trabecular bone," *Calcified Tissue Research*, vol. 5, no. 1, pp. 236–246, 1970.

[15] M. Moesen, L. Cardoso, and S. C. Cowin, "A symmetry invariant formulation of the relationship between the elasticity tensor and the fabric tensor," *Mechanics of Materials*, vol. 54, no. October 2014, pp. 70–83, 2012. [Online]. Available: http://dx.doi.org/10.1016/j.mechmat.2012.07.004

[16] M. Doube, M. M. Klosowski, I. Arganda-Carreras, F. P. Cordelières, R. P. Dougherty, J. S. Jackson, B. Schmid, J. R. Hutchinson, and S. J. Shefelbine, "BoneJ: Free and extensible bone image analysis in ImageJ," *Bone*, vol. 47, no. 6, pp. 1076–1079, 2010.

[17] C. Lawrence, *Effective stiffness models of regualr honeycombs and implications for trabecular bone models*, University Of Cape Town, Final year project, 2016.

[18] D. Weaire, "Kelvin's ideal foam structure," *Journal of Physics: Conference Series*, vol. 158, 2009. [Online]. Available: http://iopscience.iop.org/article/10.1088/1742-6596/158/1/012005

[19] F. A. Sabet, A. Raeisi Najafi, E. Hamed, and I. Jasiuk, "Modelling of bone fracture and strength at different length scales: a review," *Interface Focus*, vol. 6, no. 1, p. 20150055, 2016. [Online]. Available: http://rsfs.royalsocietypublishing.org/lookup/doi/10.1098/rsfs.2015.0055

[20] M. Tzaphlidou, L. Rincón-Kohli, P. K. Zysset, J.-Y. Rho, M. J. Olszta, X. Cheng, S. S. Jee, R. Kumar, Y. Y. Kim, M. J. Kaufman, E. P. Douglas, and L. B. Gower, "Mechanical properties and the hierarchical structure of bone," *Biomechanics and Modeling in Mechanobiology*, vol. 58, no. 7-8, pp. 92–102, 2007.

[21] O. College, *Anatomy & Physiology*. Houston, Texas: Rice University, 2013.

[22] T.-C. Lee, R. L. Kashyap, and C.-N. Chu, "Building skeleton models via 3-d medial surface/axis thinning algorithms," *CVGIP: Graph. Models Image Process.*, vol. 56, no. 6, pp. 462–478, Nov. 1994. [Online]. Available: http://dx.doi.org/10.1006/cgip.1994.1042

[23] J. Toriwaki and T. Yonekura, "Euler Number and Connectivity Indexes of a Three Dimensional Digital Picture," *Forma*, vol. 17, no. 3, pp. 183–209, 2002. [Online]. Available: http://linkinghub.elsevier.com/retrieve/pii/8756328293902456{%}5Cnhttp://www.scipress.org/journals/forma/pdf/1703/17030183.pdf

[24] W. E. Lorensen and H. E. Cline, "Marching cubes: A high resolution 3D surface construction algorithm," *Proceedings of the 14th annual conference on Computer graphics and interactive techniques - SIGGRAPH '87*, vol. 21, no. 4, pp. 163–169, 1987. [Online]. Available: http://portal.acm.org/citation.cfm?doid=37401.37422

[25] M. Doube, "The ellipsoid factor for quantification of rods, plates, and intermediate forms in 3D geometries," *Frontiers in Endocrinology*, vol. 6, no. FEB, pp. 1–5, 2015.

[26] P. L. Salmon, C. Ohlsson, S. J. Shefelbine, and M. Doube, "Structure model index does not measure rods and plates in trabecular bone," *Frontiers in Endocrinology*, vol. 6, no. OCT, pp. 1–10, 2015.

[27] T. Hildebrand and P. Rüegsegger, "Quantification of bone microarchitecture with the structure model index," *Computer Methods in Biomechanics and Biomedical Engineering*, vol. 1, no. 1, pp. 15–23, 1997.

[28] R. Dougherty and K.-H. Kunzelmann, "Computing Local Thickness of 3D Structures with ImageJ," *Microscopy and Microanalysis*, vol. 13, no. S02, 2007. [Online]. Available: http://www.journals.cambridge.org/abstract{_}S1431927607074430

[29] J. Lotz, T. N. Gerhart, and W. Hayes, "Mechanical properties of trabecular bone from the proximal femur," vol. 14, pp. 107–14, 01 1990.

[30] R. Hodgskinson and J. D. Currey, "Young's modulus, density and material properties in cancellous bone over a large density range," *Journal of Materials Science: Materials in Medicine*, vol. 3, no. 5, pp. 377–381, 1992.

[31] M. A. Klattx and K. Mecke, "Mean-intercept anisotropy analysis of porous media . II . Conceptual shortcomings of the MIL tensor de fi nition and Minkowski tensors as an alternative."

[32] M. Ding, A. Odgaard, and I. Hvid, "Accuracy of cancellous bone volume fraction measured by micro-CT scanning," *Journal of Biomechanics*, vol. 32, no. 3, pp. 323–326, 1999.

[33] J. William and J. Lewis, "Properties and an Anisotropic Model of Cancellous Bone From the Proximal Tibial Epiphysis," *Journal of Biomechanical Engineering*, vol. 104, no. 1, pp. 50–56, 1982.

[34] M. Lengsfeld, M. Lengsfeld, J. Schmitt, J. Schmitt, P. Alter, P. Alter, J. Kaminsky, J. Kaminsky, R. Leppek, and R. Leppek, "Comparison of geometry-based and CT voxel-based nite element modelling and experimental validation," *Medical Engineering & Physics*, vol. 20, pp. 515–522, 1998.

[35] D. Ulrich, B. van Rietbergen, H. Weinans, P. Rüegsegger, B. V. Rietbergen, H. Weinans, and P. Ru, "Finite element analysis of trabecular bone structure: a comparison of image-based meshing techniques." *Journal of biomechanics*, vol. 31, no. 12, pp. 1187–92, 1998. [Online]. Available: http://www.ncbi.nlm.nih.gov/pubmed/9882053

[36] G. Bevill, S. K. Eswaran, F. Farahmand, and T. M. Keaveny, "The influence of boundary conditions and loading mode on high-resolution finite element-computed trabecular tissue properties," *Bone*, vol. 44, no. 4, pp. 573–578, 2009. [Online]. Available: http://dx.doi.org/10.1016/j.bone.2008.11.015

[37] J. H. Keyak, "Improved prediction of proximal femoral fracture load using nonlinear finite element models." *Medical Engineering & Physics*, vol. 23, no. 3, pp. 165–73, 2001. [Online]. Available: http://www.ncbi.nlm.nih.gov/pubmed/11410381

[38] J. H. Keyak and Y. Falkinstein, "Comparison of in situ and in vitro CT scan-based finite element model predictions of proximal femoral fracture load," *Medical Engineering and Physics*, vol. 25, no. 9, pp. 781–787, 2003.

[39] G. H. van Lenthe, M. Stauber, and R. Müller, "Specimen-specific beam models for fast and accurate prediction of human trabecular bone mechanical properties," *Bone*, vol. 39, no. 6, pp. 1182–1189, 2006.

[40] X. S. Liu, P. Sajda, P. K. Saha, F. W. Wehrli, G. Bevill, T. M. Keaveny, and X. E. Guo, "Complete volumetric decomposition of individual trabecular plates and rods and its morphological correlations with anisotropic elastic moduli in human trabecular bone," *Journal of Bone and Mineral Research*, vol. 23, no. 2, pp. 223–235, 2008.

[41] J. Vanderoost, S. V. Jaecques, G. Van der Perre, S. Boonen, J. D'hooge, W. Lauriks, and G. H. van Lenthe, "Fast and accurate specimen-specific simulation of trabecular bone elastic modulus using novel beam-shell finite element models," *Journal of Biomechanics*, vol. 44, no. 8, pp. 1566–1572, 2011. [Online]. Available: http://dx.doi.org/10.1016/j.jbiomech.2011.02.082

[42] H. Wang, X. S. Liu, B. Zhou, J. Wang, B. Ji, Y. Huang, K. C. Hwang, and X. E. Guo, "Accuracy of individual trabecula segmentation based plate and rod finite element models in idealized trabecular bone microstructure," *J Biomech Eng*, vol. 135, no. 4, p. 44502, 2013. [Online]. Available: http://www.ncbi.nlm.nih.gov/pubmed/24231904

[43] J.-Y. Rho, "Mechanical properties and the hierarchical structure of bonef," *Medical Engineering & Physics*, vol. 20, pp. 92–102, 1998. [Online]. Available: http://ac.els-cdn.com/S1350453398000071/1-s2.0-S1350453398000071-main.pdf?{_}tid=c21fe320-1391-11e7-9d45-00000aab0f27{&}acdnat=1490690420{_}e7719fcd5dfb32e142654b267a6edd89{%}0Ahttp://ac.els-cdn.com/S1350453398000071/1-s2.0-S1350453398000071-main.pdf?{_}tid=0a9e19f

[44] K. Choi, "the Elastic Moduli of Human Subchondral Trabecular and Cortical Bone Tissue," *J. Biomechanics*, vol. 23, no. 11, pp. 1103–1113, 1990.

[45] J. C Runkle and J. Pugh, "The micro mechanics of cancellous bone. ii. determination of the elastic modulus of individual trabeculae by a buckling analysis," vol. 36, pp. 2–10, 05 1975.

[46] "Buckling studies of single human trabeculae," *Journal of Biomechanics*, vol. 8, no. 3, pp. 199 – 201, 1975.

[47] S. D. Ryan and J. L. Williams, "Tensile testing of rodlike trabeculae excised from bovine femoral bone," *Journal of Biomechanics*, vol. 22, no. 4, pp. 351 – 355, 1989. [Online]. Available: http://www.sciencedirect.com/science/article/pii/0021929089900493

[48] R. Hodgskinson, J. D. Currey, and G. P. Evans, "Hardness, an indicator of the mechanical competence of cancellous bone," *Journal of Orthopaedic Research*, vol. 7, no. 5, pp. 754–758, 1989.

[49] J. L. Kuhn, S. Goldstein, C. KW, M. London, L. Feldkamp, and L. Matthews, "Comparison of the trabecular and cortical moduli from human illiac crests," vol. 7, pp. 876–84, 11 1989.

[50] P. L. Mente and J. L. Lewis, "Experimental method for the measurement of the elastic modulus of trabecular bone tissue," *Journal of Orthopaedic Research*, vol. 7, no. 3, pp. 456–461, 1989. [Online]. Available: http://dx.doi.org/10.1002/jor.1100070320

[51] J. Y. Rho, R. B. Ashman, and C. H. Turner, "Young's modulus of trabecular and cortical bone material: Ultrasonic and microtensile measurements," *Journal of Biomechanics*, vol. 26, no. 2, pp. 111–119, 1993.

[52] R. Muller and P. Ruegsegger, "Three-dimensional finite element modelling of non-invasively assessed trabecular bone structures," *Medical Engineering and Physics*, vol. 17, no. 2, pp. 126–133, 1995.

[53] G. L. Niebur, M. J. Feldstein, J. C. Yuen, T. J. Chen, and T. M. Keaveny, "High-resolution finite element models with tissue strength asymmetry accurately predict failure of trabecular bone," *Journal of Biomechanics*, vol. 33, no. 12, pp. 1575–1583, 2000.

[54] G. Bevill and T. M. Keaveny, "Trabecular bone strength predictions using finite element analysis of micro-scale images at limited spatial resolution," *Bone*, vol. 44, no. 4, pp. 579–584, 2009. [Online]. Available: http://dx.doi.org/10.1016/j.bone.2008.11.020

[55] T. Guillén, Q. H. Zhang, G. Tozzi, A. Ohrndorf, H. J. Christ, and J. Tong, "Compressive behaviour of bovine cancellous bone and bone analogous materials, microCT characterisation and FE analysis," *Journal of the Mechanical Behavior of Biomedical Materials*, vol. 4, no. 7, pp. 1452–1461, 2011. [Online]. Available: http://dx.doi.org/10.1016/j.jmbbm.2011.05.015

[56] A. J. Wang and D. L. McDowell, "Effects of defects on in-plane properties of periodic metal honeycombs," *International Journal of Mechanical Sciences*, vol. 45, no. 11, pp. 1799–1813, 2003.

[57] M. Ashby, "The properties of foams and lattices," *Philosophical Transactions of the Royal Society A: Mathematical, Physical and Engineering Sciences*, vol. 364, no. 1838, pp. 15–30, 2006. [Online]. Available: http://rsta.royalsocietypublishing.org/cgi/doi/10.1098/rsta.2005.1678

[58] I. G. Masters and K. E. Evans, "Models for the Elastic Deformation of Honeycombs.pdf," vol. 35, no. 1996, pp. 403–422, 1997.

[59] V. S. Deshpande, N. A. Fleck, and M. F. Ashby, "Effective properties of the octet-truss lattice material," *Journal of the Mechanics and Physics of Solids*, vol. 49, no. 8, pp. 1747–1769, 2001.

[60] H. Zhu, J. Knott, and N. Mills, "Analysis of the elastic properties of open-cell foams with tetrakaidecahedral cells," *Journal of the Mechanics and Physics of Solids*, vol. 45, no. 3, pp. 319–343, 1997. [Online]. Available: http://linkinghub.elsevier.com/retrieve/pii/S0022509696000907

[61] L. J. Gibson, "by Lorna Jane Gibson A dissertation submitted to the University of Cambridge for the Degree of Dbctor of Philosophy Churchill College Augus t 1981," 1981.

[62] R. B. Ashman and J. Y. Rho, "Elastic modulus of trabecular bone material," *Journal of Biomechanics*, vol. 21, no. 3, pp. 177 – 181, 1988. [Online]. Available: http://www.sciencedirect.com/science/article/pii/0021929088901674

[63] E. Ptochos and G. Labeas, "Elastic modulus and Poisson's ratio determination of micro-lattice cellular structures by analytical, numerical and homogenisation methods," *Journal of Sandwich Structures and Materials*, vol. 14, no. 5, pp. 597–626, 2012. [Online]. Available: http://jsm.sagepub.com/cgi/doi/10.1177/1099636212444285

[64] R. E. Newnham, *Properties of Materials: Anisotropy, Symmetry, Structure.* New York: Oxford University Press, 2005.

[65] M. Lai, E. Krempl, and D. Ruben, *Introduction to Continuum Mechanics.* Burlington: Elsevier, 2009.

[66] E. J. Hastings, J. Mesit, and R. K. Guha, "Optimization of Large-Scale , Real-Time Simulations by Spatial Hashing," *Summer Computer Simulation Conference*, pp. 9–17, 2005.

[67] Y.-D. Liang and B. A. Barsky, "A new concept and method for line clipping," *ACM Trans. Graph.*, vol. 3, no. 1, pp. 1–22, Jan. 1984. [Online]. Available: http://doi.acm.org/10.1145/357332.357333

[68] H. Zhu, J. Knott, and N. Mills, "Analysis of the elastic properties of open-cell foams with tetrakaidecahedral cells," *Journal of the Mechanics and Physics of Solids*, vol. 45, no. 3, pp. 319–343, 1997. [Online]. Available: http://linkinghub.elsevier.com/retrieve/pii/S0022509696000907

[69] A. S. Murphy, "Line Thickening by Modification To Bresenham's Algorithm," *IBM Technical Disclosure Bulletin*, vol. 20, no. 12, pp. 5358–5366, 1978.